A Review of the Hubble Tension

Rebecca Houliston

Thesis presented for the degree of Master of Science in the Department of Mathematics and Applied Mathematics University of Cape Town February 2022

supervised by

Dr. Julien Larena

Prof. Amanda Weltman

The financial assistance of the National Research Foundation (NRF) towards this research is hereby acknowledged. Opinions expressed and conclusions arrived at are those of the author and are not necessarily to be attributed to the NRF.

Financial assistance from the University of Cape Town is also acknowledged.

Plagiarism declaration

I know the meaning of plagiarism and declare that all of the work in the thesis, save for that which is properly acknowledged, is my own.

Signed by candidate 6 February 2022

Rebecca Houliston

Abstract

The Hubble constant H_0 is the rate of expansion of the universe today. The discrepancy between the early universe H_0 value, inferred using ΛCDM from *Planck* observations of the CMB, and the late universe H_0 value, obtained using luminosity and distance measurements from a Type Ia Supernova (SNIa) distance ladder, has now reached 4.2σ. Despite improvements in precision, this tension has increased. This thesis studies these two measurements, as well as various other H0 determinations, which are independent of both the CMB and the SNIa distance ladder and corroborate the Hubble tension (with the caveat that many have large uncertainties), with a particular focus on lensing and gravitational waves. Some of the very many solutions proposed to resolve the Hubble tension are also explored, with an emphasis on late universe solutions and Early Dark Energy. The improvement in precision, the growing discrepancy, and the supporting independent measurements of the *Planck* and SNIa distance ladder H_0 values are strong evidence that a significant tension between the early and late universe exists. This indicates that some modification to or expansion of ΛCDM is required. A great deal of models and solutions have been proposed to do so, however none have managed to fully resolve the tension yet.

Contents

List of Figures

Chapter 1

Introduction

The aim of cosmology is to describe the universe around us: what is there and how it came to be. Theories are proposed to explain astronomical observations. If observations and theories do not align, the theories need to rethought and adjusted, and the uncertainties and precision of the observations examined and improved. This thesis will focus on a recent instance of theories and observations not agreeing: the 'Hubble tension'. First, however, the accepted model of the universe will be introduced.

The universe when observed on large scales by fundamental observers is homogeneous and isotropic, that is, it looks the same when observed from any position. It is smooth on large scales but full of structures, such as galaxies, on small scales. The geometry of the universe is well-approximated by the Friedmann-Lemaître-Robertson-Walker (FLRW) metric:

$$ds^2 = -dt^2 + a^2(t)\left[\frac{dr^2}{1-K\,r^2} + r^2\left(d\theta^2 + \sin^2\theta\,d\phi^2\right)\right] \tag{1.1}$$

where t is the proper time measured by fundamental observers along their worldline $dr = d\theta = d\phi = 0$, $a(t)$ is the scale factor which describes the change in the distance between two points with time, r is the coordinate radial distance, $K \in \mathbb{R}$ gives the curvature of space, and the solid angle is $d\Omega^2 = d\theta^2 + \sin^2\theta\,d\phi^2$. In the FLRW metric, the Einstein Field Equations (EFE) reduce to the Friedmann equation and the covariant energy conservation equation:

$$H(t)^2 = \frac{8\,\pi\,G}{3}\,\rho(t) - \frac{K}{a(t)^2} \quad \text{and} \tag{1.2}$$

$$0 = \dot{\rho}(t) + 3H(t)\left(\rho(t) + p(t)\right) \quad , \tag{1.3}$$

where $\rho(t)$ is the matter density, $p(t)$ is the pressure, and the dot denotes the derivative with respect to proper time t.

The physical distance between two spatially separated (i.e. $dt = 0$) fundamental observers, located at r and $r + \Delta r$, with $\Delta r \ll 1$, and $\phi = \phi_0$, $\theta = \theta_0$ (where the subscript 0 denotes the current value, so $d\phi^2 = d\theta^2 = 0$), is given by

$$\Delta d_{\text{phys}}(r,t) = a(t)\frac{\Delta r}{\sqrt{1-K\,r^2}} \quad . \tag{1.4}$$

The conformal time η is defined by

$$d\eta = \frac{dt}{a(t)} \quad , \tag{1.5}$$

$$\eta - \eta_0 = \int_{t_0}^{t} \frac{dt'}{a(t')} \quad \text{and} \tag{1.6}$$

$$dt^2 = a(\eta)^2 d\eta^2 \qquad \text{with} \qquad a(\eta) \equiv a(t(\eta)) \quad . \tag{1.7}$$

The scale factor $a(t)$ can be factored out of the FLRW metric (1.1) when using conformal time:

$$ds^2 = a^2(\eta) \left[-d\eta^2 + \frac{dr^2}{1 - K\, r^2} + r^2 \left(d\theta^2 + \sin^2\theta \, d\phi^2 \right) \right] \quad . \tag{1.8}$$

The radial coordinate χ is defined by

$$d\chi \equiv \frac{dr}{\sqrt{1 - K\, r^2}} \quad , \tag{1.9}$$

and, setting $\chi(r = 0) = 0$, is

$$\chi = \int_0^r \frac{dr'}{\sqrt{1 - K\, r^2}} \quad . \tag{1.10}$$

Integrating (1.10) and defining $S_K(\chi) \equiv r(\chi)$ results in

$$S_K(\chi) = \begin{cases} \frac{1}{\sqrt{K}} \sin(\sqrt{K}\, \chi) & K > 0 \\ \chi & K = 0 \\ \frac{1}{\sqrt{-K}} \sinh(\sqrt{-K}\, \chi) & K < 0 \end{cases} \quad . \tag{1.11}$$

Note that for $K > 0$, $r \in \left[0, \frac{1}{\sqrt{K}}\right]$ and $\chi \in [0, \pi]$; and for $K \leq 0$, $r \in [0, \infty)$ and $\chi \in [0, \infty)$. The FLRW metric (1.8) can then be written in terms of χ as

$$ds^2 = a^2(\eta) \left[-d\eta^2 + d\chi^2 + S_K^2(\chi) \left(d\theta^2 + \sin^2\theta \, d\phi^2 \right) \right] \quad . \tag{1.12}$$

For $K = 0$, the metric represents standard Euclidean flat space, for $K > 0$ a round metric on a 3-sphere S^3 with radius $\frac{1}{\sqrt{K}}$, and for $K < 0$ a standard metric on a hyperbolic space H^3. The radius of a 2-sphere at a coordinate distance χ from the origin is given by $S_K(\chi)$: the physical area of a 2-sphere located at $d\eta = d\chi = 0$ is then

$$S_K^2(\chi) \left(d\theta^2 + \sin^2\theta \, d\phi^2 \right) = 4\pi \, S_K^2(\chi) \quad . \tag{1.13}$$

The metric (1.12) yields for radial light rays, where $ds^2 = d\theta = d\phi = 0$,

$$\chi - \chi_0 = \pm(\eta - \eta_0) \quad . \tag{1.14}$$

The 4-velocities of fundamental observers are given by

$$\mathbf{u} = \frac{\partial}{\partial t} \quad \text{with components} \quad u^\mu = (1, 0, 0, 0)_{(t,r,\theta,\phi)} = \delta^\mu_0 \quad . \tag{1.15}$$

In the χ and η coordinate system, the components are given by

$$u^\mu = \left(\frac{1}{a}, 0, 0, 0 \right)_{(\eta,\chi,\theta,\phi)} = \frac{1}{a}\, \delta^\mu_0 \quad . \tag{1.16}$$

The physical separation of two fundamental observers at time t and located spatially at position vectors $\vec{x}_1$ and $\vec{x}_2$ that are constant with respect to time is given by

$$\vec{r}_{12} = a(t)\,(\vec{x}_1 - \vec{x}_2) \quad . \tag{1.17}$$

The time derivative of this physical separation is

$$\begin{aligned} \frac{d}{dt}\,\vec{r}_{12} &= \frac{d}{dt}\,[a(t)\,(\vec{x}_1 - \vec{x}_2)] && (1.18)\\ &= \dot{a}\,(\vec{x}_1 - \vec{x}_2) && (1.19)\\ &= \frac{\dot{a}}{a}\,\vec{r}_{12} \quad . && (1.20) \end{aligned}$$

Equation (1.20) is called the Hubble-Lemaître law. The Hubble rate, which describes the expansion of the universe, is defined as

$$H(t) \equiv \frac{\dot{a}}{a} \quad . \tag{1.21}$$

At the current time, the Hubble-Lemaître law is

$$\vec{v} = H_0\,\vec{r} \quad . \tag{1.22}$$

Cosmological objects move with respect to each other with a velocity that increases the further they are apart. In an expanding universe, $H_0 > 0$ and the velocity is a recession velocity. A galaxy recedes faster the more distant it is. The discovery that the universe is expanding is usually attributed to Edwin Hubble in 1929 [72], but it was also as a result of joint efforts from, for example, Slipher [130] and Lemaître [84]. The Hubble constant $H_0 = 100\,h\,\mathrm{km\,s^{-1}\,Mpc^{-1}}$ gives the rate of expansion today, and H_0^{-1} is a time-scale for this. Essentially, it is the time at which all galaxies were together [50], and so it provides an estimate for the age of the universe. Hubble in 1929 found $H_0 = 500\,\mathrm{km\,s^{-1}\,Mpc^{-1}}$ with huge errors. In 1958 Sandage [123] found $H_0 = 75\,\mathrm{km\,s^{-1}\,Mpc^{-1}}$. For $H_0 = [\text{value}]\,\mathrm{km\,s^{-1}\,Mpc^{-1}}$, the units indicate that for each Mpc away a source is, the source recedes with velocity $[\text{value}]\,\mathrm{km\,s^{-1}}$ faster. A parsec (pc) is the 'distance at which the radius of Earth's orbit subtends an angle of one second of arc' [13], and 1pc = 3.26 light years. The Hubble radius is where the recession velocity reaches the speed of light and no objects further away than that can be observed by us [109]. H_0 normalizes all other values. The uncertainties in H_0 propagate into other cosmological parameters, and h is used to follow them.

In the geometric optics limit, where the wavelength of light considered is small with respect to the typical curvature radius of spacetime, the propagation of electromagnetic waves is well-approximated by the properties of light rays. Light rays are null curves with a tangent vector field $\mathbf{k}$ with components $k^\mu = \dfrac{dx^\mu}{d\lambda}$, where λ is an affine parameter along the light rays considered. k^μ is also called the separation vector because it describes the relative behaviour of two neighbouring light rays. The tangent vector field $\mathbf{k}$ satisfies

$$\begin{aligned} g(\mathbf{k},\mathbf{k}) &= k_\mu k^\mu = 0 \quad \text{and} && (1.23)\\ \nabla_{\mathbf{k}}\mathbf{k} &= k^\nu \nabla_\nu k^\mu = 0. && (1.24) \end{aligned}$$

Equation (1.24) is called the geodesic equation.

The projection tensor h projects orthogonally on hypersurfaces of constant proper time t or, equivalently conformal time η, and is given by

$$h = g + \mathbf{u} \otimes \mathbf{u} \quad , \tag{1.25}$$

$$h_{\mu\nu} = g_{\mu\nu} + u_\mu u_\nu = g_{\mu\nu} + \delta_{\mu 0}\delta_{\nu 0} \quad . \tag{1.26}$$

Note that $h_{0\mu} = -1 + 1 = 0$. The metric tensor in conformal spacetime is given by

$$g_{\mu\nu} = a^2 \begin{pmatrix} -1 & 0 & 0 & 0 \\ 0 & 1 & 0 & 0 \\ 0 & 0 & \chi^2 & 0 \\ 0 & 0 & 0 & \chi^2 \sin^2\theta \end{pmatrix} \quad . \tag{1.27}$$

The spatial components of h are thus

$$h_{ij} = a^2 \begin{pmatrix} 1 & 0 & 0 \\ 0 & \chi^2 & 0 \\ 0 & 0 & \chi^2 \sin^2\theta \end{pmatrix} \quad . \tag{1.28}$$

That is,

$$h_{ij} = a^2 \gamma_{ij} \quad , \tag{1.29}$$

where γ_{ij} is the metric of conformal space.

For a future directed light ray measured in the rest frame of a fundamental observer, the energy E and momentum p^μ of a photon are defined by

$$E = -k^\mu u_\mu \quad \text{and} \quad p^\mu = h^\mu{}_\nu \, k^\nu \quad , \tag{1.30}$$

where $\dfrac{p^\mu}{E}$ are the components of the instantaneous direction of the propagation of light rays in the rest frame of the fundamental observers. Furthermore, p^μ is orthogonal to the velocity of the observers:

$$p^\mu u_\mu = 0 \quad \Longrightarrow \quad p^0 = 0 \quad . \tag{1.31}$$

Therefore the components of the 3-momentum of photons are given by p^μ, and their 4-momentum can be written as

$$k^\mu = E\, u^\mu + p^\mu \quad . \tag{1.32}$$

Using equations (1.32) and (1.30), equation (1.23) can be written

$$0 = k_\mu k^\mu = k_\mu E + k_\mu p^\mu \tag{1.33}$$

$$= k_\mu(-k^\mu u_\mu)u^\mu + k_\mu h^\mu{}_\nu k^\nu \tag{1.34}$$

$$= -E^2 + h_{ij} p^i p^j \quad . \tag{1.35}$$

Then, using (1.29),

$$-E^2 + a^2 \gamma_{ij}\, p^i\, p^j = 0 \quad . \tag{1.36}$$

Projecting the geodesic equation (1.24) along $\mathbf{u}$:

$$E\,\dot{E} = +a^2\, H\, \gamma_{ij}\, p^i\, p^j \quad , \tag{1.37}$$

$$E^2 = -a^2\, \frac{E}{\dot{E}}\, H\, \gamma_{ij}\, p^i\, p^j \quad . \tag{1.38}$$

Then, using (1.36), this results in the following:

$$a^2\,\gamma_{ij}\,p^i\,p^j = -a^2\,\frac{E}{\dot{E}}\,H\,\gamma_{ij}\,p^i\,p^j \tag{1.39}$$

$$1 = -\frac{E}{\dot{E}}\,H \tag{1.40}$$

$$\frac{\dot{E}}{E} = -\frac{\dot{a}}{a} \tag{1.41}$$

$$E = \frac{C}{a} \quad , \quad C \in \mathbb{R} \quad . \tag{1.42}$$

For a light ray with frequency ν, the energy of a photon is $E = \hbar\,\nu$, where $\hbar$ is the reduced Planck mass. Then, following from (1.42), the frequency of light is affected by the expansion along the trajectory of photons according to

$$\nu(t) = \frac{a(t_e)}{a(t)}\,\nu(t_e) \quad , \tag{1.43}$$

where t is the time of observation and t_e is the time at which photons are emitted. A fundamental observer located at the centre of the coordinate system, at $\chi = 0$, receives a light ray at $t = t_0$ (today) with wave length $\lambda(t_0)$. The redshift z is defined by

$$z \equiv \frac{\lambda(t_0) - \lambda(t_e)}{\lambda(t_e)} \quad . \tag{1.44}$$

Noting that wavelength and frequency are inversely related through $\lambda = \dfrac{1}{\nu}$, and using (1.43), the wavelength today is given by

$$\lambda(t_0) = \frac{a(t_0)}{a(t_e)}\,\lambda(t_e) \quad . \tag{1.45}$$

In FLRW, the ratio of the scale factor at observation and emission is therefore, substituting (1.44) in to (1.43),

$$1 + z = \frac{a(t_0)}{a(t_e)} \quad . \tag{1.46}$$

The effect of redshift is time dilation: all observed phenomena of a source will appear to be slowed down by the same ratio $(1 + z)$. Radiation is redshifted as it propagates from a distance source to an observer. In an expanding universe, $a(t_0) > a(t_e)$ which, by (1.45), shows that $\lambda(t_0) > \lambda(t_e)$. The observed wavelength is larger, and therefore redder, than the emitted wavelength. Thus z is called redshift. The scale factor a and the radial coordinate distance χ are only defined simultaneously up to an overall scaling. Then, setting units for χ appropriately at $t = t_0$, the scale factor today can then be set at $a(t_0) = 1$. Then,

$$1 + z = \frac{1}{a} \quad . \tag{1.47}$$

The coordinate distances, given by radial coordinates r and χ, are not observable in general relativity (GR) because they are calculated only by the spacelike separation of two events in spacetime. Physically meaningful distances in GR should include timelike separations, and so in cosmology are obtained by determining distances measured along the past light cone of an observer. A light ray observed by a fundamental observer at $\chi = 0$, $\eta = \eta_0$, emitted at time t corresponding to redshift z and propagating radially with $d\theta = d\phi = 0$, will have $ds^2 = 0$ along it. Then, the FLRW metric (1.12) will reduce to

$$d\chi = -\frac{dt}{a(t)} = -\frac{da}{a^2\,H} \quad . \tag{1.48}$$

The minus sign ensures that the ray propagates forward in time from the source at $\chi > 0$ to the observer at $\chi = 0$. Differentiating (1.47) results in

$$dz = -\frac{da}{a^2} \quad , \tag{1.49}$$

and so equation (1.48) can be written

$$d\chi = \frac{dz}{H(z)} \quad . \tag{1.50}$$

The comoving radial distance is then defined as

$$\chi(z) \equiv \int_0^z \frac{dz'}{H(z')} \quad . \tag{1.51}$$

Note that $\chi(z)$ is not an observable.

Consider a comoving 2-sphere with $d\eta = d\chi = 0$, located at $\chi = \chi(z)$. Because it is comoving, the scale factor $a(\eta)$ can be ignored, and so the metric (1.12) gives the line element

$$ds^2_{\rm com} = S^2_K(\chi)\, \left(d\theta^2 + \sin^2\theta\, d\phi^2\right) \quad . \tag{1.52}$$

Let there be a small source located on the sphere which is observed at the centre under a small solid angle $d\Omega^2_{\rm obs}$ that subtends a small transverse area portion of the sphere. The line element of this source will be

$$dS^{\rm source}_{\rm com} = S^2_K(\chi)\, d\Omega^2_{\rm obs} \quad . \tag{1.53}$$

The comoving angular distance between the source at redshift z and the observer, $R_{\rm ang}(z)$, is defined as

$$R^2_{\rm ang}(z) \equiv \frac{dS^{\rm source}_{\rm com}}{d\Omega^2_{\rm obs}} \quad . \tag{1.54}$$

Using equations (1.52) and (1.53), this reduces to

$$R_{\rm ang}(z) = S_K(\chi(z)) \quad . \tag{1.55}$$

This indicates that objects of the same size located at the same comoving distance $\chi(z)$ will have different angular distances $R_{\rm ang}(z)$ in spaces of different curvature. $R_{\rm ang}(z)$ is not directly observable because it depends on the comoving size of the source which is not observable. The actual physical size of the source is related to the comoving size through

$$dS^{\rm source}_{\rm phys} = a^2\, dS^{\rm source}_{\rm com} \quad . \tag{1.56}$$

The angular diameter distance of an object located at z with respect to the observer, $D_A(z)$, is observable and is defined as

$$D^2_A(z) \equiv \frac{dS^{\rm source}_{\rm phys}}{d\Omega^2_{\rm obs}} \quad . \tag{1.57}$$

Using equations (1.54) - (1.56), and the definition of the redshift (1.47), this reduces to

$$D_A(z) = a\, R_{\rm ang}(z) \tag{1.58}$$

$$D_A(z) = \frac{1}{1+z}\, S_K(\chi(z)) \quad . \tag{1.59}$$

The angular diameter distance $D_A(z)$ is, in principle, measurable: if an observer can measure the apparent angular size of a source on the sky while also having knowledge of the absolute physical size of the source from theoretical modelling, then $D_A(z)$ can be deduced. Objects whose physical size is both known and stable are called standard rulers. For example, CMB fluctuations have a length scale that is determined by early universe scales [128] and so are standard rulers. Similarly, standard candles are objects whose absolute luminosity is both known, from theoretical modelling, and nearly constant over their position in the sky. Assume an observer at $\chi = 0$ and $t = t_0$ observes a source located at a comoving radial distance $\chi(z)$, which is a standard candle and radiates isotropically with absolute luminosity $L_{\rm source}$ photons with frequency ν_e at time $t = t_e$. In a small time interval δt_e, the number of photons emitted by the object in a spherically symmetric manner is given by

$$N = L\,\frac{\delta t_e}{h\,\nu_e} \quad , \tag{1.60}$$

where h is Planck's constant. Integrating over the sphere with radius D_m (the metric distance $D_m = a_0\,r$, where r is the proper distance) occupied by these photons at observation by the solid angle line element of the FLRW metric $a_0^2\,r^2\,d\Omega^2$, the area of a sphere is then:

$$A = 4\pi\,D_m^2 \quad . \tag{1.61}$$

The frequency of the photons has been reduced by $1 + z$ to ν_0, and they arrive in time interval δt_0 which has been stretched out by $(1 + z)$. By equation (1.43),

$$h\,\nu_0 = \frac{h\,\nu_e}{1+z} \quad \text{and} \quad \delta t_0 = \delta t_e\,(1+z) \quad . \tag{1.62}$$

The observed flux is the energy received over a time interval in the detection area, and the luminosity is the energy emitted per unit time. The total energy that is detected by the observer is $N\,h\,\nu$. Then, the flux is given by:

$$\Phi = \frac{N\,h\,\nu_0}{A\,\delta t_0} \tag{1.63}$$

$$\Phi = \frac{N\,h\,\nu_e}{(1+z)\,A\,\delta t_e\,(1+z)} \tag{1.64}$$

$$\Phi = \frac{L_{\rm source}}{A\,(1+z)^2} \quad . \tag{1.65}$$

Substituting the area of the sphere given in (1.61), the observed flux of a source with luminosity $L_{\rm source}$ at redshift z and coordinate distance D is then

$$\Phi = \frac{L_{\rm source}}{4\pi\,D_m^2\,(1+z)^2} \quad . \tag{1.66}$$

Defining the luminosity distance

$$D_L(z) \equiv D_m\,(1+z) \quad , \tag{1.67}$$

the observed flux is then given by

$$\Phi_{\rm obs} = \frac{L_{\rm source}}{4\pi\,D_L(z)^2} \quad . \tag{1.68}$$

$D_L(z)$ is the luminosity distance between a source and an observer: it is an observable that can be directly measured. Luminosity is the rate of emission of radiant energy, the rate of change of energy, and so can be written

$$L_{\rm source} = \frac{\Delta E_{\rm emit}}{\Delta t_{\rm emit}} = \frac{\Delta E(z)}{\Delta t(z)} \quad , \tag{1.69}$$

where $\Delta E_{\rm emit}$ is the change in energy over an emission time period $\Delta t_{\rm emit}$. The redshift (1.46) experienced by light between emission and observation results in a change in the observed energy of

$$\Delta E_{\rm obs} = \frac{\Delta E_{\rm emit}}{1+z} \quad . \tag{1.70}$$

Two light rays emitted from a source at an interval of $\Delta\eta_{\rm emit}$ are observed in an interval of $\Delta\eta_0$. Light rays are straight lines in conformal spacetime so $\Delta\eta_0 = \Delta\eta_{\rm emit}$. In proper time, however,

$$\Delta t_0 = (1+z)\,\Delta t_{\rm emit} \quad . \tag{1.71}$$

This, and equations (1.70) and (1.69), results in the observed luminosity:

$$L_{\rm obs} = \frac{\Delta E_{\rm obs}}{\Delta t_0} = \frac{\Delta E_{\rm emit}}{1+z}\frac{1}{(1+z)\,\Delta t_{\rm emit}} \tag{1.72}$$

$$L_{\rm obs} = \frac{L_{\rm source}}{(1+z)^2} \quad . \tag{1.73}$$

The observed flux, $\Phi_{\rm obs}$, is the ratio of the total observed luminosity $L_{\rm obs}$ to the surface area over which this luminosity is distributed. The latter is the physical area today of a sphere centred on $R_{\rm ang}(z) = S_K(\chi(z))$, which, using (1.53) and (1.56), is given by

$$S^{\rm phys} = a_0^2\, S^{\rm com} = 4\pi S_K^2(\chi(z)) \quad . \tag{1.74}$$

The observed flux is then, using (1.74) and (1.73), given by

$$\Phi_{\rm obs} = \frac{L_{\rm obs}}{4\pi\, S_K^2(\chi(z))} = \frac{L_{\rm source}}{4\pi\, S_K^2(\chi(z))\,(1+z)^2} \quad . \tag{1.75}$$

Comparing (1.75) with (1.68), the following expression is obtained for the luminosity distance:

$$D_L(z) = (1+z)\, S_K(\chi(z)) \quad . \tag{1.76}$$

Substituting in to this the expression (1.59) for the angular diameter distance $D_A(z)$ gives Etherington's reciprocity relation (also called the distance-duality relation):

$$D_L(z) = (1+z)^2\, D_A(z) \quad , \tag{1.77}$$

which is true in any spacetime and metric gravity theory, as long as the number of photons is conserved during the propagation of light between the source and observer. In flat FLRW, the angular diameter and luminosity distances are given by

$$D_A(z) = \frac{1}{1+z}\int_0^z \frac{dz'}{H(z')} \quad \text{and} \tag{1.78}$$

$$D_L(z) = (1+z)\int_0^z \frac{dz'}{H(z')} \quad . \tag{1.79}$$

The angular diameter distance $D_A(z)$ is defined along a future-directed light ray bundle diverging from the source: it measures the distance between the observer and the source at the time when light was emitted. By comparison, the luminosity distance measures the distance between the observer and the source at the time when the light is observed.

To determine the nature of the angular diameter and luminosity distances, the dynamics of the FLRW universe, through $H(z)$, are required. The Einstein Field Equations are

$$R_{\mu\nu} + \frac{1}{2} R\, g_{\mu\nu} + \Lambda\, g_{\mu\nu} = 8\pi\, G\, T_{\mu\nu} \quad . \tag{1.80}$$

The components of the Ricci tensor $R_{\mu\nu}$ are

$$R_{00} = -3\,\frac{\ddot{a}}{a} \quad \text{and} \tag{1.81}$$

$$R_{ij} = a^2 \left(2H^2 + \frac{\ddot{a}}{a} + 2\,\frac{K}{a^2} \right) \gamma_{ij} \quad ; \tag{1.82}$$

and its trace the Ricci scalar is

$$R = 6 \left(H^2 + \frac{\ddot{a}}{a} + \frac{K}{a^2} \right) \quad . \tag{1.83}$$

The energy-momentum tensor $T_{\mu\nu}$ is given by

$$T^{(i)}_{\mu\nu} = (\rho_i + p_i)\, u_\mu\, u_\nu + p_i\, g_{\mu\nu} \quad , \tag{1.84}$$

where dark matter and dark energy are treated as independent, non-interacting perfect fluids with energy densities $\rho_i(t)$ and pressures $p_i(t)$. The conservation of energy-momentum equation is

$$\nabla_\mu T^{(i)\mu}_\nu = 0 \quad . \tag{1.85}$$

Each fluid has an equation of state

$$w_i = \frac{p_i}{\rho_i} \quad . \tag{1.86}$$

Then the conservation of energy-momentum equation (1.85) can be written

$$\dot{\rho}_i + 3(1 + w_i) H \rho_i = 0 \quad . \tag{1.87}$$

The total energy density ρ and pressure p are the sums of the pressures and energy densities of the individual fluids:

$$\rho = \sum_i \rho_i \quad \text{and} \quad p = \sum_i p_i \quad . \tag{1.88}$$

Then, $w = \dfrac{p}{\rho}$, and the equation for the total conservation of energy-momentum (1.87) is then

$$\dot{\rho} + 3(1 + w) H \rho = 0 \quad . \tag{1.89}$$

In non-relativistic fluids, the particles move slowly with respect to the speed of light. This leads to a pressure $p_i \sim 0$ and therefore equation of state $w_i \sim 0$. Standard baryonic matter (for most of the history of the universe) and neutrinos in the very late-time universe are two examples of non-relativistic fluids. Non-relativistic matter is usually called dust. On the other hand, particles in relativistic fluids move with velocities close to the speed of light. The pressure in relativistic fluids is $p_i \simeq \dfrac{1}{3}\rho_i$, which gives an equation of state $w_i = \dfrac{1}{3}$. A more exotic fluid can be considered when rewriting the Einstein Field Equations (1.80) by moving $\Lambda\, g_{\mu\nu}$ to the right hand side. Then, the cosmological constant Λ can be interpreted as a perfect fluid with $p_\Lambda = -\rho_\Lambda$ and the equation of state $w_\Lambda = -1$. Barotropic fluids are perfect fluids with a constant equation of state. Dust, relativistic fluids and the cosmological

constant are thus all barotropic fluids. Solving equation (1.89) for dust ('NR' subscript) and relativistic fluids ('R' subscript) with their respective equations of states results in

$$\rho_{\rm NR} = \rho_{\rm NR,0}\, a^{-3} \quad \text{and} \tag{1.90}$$

$$\rho_{\rm R} = \rho_{\rm R,0}\, a^{-4} \quad , \tag{1.91}$$

where the 0 subscript denotes the present day value. The solution for non-relativistic fluids (1.90) indicates that in an expanding universe, dust is diluted by a factor a^3. This means that the number of particles remains constant while the volume increases. The solution for relativistic fluids (1.91) shows that relativistic matter receives extra dilution compared to dust through a^{-1}, which comes from the redshift of the energy of individual photons in the fluid. From now on, the subscripts m (for matter) and r (for radiation) will refer to non-relativistic and relativistic matter respectively. The conservation of energy and momentum equation (1.89) can also be solved for the cosmological constant with $w_\Lambda = -1$, resulting in $\dot{\rho}_\Lambda = 0$, i.e. $\rho_\Lambda = \text{constant} = \dfrac{\Lambda}{8\pi G}$.

The dynamical equations governing the dynamics of the FLRW universe are the Friedmann equation,

$$H^2 = \left(\frac{\dot{a}}{a}\right)^2 = \frac{8\pi G}{3}\rho - \frac{K}{a^2} + \frac{\Lambda}{3} \quad ; \tag{1.92}$$

the Raychaudhuri equation,

$$\frac{\ddot{a}}{a} = -\frac{4\pi G}{3}(\rho + 3p) + \frac{\Lambda}{3} \quad ; \tag{1.93}$$

and the continuity equation,

$$\dot{\rho} = -3(\rho + p)\, H \quad . \tag{1.94}$$

This system of equations (1.92) - (1.94) is not independent: only two independent equations need to be solved for the three unknown functions. To solve the system, a constant equation of state needs to be assumed. Then, the continuity equation (1.94) can be solved:

$$\dot{\rho} = -3(1+w)\,\frac{\dot{a}}{a}\,\rho \tag{1.95}$$

$$\rho(t) = \rho_0\, a(t)^{-3(1+w)} \quad . \tag{1.96}$$

Assuming $K = \Lambda = 0$ and $w \neq 1$, the Friedmann equation (1.92) can then be solved:

$$a(t) = \left(\frac{t}{t_0}\right)^{2/3(1+w)} \quad , \tag{1.97}$$

$$H(t) = \frac{2}{3(1+w)t} \quad . \tag{1.98}$$

More specifically, for dust with $w = 0$,

$$a(t) = \left(\frac{t}{t_0}\right)^{2/3} \quad \Longrightarrow \quad a \propto t^{2/3} \quad ; \tag{1.99}$$

and for a relativistic fluid with $w = \dfrac{1}{3}$,

$$a(t) = \left(\frac{t}{t_0}\right)^{1/2} \quad \Longrightarrow \quad a \propto t^{1/2} \quad . \tag{1.100}$$

The dimensionless density parameters are defined by

$$\Omega_i(z) \equiv \frac{8\pi G\,\rho_i(z)}{3H^2(z)} \quad . \tag{1.101}$$

The total energy content from all matter and radiation is given by

$$\Omega(z) \equiv \frac{8\pi G\rho(z)}{3H^2(z)} = \sum_i \Omega_i(z) \quad , \tag{1.102}$$

and the dimensionless density parameters of the cosmological constant and curvature are given by

$$\Omega_\Lambda(z) = \frac{8\pi G\rho_\Lambda(z)}{3H^2(z)} \quad \text{and} \tag{1.103}$$

$$\Omega_K(z) = \frac{-K}{a^2(z)\,H^2(z)} \quad . \tag{1.104}$$

These density parameters, together with $\rho_\Lambda = \dfrac{\Lambda}{8\pi G}$, can be substituted into the Friedmann equation (1.92), resulting in

$$1 = \Omega + \Omega_K + \Omega_\Lambda \quad . \tag{1.105}$$

Furthermore, again using the subscript 0 to denote the present day value,

$$1 = \sum_i \Omega_{i,0} + \Omega_{K,0} + \Omega_{\Lambda,0} \quad . \tag{1.106}$$

Using equation (1.96), the dimensionless density parameter (1.101) for each barotropic fluid with constant equation of state w_i can be written

$$\Omega_i(z) = \Omega_{i,0} \left(\frac{H_0}{H(z)}\right)^2 (1+z)^{3(1+w_i)} \quad . \tag{1.107}$$

The dimensionless expansion rate $E(z)$ is now introduced as

$$E(z) \equiv \frac{H(z)}{H_0} \quad . \tag{1.108}$$

Equation (1.107) can then be rewritten as

$$\Omega_i(z) = \frac{\Omega_{i,0}}{E^2(z)} (1+z)^{3(1+w_i)} \quad . \tag{1.109}$$

Then, using this and equations (1.103) and (1.104), and recalling that $a_0 = 1$ and ρ_Λ is a constant, (1.105) can be rewritten as follows:

$$1 = \sum_i \Omega_i + \Omega_\Lambda + \Omega_K \tag{1.110}$$

$$1 = \sum_i \Omega_{i,0} \frac{1}{E^2(z)} (1+z)^{3(1+w_i)} + \Omega_\Lambda + \Omega_K \tag{1.111}$$

$$E^2(z) = \sum_i \Omega_{i,0} (1+z)^{3(1+w_i)} + \Omega_\Lambda \frac{H^2}{H_0^2} + \Omega_K \frac{H^2}{H_0^2} \tag{1.112}$$

$$E^2(z) = \sum_i \Omega_{i,0} (1+z)^{3(1+w_i)} + \frac{8\pi G\,\rho_\Lambda}{3H_0^2} - \frac{K(1+z)^2}{H_0^2} \tag{1.113}$$

$$E^2(z) = \sum_i \Omega_{i,0} (1+z)^{3(1+w_i)} + \Omega_{\Lambda,0} + \Omega_{K,0} (1+z)^2 \quad . \tag{1.114}$$

For barotropic fluids with $K = 0$, the critical density of the universe is defined as

$$\rho_{c,0} \equiv \frac{3H_0^2}{8\pi G} \quad . \tag{1.115}$$

Then, from (1.101),

$$\rho_{m,0} = \frac{3H_0^2}{8\pi G}\,\Omega_{m,0} = \rho_{c,0}\,\Omega_{m,0} \quad , \tag{1.116}$$

and, using (1.90),

$$\rho_m = \Omega_{m,0}\,\rho_{c,0}\,a^{-3} = \Omega_{m,0}\,\rho_{c,0}\,(1+z)^3 \quad . \tag{1.117}$$

Similarly,

$$\rho_r = \Omega_{r,0}\,\rho_{c,0}\,a^{-4} = \Omega_{r,0}\,\rho_{c,0}\,(1+z)^4 \quad \text{and} \tag{1.118}$$

$$\rho_\Lambda = \Omega_\Lambda\,\rho_{c,0} \quad . \tag{1.119}$$

An expanding universe undergoes three phases: the radiation dominated era (RDE), the matter dominated era (MDE) and the dark energy dominated era (ΛDE). In the radiation dominated era, the energy content and dynamics of the universe are dominated by a relativistic fluid with energy density $\rho(z) \sim (1+z)^4$ at early times (i.e. at high redshift). In the matter dominated era, dust starts to dominate with $\rho(z) \sim (1+z)^3$. The energy densities of all the fluids decay, except for that of the cosmological constant ρ_Λ which is constant: thus, at very late times (i.e. low redshift) the cosmological constant dominates in what is called the dark energy dominated era. The MDE occurs between the RDE and the ΛDE. Naturally, an expanding universe was smaller and hotter with denser fluids in the past. When the temperature T is much greater than the mass, $\rho \propto T^4$ for relativistic particles. Thus (from the Friedmann equation (1.92)) during the RDE, $H \propto T^2$. The timescale of the universe is then $\tau_H = H^{-1} \propto T^{-2}$: the hotter the temperature, the younger the universe. The rate of interaction between particles is represented by Γ, which has units of inverse time. When $\Gamma \gg H$, particles have enough time to interact before they are separated through expansion. However, when $\Gamma < H$, the interactions stop and the particles evolve independently, decoupling from each other. Matter-Radiation Equality occurs when the energy densities of the relativistic and non-relativistic fluids agree. This occurs at $z = 3400$. Later, at $z = 1100 - 1400$, electrons and baryons combine to form atoms in the recombination era. Prior to recombination, photons and electrons are tightly coupled via Thomson scattering. Free electrons become scarce during recombination when matter becomes neutral, and Thomson scattering is then inefficient. Photons thus decouple from the rest of matter after recombination at $z = 1000 - 1200$, forming the Cosmic Microwave Background (CMB), a thermal bath of free streaming radiation that permeates the universe. The temperature of the CMB is the common temperature of all matter species in the universe as long as they all remain in thermodynamic equilibrium: when baryons and photons decouple at recombination, their temperature is no longer equal. After photon decoupling, ordinary matter is no longer influenced by radiation and structures can begin to form. Dark Energy-Matter Equality occurs at $z = 0.4$, when Λ starts to dominate the dynamics of the universe.

To explain the behaviour of the universe and its objects, at least two new sources of gravity are required. These are dark matter and dark energy, so called because they are felt only through their gravitational interactions and do not seem to have any significant electromagentic interactions. In

ΛCDM, they compose 95% of the universe. Dark matter is a non-relativistic fluid whose nature is not yet known, however it is standard to assume that it exists. Dark matter is needed to explain the formation and the structure of the universe. The deceleration parameter is defined by

$$q \equiv -\frac{1}{H^2}\frac{\ddot{a}}{a} \quad , \tag{1.120}$$

and today, where $\Omega_{r,0} \sim 10^{-4}$ can be neglected,

$$q_0 = \frac{1}{2}\Omega_{m,0} - \Omega_{\Lambda,0} \quad . \tag{1.121}$$

Because q_0 and $\sum_i \Omega_{i,0}$ are observables, equations (1.106) and (1.121) can be used to determine Λ and $\Omega_{K,0}$. Observations give $q_0 < 0$, which indicates that, in FLRW, the universe is expanding more slowly at larger z than nearby. This is only possible if $\Omega_{\Lambda,0} \neq 0$, that is, $\Lambda \neq 0$. It also means that $\ddot{a} > 0$: the expansion of the universe is accelerating at present, which does not arise from standard sources of gravity. If it is assumed $\Lambda = 0$, for $\ddot{a} > 0$ to be satisfied either gravity needs to be modified, or a non-standard, exotic source of matter called 'dark energy' needs to be introduced.

The concordance model of cosmology, ΛCDM (Λ Cold Dark Matter) is the 'simplest' model that accounts for most (if not all) current observations of the universe from very different epochs, characterizing phenomena such as accelerating expansion, structure formation, big bang nucleosynthesisis (BBN), the lack of curvature, CMB fluctuations and the combination of baryons into atoms. It is the FLRW universe with $\Lambda \neq 0$, some cold dark matter and $K = 0$. It generally contains six free parameters, determined through observations or principles, and five fixed parameters. The pre-recombination model makes assumptions about dark energy and dark matter, with a universe consisting of 63% dark matter, 15% photons, 12% atoms and 10% neutrinos. It is used to predict the physical size of fluctuations in the sound horizon and the baryon density [139]. When this model-predicted fluctuation spectrum is compared to the CMB-observed angular spectrum, the 6 free parameters are set and the ansätze about dark energy and dark matter are tested. All other parameters are determined through calculations. However, there is a problem. The value of the Hubble rate today, the Hubble constant H_0, determined by measurement in the late universe does not concord with the value inferred from the CMB, assuming ΛCDM, in the early universe. This tension, called the 'Hubble tension' or 'H_0 tension', between the early and late universe value has increased over recent years to 4.2σ despite progress in reducing uncertainties and increasing precision. Values obtained through different methods on different data sets support the tension. This suggests there might be something wrong with the current model: the test of a model is how well it reproduces observations. New physics to resolve the tension have been proposed.

This thesis is about the Hubble tension. The ways in which the Hubble constant is measured and inferred are discussed in chapter 2, starting with a broad overview of various methods and results - the latter of which is displayed in figure 2.1. The inference of H_0 from the early universe, particularly the Cosmic Microwave Background (CMB) and Baryon Acoustic Oscillations (BAO) observations, is explained and some results given in section 2.1. Some supplementation to the introduction to distance measurements given in this chapter is provided in section 2.2, after which there is a discussion of the methods and H_0 results from the Type Ia supernova distance ladder in 2.2.1, lensing in 2.2.2

and gravitational waves in 2.2.3. The many solutions that have been proposed to resolve the Hubble tension are introduced in chapter 3, beginning with what requirements a suitable solution needs to meet. Following that is an attempt at categorising the solutions, although this is not intended to be exhaustive. Late time solutions, and why they are unlikely to be successful, are examined in section 3.1. Early Dark Energy and its application to the Hubble tension is discussed in section 3.2. A summary and conclusion appear in chapter 4, which includes placing the tension in a wider cosmological context with a brief overview of related tensions.

Chapter 2

Measurements

An accurate measurement of the Hubble constant H_0 is needed as it is an important part of our understanding of the universe. There are two 'main' ways of measuring H_0. The first is indirect: the inference or prediction of the value from the Cosmic Microwave Background (CMB) as interpreted by ΛCDM. It is a non-local, early universe measurement that is dependent on flat-ΛCDM. The final value obtained by the *Planck* collaboration, released in 2018, is $H_0 = 67.36 \pm 0.54\,\mathrm{km\,s^{-1}\,Mpc^{-1}}$ when the *Planck* data includes CMB lensing [8]. The second way is to directly measure the value using the local distance ladder and Type Ia supernovae (SNIa). It is a local, late universe and model-independent measurement. In 2020, the SH0Es (Supernovae, H_0, for the Equation of State of Dark Energy) collaboration released their most recent value obtained using this method: $H_0 = 73.2 \pm 1.3\,\mathrm{km\,s^{-1}\,Mpc^{-1}}$ [115]. If this is the true expansion rate, the universe may be up to $\sim 10^6$ years younger than previously thought [114].

The latest *Planck* and SH0Es values are in 4.2σ (4.2 standard deviations) tension with each other. This tension has increased from the tensions between earlier results of 3.4σ in 2016 [117] and 3.7σ in 2018 [118]. In 2019 the tension was 4.4σ [116]. The Hubble tension was apparent from the first *Planck* results, which produced $H_0 = 67.3 \pm 1.2\,\mathrm{km\,s^{-1}\,Mpc^{-1}}$ [5], which was in tension with the then recent distance ladder value of $H_0 = 73.8 \pm 2.4\,\mathrm{km\,s^{-1}\,Mpc^{-1}}$ [119]. These are, of course, improvements from the first values obtained when, in 1929, the initial estimates of H_0 indicated that the universe was newer than the Earth and the Sun [114]. Significant work has been performed by the SHOEs team to reduce uncertainties and systematic errors to improve precision, with a goal of achieving a 1% precision measurement of H_0 [115]. The SH0Es data has also been re-analysed multiple times since the project began in 2005, none of which have significantly changed the value of H_0. The precision of late universe H_0 values have improved from 10% twenty years ago [114]; and specifically for the SH0Es distance ladder from to 2.4% in 2016 [117] to 1.8% in 2020 [115]. However, doubt has recently been cast on the accuracy of SH0Es with regard to dust extinction [91] and the choice of Cepheid colour-luminosity calibration [92]. A discussion of systematic errors in SNIa observations that could resolve the Hubble tension if identified and accounted for appears in [120]; however, no such systematics have yet been conclusively identified (as shown in, for example, [4], [77] and [116]). Multiple CMB observations

have been re-analysed and cross-checked: for example, potential systematic errors in the analysis have been tested and found not to affect the H_0 tension in [7]. The precision of the *Planck* 2018 value is 0.8% [8]. Both the early universe (*Planck* CMB) and the late universe (SHOEs) measurements have been supported and checked by independent measurements performed by other groups using different methods and/or data sets, which may all have different systematics. The increase in precision and reduction of errors, combined with the many supporting measurements, strongly suggests that the tension is not a result of observational or calculation errors. Solutions that have been proposed to resolve the tension by adapting ΛCDM are discussed in chapter 3.

The value of H_0 that is obtained from the CMB is indirect because it is not constrained directly by CMB observations, but is inferred by finding the best value to fit the ΛCDM model to the CMB. The CMB H_0 value is non-local because it depends on the entire expansion history. The SNIa distance ladder by comparison is a direct measurement of H_0 because it directly measures the fluxes and luminosities used to obtain distances and therefore H_0 from SNIa. Furthermore, it depends on the local expansion rate and is thus a local measurement. ΛCDM describes the evolution of the late universe and uses this to predict H_0 from the parameters derived using the early model from CMB data. As the predicted H_0 value differs from the late universe value, the tension could signal an error in standard ΛCDM.

Measurements that are independent of the *Planck* CMB data set and the SH0Es distance ladder are important as a check on them. Alternative measurements need to have a high precision comparable to the precision of SH0Es in order to be considered to be either reinforcing the existence of the tension or resolving it by showing it does not exist. Blinded analyses are also important to prevent experimenter bias and provide credibility for results. In a blind analysis, procedures for a measurement are fully established before the data is examined. In this way, decisions regarding the method are not influenced by intermediate results. For credibility for the existence of the Hubble tension or in a resolution of the tension, the authors of [19] insist that all relevant measurements contributing to these must be reproducible and potential causes of their systematic errors thoroughly investigated to ensure their accuracy. This is because 'extraordinary claims, like physics beyond ΛCDM, require extraordinary evidence' [19].

Every determination of H_0 is based on an absolute distance scale to which other distances are compared. For determinations made using the CMB and Baryon Acoustic Oscillations (BAO), this scale is the physical size of the baryon-photon sound horizon at recombination $r_s(z_*)$ obtained from these observations. Instead of using the CMB to set the sound horizon, an alternative method is to derive it by relating the predicted baryon density to measurements of primordial deuterium abundance [114]. The sound horizon predicts the expansion history from $z = 1000$ to $z = 0$ which means that distances cannot be measured directly. The absolute distance scale in the distance ladder is obtained either by geometric parallax to the Milky Way Cepheids or Tip of the Red Giant Branch (TRGB) stars (see figure 2.3); or by the distance to a nearby star galaxy measured using detached eclipsing binaries or via maser emission. The value of H_0 is only as accurate as the value of the absolute distance used in calibration.

The methods to obtain the SH0Es and *Planck* H_0 values are discussed in detail later in this chapter, as well as those of some alternative measurements. They are divided into 'early' and 'late' measurements following the definitions given in [43]. 'Early' measurements are those that are made by early universe ($z > 1000$) physics which are described by ΛCDM; whereas a 'late' measurement is one which is measured in the late universe ($0 < z < 1000$), with or without the inclusion of the late-time behaviour of ΛCDM. 'Early' and 'late' refer to the epoch of the ΛCDM model used (e.g. post- or pre-recombination), not the redshift where the measurement is made. A test is whether or not a measurement depends on the number of neutrinos in ΛCDM: if it does, then it belongs in the 'early' category. Tracing the chain of calibration is also useful in establishing to which category a measurement belongs. In general, early universe measurements give lower values of H_0 than late universe ones - this indicates their corroboration of the *Planck* and SH0Es values.

The underlying method to measuring H_0 directly is to use independent measurements of redshift (to obtain the recession velocity) and distance in Hubble's law (1.22). In 1929, Edwin Hubble made the first H_0 measurement using 18 galaxies with known z and distance of $H_0 = 500\,\mathrm{km\,s^{-1}\,Mpc^{-1}}$ with large errors [72]. He determined the distance to other galaxies by observing their Cepheid variable stars [50]. Measurements of redshift can be made by comparing observed spectra with known spectra for different elements, assuming the latter were the same in the past. Flux is dependent on the distance from the source. For standard candles, flux is related to distance by the inverse square law: intensity $\propto \frac{1}{\text{distance}^2}$. Flux can also be given as μ, the source's apparent magnitude: therefore, magnitude can be used as a proxy for distance. For intrinsically alike, relatively nearby sources, the magnitude is linearly related to redshift [50], like Hubble's law which is a linear relation between velocity v and distance d:

$$v = H_0\, d \quad . \tag{2.1}$$

This is a result of the expansion of the universe [50].

Determining cosmological distances is a challenge because they cannot be measured directly. A distance ladder, a succession of techniques to determine distances, is one way of addressing this. Each rung of the ladder provides information to determine distances at the next rung: local objects with known distances are used to calibrate objects that are further away. In the SH0Es distance ladder, variable stars Cepheids are used to calibrate Type Ia supernovae in the Large Magellanic Cloud (LMC). This distance ladder is discussed further in section 2.2.1. Alternative distance ladders use a different type of star instead of Cepheids to calibrate SNIa; and others substitute another distant object for SNIa. The Carnegie-Chicago Hubble Project (CCHP) [55] calibrate SNIa with Tip of the Red Giant Branch (TRGB) stars instead of Cepheids. TRGB is where peak brightness is acheived by red giant stars when they transition from burning hydrogen to burning helium in the core, and is observed in SNIa host galaxies by the Hubble Space Telescope (HST) up to ~ 20 Mpc. TRGB distance measurements in the LMC are used to calibrate 18 SNIa across 14 host galaxies, with a result of $H_0 = 69.8 \pm 1.9\,\mathrm{km\,s^{-1}Mpc^{-1}}$, which supports the early universe value. Different estimates of dust extinction of the TRGB in the LMC and calibration changes [114] lead to a different result from the TRGB distance ladder of $H_0 = 72.4 \pm 1.9\,\mathrm{km\,s^{-1}Mpc^{-1}}$ [145] which supports the late universe value. Miras are also used instead of Cepheids to calibrate SNIa in distance ladders. Miras are oxygen rich

variable red giant stars that come from older stellar populations and are brighter than Cepheids. They are present in ellipticals and halo spirals. The H_0 value obtained using a Miras-based distance ladder is $H_0 = 73.3 \pm 3.9\,\mathrm{km\,s^{-1}\,Mpc^{-1}}$ [71]. It is anticipated that the TRGB- and Miras-based distance ladders will improve with data from the recently launched James Webb Space Telescope and new Gaia data releases [139].

Surface Brightness Fluctuations (SBF) is an alternative distance ladder which is calibrated by Cepheids or TRGB stars, but is independent of SNIa. This method is based on the fact that the resolution of stars in astrophotography depends on distance: the luminosity of each pixel is due to a given number of stars, and the Poisson fluctuations from one pixel to another depend on the distance to the host galaxy [107]. A recent result using this method is $H_0 = 76.5 \pm 4.0\,\mathrm{km\,s^{-1}\,Mpc^{-1}}$ [139]. The Tully-Fisher relation is a strong correlation between the maximal rotation velocity of spiral galaxies and their absolute luminosity: a brighter, and therefore more massive, galaxy must rotate faster to compensate for the gravitational attraction of its mass [107]. It is used in distance ladders calibrated by TRGB stars and Cepheids. A recent result using the Tully-Fisher relation is $H_0 = 75.1 \pm 2.8\,\mathrm{km\,s^{-1}\,Mpc^{-1}}$ [124]. Type II supernovae (SNII), which are formed by the explosion of massive stars which leads to a residual black hole or neutron star and differ from SNIa in that their optical spectrum includes hydrogen traces [107], can also be used as the last rung of a distance ladder instead of SNIa. A recent result of this is $H_0 = 75.8^{+5.2}_{-4.9}\,\mathrm{km\,s^{-1}\,Mpc^{-1}}$ [37].

There are various direct methods of determining H_0 that do not rely on a distance ladder. The Megamaser Cosmology Project [106] measures $H_0 = 73.9 \pm 3.0\,\mathrm{km\,s^{-1}\,Mpc^{-1}}$ using geometric distance measurements to six megamaser-hosting galaxies which are in the Hubble flow: the distances are measured using observations of water masers orbiting supermassive black holes. The precision of this method is limited by sample size and may not reach below 1% [139]. A method using cosmic chronometers is also independent of a distance ladder. Cosmic chronometers are also called cosmic clocks because they are objects, for example the oldest elliptical galaxies, whose time-evolution is known or well-modelled. This method determines H_0 by finding a change in a cosmic chronometer across a change in redshift, using $H(z) \propto \frac{dz}{dt}$ [43]. A recent value, assuming ΛCDM, is $H_0 = 71.0 \pm 2.8\ \mathrm{km\ s^{-1}\ Mpc^{-1}}$ [139]. There are many systematic uncertainties in all the astrophysics in this method and more work on uncertainties is still needed [43], [139]. Age estimates of the oldest objects in the universe can be combined with measurements of the present day matter density $\Omega_{m,0}$ to determine the Hubble constant: globular clusters give $H_0 = 71 \pm 2.8\,\mathrm{km\,s^{-1}\,Mpc^{-1}}$, whereas very low metallicity stars give $H_0 = 69.3 \pm 2.7\,\mathrm{km\,s^{-1}\,Mpc^{-1}}$ [76]. The use of γ-ray attenuation data under the assumption of flat ΛCDM gives $H_0 = 68.0^{+4.2}_{-4.1}\,\mathrm{km\,s^{-1}\,Mpc^{-1}}$ [46]. Other examples of measuring H_0 without a distance ladder include the expansion of the photospheres of SNII [57] and the Sunyaev-Zel'dovich effect [82]. Lensing is a major method in this category of direct measurements that are independent of a distance ladder - it is discussed in detail further in this chapter in section 2.2.2. The latest lensing result from TDCOSMO IV, which includes information from SLACS (the Sloan Lens ACS sample), is $H_0 = 67.4^{+4.1}_{-3.2}\,\mathrm{km\,s^{-1}\,Mpc^{-1}}$ [19]. It seems to support the early universe value.

Averaging various measurements together in different combinations by excluding a particular

method (distance ladders with: Cepheids, TRGB, Miras or SNIa; lensing), geometric calibration (parallaxes, masers, detached eclipsing binaries) or a team in each combination to avoid overlapping data gives a tension with *Planck* of $4.5 - 6.3\sigma$ [114]. A similar averaging is performed in [139] which finds tension between the early and late universe of $4 - 5.8\sigma$. This suggests that the the tension is both highly significant and does not seem to be the fault of an error with any one method or calibration. Even if there are multiple systematic errors in the different measurements, taking them into account is unlikely to resolve the Hubble tension [43].

The inverse distance ladder uses absolute distance measurements from lensing or BAO calibrated by the CMB at high redshift as an anchor for the supernovae relative distances, and then extrapolates to $z = 0$, assuming a prior on the sound horizon at recombination $r_s(z_*)$. Using an inverse distance ladder and blinded analysis on BAO, Dark Energy Survey (DES) and low-z SNIa data results in $H_0 = 67.8 \pm 1.3\,\mathrm{km\,s^{-1}\,Mpc^{-1}}$ [88], which is consistent with *Planck*.

Most of the values of H_0 that appear in this chapter are shown in figure 2.1, divided into the early and late universe with the 'main' *Planck* and SH0Es 2020 data shown as shaded bars for comparison. In general, the early universe values agree with the *Planck* value and the late universe values agree with the SH0Es 2020 value. However, many of the late universe values have much larger error bars than the early universe values, and some agree with the *Planck* value but do not have good enough precision to resolve the tension.

The rest of this chapter is divided into discussions of early universe measurements in section 2.1 and late universe measurements in section 2.2. In the early universe section, the inference of H_0 from the CMB and BAO is explained. In the late universe section is a summary of distance cosmology, followed by a discussion of the SNIa distance ladder in section 2.2.1; the determination of H_0 from gravitational time delays, referred to as 'lensing' in 2.2.2, with a summary of the different lensing results in figure 2.6; and then finally gravitational waves in section 2.2.3.

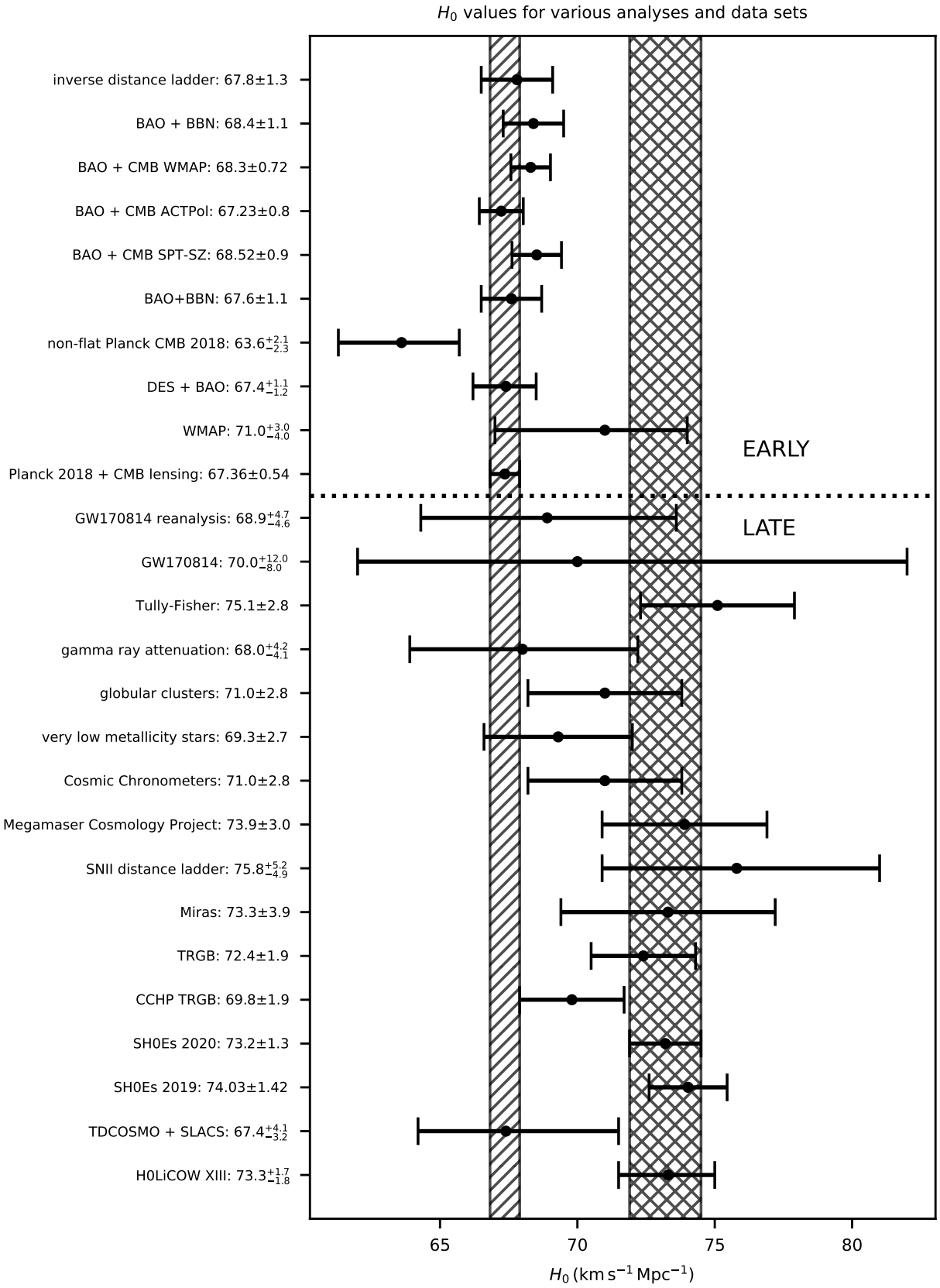

Figure 2.1: Many of the values of H_0 that appear in chapter 2, divided into early and late universe values. The shaded bar represents the *Planck* CMB value, while the cross-hatched bar represents the SH0Es 2020 value.

2.1 Early universe measurements

Prior to recombination, hot hydrogen and helium plasma oscillated between the competing effects of gravitational collapse and radiation pressure [50]. This resulted in density waves in the plasma with a relativistic sound speed that allowed them to propagate over cosmological distances: they did so until free electrons and protons combined to form neutral atoms. The photons were then free to stream out of the baryonic density fluctuations to form the cosmic microwave background (CMB). The reduced photon pressure resulted in a decrease of the sound speed of the density waves, which were then frozen into the distribution of baryonic gas at the last scattering surface $z \approx 1100$. As the gas cooled and formed stars and galaxies, the memory of the early plasma waves imprinted into the large scale distribution of galaxies, causing small oscillations in the galaxy power spectrum called the Baryon Acoustic Oscillations (BAO). The BAO evolves with redshift whereas oscillations imprint in the CMB at the redshift of decoupling only. BAO is a standard ruler (i.e. absolute distances are known) and it can probe greater redshifts than SNIa. BAO can be understood with linear analysis, and is independent of the highly nonlinear astrophysics of individual objects like supernovae or galaxies [50].

The angular scale θ_*, the angular size of the sound horizon, shown in figure 2.2, corresponds to how far a plasma sound wave could have travelled before the epoch of recombination. It is related to the baryon-photon sound horizon r_s and the angular distance D_A to the redshift when photons and baryons decouple $z_* \approx 1100$ as

$$\theta_* = \frac{r_s}{D_A(z_*)} \quad , \tag{2.2}$$

where the definitions of r_s and $D_A(z_*)$ are

$$r_s = \int_{z_*}^{\infty} \frac{c_s \, dz}{H(z)} \quad \text{and} \tag{2.3}$$

$$D_A(z_*) = \int_0^{z_*} \frac{dz}{H(z)} \quad . \tag{2.4}$$

The sound horizon depends on c_s, the sound speed at which the acoustic waves travel in the plasma, which depends on the ratio of the baryon and photon densities ρ_b, ρ_γ, and is given by

$$c_s = \frac{1}{\sqrt{3\,(1 + 3\rho_b/4\rho_\gamma)}} \quad . \tag{2.5}$$

Big Bang Nucleosynthesis (BBN) gives the ratio of baryonic matter to radiation in the universe, and the CMB is then used to infer the amount of radiation.

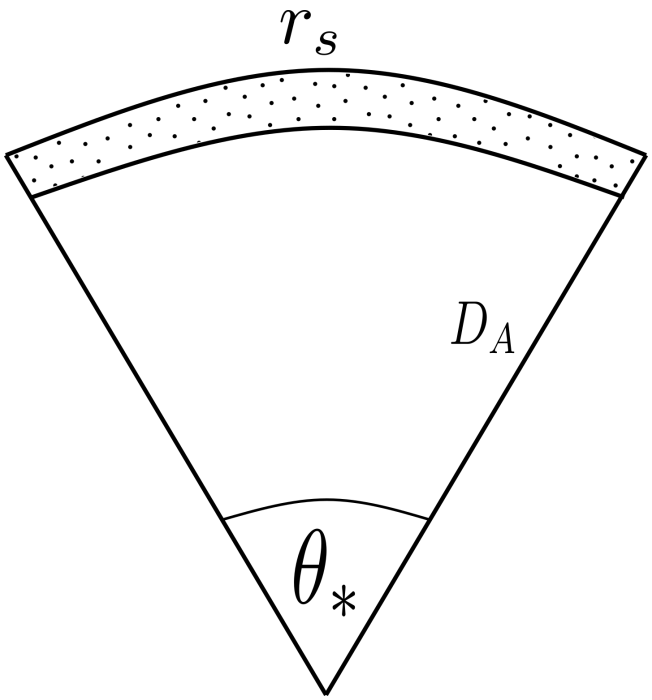

Figure 2.2: The angular scale θ_* is the angle subtended by the sound horizon r_s at decoupling and the angular diameter distance D_A. The dotted section represents the surface of last scattering.

The angular scale is precisely known from CMB anisotropies and can be directly read off the peak spacing of the CMB as

$$\theta_* = \frac{\pi}{\Delta\ell} \quad , \tag{2.6}$$

where ℓ are CMB modes [81]. It is clear from equation (2.4) that $D_A(z_*)$ is sensitive to $H(z)$ at late times (post-recombination); whereas in equation (2.3) r_s is sensitive to $H(z)$ at early times (pre-recombination). This shows that r_s is independent of H_0. From equations (2.2) - (2.4), the angular scale is proportional to H_0 as

$$\theta_* \propto r_s\, H_0 \quad , \tag{2.7}$$

and the value of r_s is needed in order to infer H_0 from the CMB. In summary: H_0 is estimated from CMB data, assuming a model, by first deriving r_s at z_* from measurements of baryon and matter density; θ_* is read off the CMB peaks and $D_A(z_*)$ is derived from (2.2); then $H(z)$ is derived from (2.4). Similarly, the angular scale for the BAO is related to the comoving sound horizon r_s at decoupling, which is provided by the BAO scale, and the average angular diameter distance to a sample of galaxies used for measurement $D_A(z_{\rm gl})$ as:

$$\theta_{\rm BAO} = \frac{r_s}{D_A(z_{\rm gl})} \quad . \tag{2.8}$$

The above shows that the inference of H_0 from CMB and BAO data is only as good as the knowledge of the baryon-photon sound horizon. As will be discussed in chapter 3, many attempts at resolving the Hubble tension involve increasing the value of r_s by adjusting the early physics and background parameters, such as the density of matter and baryons, in order to realise a higher CMB-inferred H_0 value. The sound horizon r_s is constant after recombination: the tension is mostly independent of $H(z)$ between $z \sim 0.7$, the redshift of BAO observations, and recombination. Thus, a proposed

solution that significantly changes the value of the early universe H_0 to resolve the Hubble tension should rely on new physics before recombination.

The Hubble constant is not a free parameter: the Friedmann equation (1.92) shows that it cannot be varied independently of the matter content of the universe. The influence of H_0 on the angular power spectrum of the CMB depends on the dimensionless densities that are kept constant when its value is varied. If the early H_0 is decreased, matter-radiation equality occurs later, which increases the amplitude of the acoustic peaks in the CMB [107].

The CMB allows a precise and indirect inference of H_0 to be made under the assumption of a cosmological model. The angular size of the sound horizon and constraints on the energy density of each component of the ΛCDM model derived from the *Planck* 2018 analysis of the CMB give a value of $H_0 = 67.36 \pm 0.54\,\mathrm{km\,s^{-1}\,Mpc^{-1}}$ [8]. This is for a fit of flat ΛCDM to the CMB. A fit of the non-flat ΛCDM to the CMB results in $H_0 = 63.6^{+2.1}_{-2.3}\,\mathrm{km\,s^{-1}\,Mpc^{-1}}$ [8]. The *Planck* CMB observations give the best current calibration of ΛCDM parameters which give the most precise estimate of H_0; however the observations rely on the assumptions that ΛCDM makes about the nature of dark matter, dark energy and relativistic particles. Thus, the Hubble tension appears to indicate some inaccuracy or omission in the ΛCDM model.

The Hubble constant is inferred from BAO using equation (2.8): it is the same way as from the CMB, but without the CMB anisotropy data. A measurement of the baryon density in the early universe inferred from BBN data is combined with late universe measurements of matter density to calibrate the BAO-measured sound horizon to give a value of H_0. This method, independent of the CMB and distance ladder, is anchored in the early universe using a combination of galaxy clustering and weak lensing measurements from the Dark Energy Survey (DES) data, BAO from the Baryon Oscillation Spectroscopic Survey (BOSS) and BBN measurements gives a result of $H_0 = 67.4^{+1.1}_{-1.2}\,\mathrm{km\,s^{-1}\,Mpc^{-1}}$ [3] - a nearly identical value to the *Planck* CMB value but with error bars of double the size.

Other sets of data combined with BAO data give varying values of H_0. BOSS BAO data analysed with a weak BBN prior gives $H_0 = 67.6 \pm 1.1\,\mathrm{km\,s^{-1}\,Mpc^{-1}}$ [35]. Under the assumption of flat ΛCDM, a combination of the full-shape analysis of BAO in the BOSS data set and BBN data gives a 1.6% precision measurement of $H_0 = 68.6 \pm 1.1\,\mathrm{km\,s^{-1}\,Mpc^{-1}}$ [108]. Galaxy and Lyman-α forest BAO data together with a precise estimate of the primordial deuterium abundance result in $H_0 = 66.98 \pm 1.18\,\mathrm{km\,s^{-1}\,Mpc^{-1}}$ for flat ΛCDM [4]. Note that the above four results are completely independent of the CMB. The following three results combine BAO data sets with CMB data that do not come from *Planck*: SPT-SZ (South Pole Telescope SZ camera) CMB data gives $H_0 = 68.52 \pm 0.9\,\mathrm{km\,s^{-1}\,Mpc^{-1}}$; CMB data from ACTPol (Atacama Cosmology Telescope Polarization camera) results in $H_0 = 67.23 \pm 0.8\,\mathrm{km\,s^{-1}\,Mpc^{-1}}$; and Wilkinson Microwave Anisotropy Probe (WMAP) CMB data gives $H_0 = 68.30 \pm 0.72\,\mathrm{km\,s^{-1}\,Mpc^{-1}}$ [4]. The result from the WMAP CMB data set alone is $H_0 = 71^{+4}_{-3}\,\mathrm{km\,s^{-1}\,Mpc^{-1}}$ [134]. Early universe inferences of H_0 tend to be larger than the *Planck* value when CMB polarization (EE) data, BAO data or additional freedoms in ΛCDM are included in the analysis [43]. When the BAO are calibrated with supernovae from the Pantheon

compilation, the BAO sound horizon measurement is in tension with the CMB value [105].

2.2 Late universe measurements

The test of ΛCDM and the assumptions made in it is a late universe measurement of H_0 that is independent of the CMB and has a 1% precision that is comparable to that of the *Planck* CMB value. This section will discuss some of the ways astronomers have attempted to do this.

Distances to objects in small regions around the sun are measured as proper distances, which are instantaneous distances between source and observer at the time of detection and are expressed in parsecs. Cosmological distances in an expanding universe are a different matter. It takes a long time for light from distant objects to reach us, and their separation from us may be much more than when it was emitted (indeed, the object may no longer exist!). For local measurements, the immediate separation between us and an object makes sense but not for greater distances. The redshift z of the spectrum of light emitted by an object is a different measurement of separation. Larger redshifts imply larger distances. Redshift is defined in equations (1.44) and (1.47). A measurement of redshift is performed by identifying the absorption or emission lines for certain elements in the spectra of distant objects, measuring their wavelengths and then comparing this with the wavelengths of the absorption or emission lines.

What is the appropriate way to measure distance when the separation is so vast on cosmological scales? The coordinate distance cannot be measured and neither can the proper distance: because light travels along null lines, the proper distance is 0 between emission and observation. Instead, measurements of the luminosity of objects in nearby galaxies are used to infer the distances to them, which were introduced in chapter 1.

In FLRW, the angular and luminosity distances are given by

$$D_A = \frac{1}{1+z}\, f\left(\int_0^z \frac{dz'}{H(z')}\right) \quad , \tag{2.9}$$

$$D_L = (1+z)\, f\left(\int_0^z \frac{dz'}{H(z')}\right) \quad . \tag{2.10}$$

with, as in (1.11),

$$f(\chi) = \begin{cases} \frac{1}{\sqrt{K}} \sin(\sqrt{K}\,\chi) & K > 0 \\ \chi & K = 0 \\ \frac{1}{\sqrt{-K}} \sinh(\sqrt{-K}\,\chi) & K < 0 \end{cases} \quad . \tag{2.11}$$

Using (1.104), and noting from (1.105) that $K > 0$ if $\Omega_{\text{total}} > 1$, the luminosity distance as a function of redshift in FLRW spacetime with $K > 0$ is given from (2.10) as

$$D_L = \frac{1+z}{H_0\sqrt{-\Omega_{K0}}} \sin\left(\sqrt{-\Omega_{K0}} \int_0^z \frac{H_0\, dz'}{H(z')}\right) \quad . \tag{2.12}$$

The equation for the source's observed or apparent magnitude is

$$\mu = -2.5 \log_{10} \Phi + \text{constant} \quad . \tag{2.13}$$

Substituting (1.68) into this leads to

$$\mu = -2.5\log_{10} L_{\text{source}} + 5\log_{10} D_L + \text{constant} \tag{2.14}$$

$$\mu = M + 5\log_{10} D_L + \text{constant} \quad , \tag{2.15}$$

where the source's intrinsic or absolute magnitude is

$$M \equiv -2.5\log_{10} L_{\text{source}} \quad . \tag{2.16}$$

This shows that the luminosity distance $D_L(z)$ is directly observable from flux measurements. The expansion history $H(z)$ is given by [50] as

$$\frac{H^2(z)}{H_0^2} = \Omega_{r,0}\,(1+z)^4 + \Omega_{m,0}\,(1+z)^3 + \Omega_{K,0}\,(1+z)^2 + \Omega_{DE,0}\exp\left(3\int_0^z \left[\frac{1+w(z')}{1+z'}\right] dz'\right). \tag{2.17}$$

The source's absolute and observed magnitudes, μ and M, constrain $D_L(z)$ and thus constrain $H(z)$ for a given $\Omega_{K,0}$ and dark energy with equation of state $w(z)$.

2.2.1 Type Ia supernova distance ladder

The Hubble Space Telescope, a telescope that has been orbiting the Earth since 1990, was the first tool that was able to measure Cepheids further away than a few Mpc. The final result of the Hubble Space Telescope Key Project [54] using Cepheid distances with a variety of methods and objects (namely, SNIa, Tully-Fisher relation, SBF, SNII and the fundamental plane) was $H_0 = 72 \pm 8\,\text{km}\,\text{s}^{-1}\,\text{Mpc}^{-1}$, which improved to $H_0 = 74.3 \pm 2.1\,\text{km}\,\text{s}^{-1}\,\text{Mpc}^{-1}$ when recalibrated to use improved geometric distance calibrations to the LMC [56]. The SH0Es project, begun in 2005, is an advanced distance ladder consisting of improved geometric distances to: the LMC using detached eclipsing binaries, the host galaxy NGC 4258 using water masers, and Milky Way Cepheids using European Space Agency (ESA) Gaia parallaxes.

From (1.68), a measurement of the flux Φ leads to an inference of the absolute luminosity of a source. If the luminosity is already known and the object is a standard candle, a measurement of the flux leads to an inference of the luminosity distance $D_L(z)$. The luminosity of an object can be known from theoretical modelling or from reliably calibrated distances to nearby examples of it. The distance ladder starts at the nearest stars, whose distances are measured by parallax, and continues to very distant galaxies. Parallax is a geometric distance measurement to nearby stars that is independent of luminosity. As the Earth orbits the Sun, the apparent change over six months in the sky position of nearby stars as they appear to move with respect to more distant objects can be calculated. This is the parallax distance and is shown in figure 2.3. The parallax distance is inversely proportional to the parallax angle p: stars that are closer to us have a larger parallax angle. This means that the parallax can be measured to any visible object but is only useful within part of the Milky Way [114]: otherwise the angle is too small to be measured accurately.

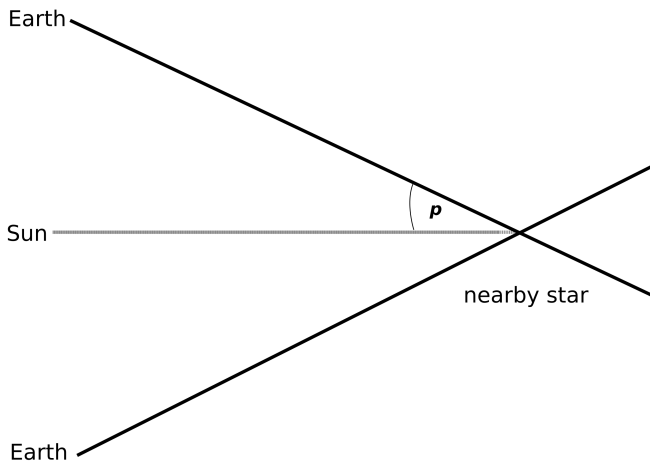

Figure 2.3: The parallax distance is obtained by calculating the apparent change over six months in the position of nearby stars as the Earth orbits the Sun.

The distance ladder is made up of brightness measurements. For each rung, a standard candle is identified. The object on the next rung is calibrated by the previous one, which allows objects at greater distances to be observed. In the SH0Es distance ladder, Cepheids are used to calibrate the luminosity curves of Type Ia supernovae in the LMC. Cepheids are young and bright variable supergiant stars that are abundant in nearby and spiral galaxies. Their external atmosphere pulses with a period of 2-100 days: this pulsation period is independent of distance and is correlated to the intrinsic luminosity of the star through Leavitt's law [107], also called the period-luminosity relation, which can be converted to the period-magnitude relation:

$$M \approx -3[\log_{10}(P) - 1.0] - 4 \quad , \tag{2.18}$$

where P is the period of the star and M its absolute magnitude. The exact expression depends on the photometry [89]. The luminosity and absolute magnitude are related through equation (2.16). The luminosity of Cepheids is bright enough that they are visible with the HST up to 40 Mpc. Type Ia supernovae are supernovae without hydrogen lines in their optical spectrum. SNIa originate from binary systems where one of the stars is a white dwarf which accretes material from its companion until its mass exceeds the Chandrasekhar mass limit of $1.4\,M_{\odot}$. Then it collapses and explodes in a supernova. The luminosity of an individual supernova is equivalent to or brighter than that of an entire galaxy ($\sim 10^6\,L_{\odot}$), which allows them to be observed up to several hundred Mpc. Supernovae are the brightest objects in the distance ladder. They are also rare, only occurring once in a century in a typical galaxy, and so are the last rung of the distance ladder [43]. SNIa allow the Hubble diagram to be extended to large redshifts ($z \sim 2$ and further) for which the luminosity-distance relation is no longer viable [107].

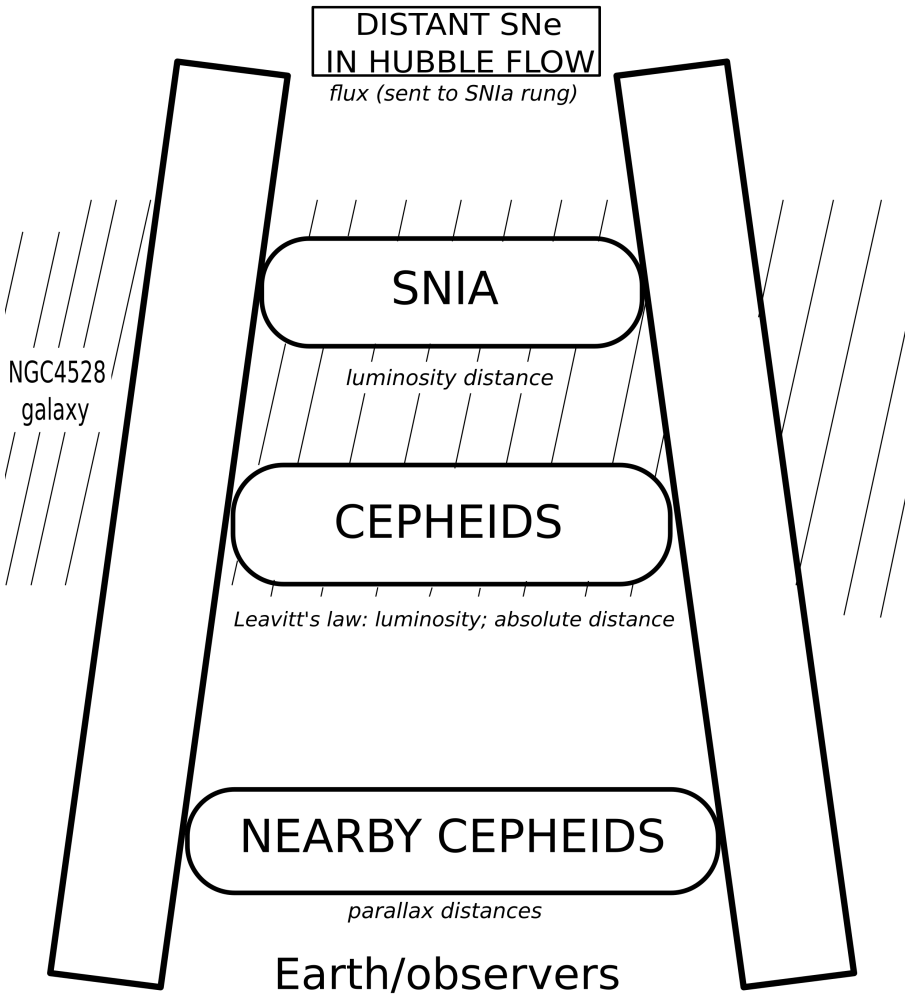

Figure 2.4: The Type Ia supernova distance ladder. The distances from Earth to nearby Cepheids, the first rung on the ladder, are obtained using parallax. The parallax distances are used to calibrate Cepheids in galaxy NGC4258, the second rung on the ladder. The period measurements of the Cepheids are converted into luminosity measurements which are used to obtain the absolute distance to the galaxy. The absolute distance to the galaxy calibrates SNIa in NGC4258, the final rung on the ladder. The flux from distant SNe in the Hubble flow is used to to obtain the luminosity distance $D_L(z)$ to the SNIa.

The SHOEs distance ladder, shown in figure 2.4, starts when distances to nearby Cepheids are obtained using parallax. These distances are used to calibrate Cepheids that are in the same galaxy as the SNIa. Leavitt's law (2.18) is used to convert the Cepheids' period measurements into luminosity measurements. This luminosity is then used to obtain the absolute distance to the galaxy, which in turn is used to calibrate the SNIa. The flux from distant supernovae in the Hubble flow is then used to obtain the luminosity distance $D_L(z)$ to the SNIa via equation (1.68). This and the recession velocity of the galaxy obtained from the redshift finally give H_0 via Hubble's law (1.22). Note that the distance ladder does not directly measure H_0: it directly measures the absolute luminosity of SNIa, or, equivalently, the distance modulus $\mu - M$ which is given by equation (2.15).

Questioning the existence of the Hubble tension, [112] indicates that the H_0 value from the SNIa distance ladder varies depending on the SNIa catalogue used.

2.2.2 Lensing

The light rays emitted by a source, a background object such as a supernova or quasar, are affected by the gravitational potential of a mass in between the source and the observer, called the lens. The source is thus observed at different positions to where it actually is, as images. For the purposes of measuring H_0 the source is usually a quasar - the reasoning for this is discussed later in this section. The light rays emitted by lensed a source take different paths, that have different lengths and pass through different gravitational potentials, to arrive at different image positions – that is, arrive at an observer at different times. The difference in the time the light rays take to arrive is called the time delay Δt. H_0 is inversely proportional to absolute scales of the universe, and as such $\Delta t \propto H_0^{-1}$ [19]. Time delays rely on late universe physics only, so lensing provides a late measurement of H_0 that is independent of the CMB and distance ladders. This alternative measurement of H_0 to SH0Es and *Planck* is important as it does not share any source of systematic uncertainty with them [105], and the distances lensed objects are observed at are larger than those found in the distance ladder [141]. The observables required to obtain H_0 from lensing are: the time delay Δt, the distance between the observer and the source D_s, and the distance between the observer and the lens D_l. If the brightness of the source varies with time on short scales (weeks - months [121]), the time delay can be measured by observing the fluxes of the images [141]. The distance between the lens and the source D_{ls} is also required - it cannot be directly determined from observations but can be derived from D_l and D_s. In addition to these, a lens of the model is needed.

For a source a distance D_s from the observer that is lensed by a lens a distance D_l from the observer, as shown in figure 2.5, the lens equation is

$$\beta = \theta - \alpha(\theta) \quad , \tag{2.19}$$

where β, θ and α are the 2-D vectors on the plane of the sky of, respectively, the source plane, the image plane and the change between the original unlensed and the lensed observed position on the sky of the object. For a single lensing plane,

$$\beta = \theta - \frac{D_s}{D_{ls}}\,\hat{\alpha}(\theta) \quad , \tag{2.20}$$

where $\hat{\alpha}$ is the physical deflection angle. The lensing potential ψ, defined by

$$\alpha(\theta) = \nabla\psi(\theta) \quad , \tag{2.21}$$

defines the lensing convergence

$$\kappa(\theta) = \frac{1}{2}\,\nabla^2\psi(\theta) \quad . \tag{2.22}$$

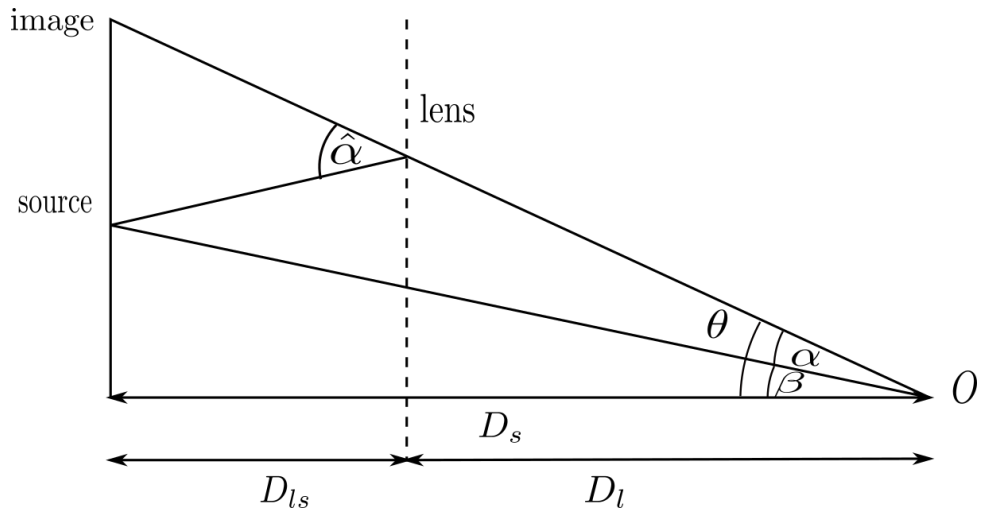

Figure 2.5: The observation of a lensed source. D_s and D_l are the distances from the observer to the source and the lens respectively; D_{ls} is the distance between the source and the lens; β is the angular position on the sky of the source; θ is the angular position on the sky of the image (where the lensed source is observed); and $\hat{\alpha}$ is the physical deflection angle.

The possibility of determining H_0 from lensed galaxies was first proposed by Refsdal in 1964 [113]. Refsdal suggested that for a supernova lensed by a galaxy located between it and an observer, the difference in time that light from the supernova takes to travel along the two paths it follows to the observer, Δt, could be measured and used to calculate the Hubble parameter. Refsdal showed that the Hubble parameter could be expressed by observable quantities only: Δt, the redshifts of the source z_s and the lens z_l (which are assumed to be small), the luminosities of the images L_1 and L_2 and the angles θ_1 and θ_2 at which the images are observed, which sum to θ. Refsdal expressed the Hubble parameter first as

$$H = \frac{z_s \, z_l \, \theta \, (\theta_1 - \theta_2)}{\Delta t \, (z_s - z_l)} \quad . \tag{2.23}$$

The angles θ_1 and θ_2 are almost equal, so their difference would be difficult to measure, Refsdal instead used the luminosities of the images L_1 and L_2. Using the notation $\dfrac{L_1}{L_2} = \dfrac{L_1(t)}{L_2(t+\Delta t)}$, the difference between the angular positions of the images can be expressed as follows:

$$\frac{L_1}{L_2} = \frac{\theta_1^2}{\theta_2^2} \quad \Rightarrow \quad \theta_1 = \theta_2 \sqrt{\frac{L_1}{L_2}} \quad \text{and} \quad \theta_1 = \frac{\theta_1}{\sqrt{\frac{L_1}{L_2}}} \quad ; \tag{2.24}$$

$$\theta = \theta_1 + \theta_2 \quad \Rightarrow \quad \theta_1 = \theta - \theta_2 \quad \text{and} \quad \theta_2 = \theta - \theta_1 \quad . \tag{2.25}$$

Substituting equation (2.25) into equation (2.24) results in

$$\theta_1 = \frac{\theta \sqrt{\frac{L_1}{L_2}}}{\sqrt{\frac{L_1}{L_2}} + 1} \quad \text{and} \quad \theta_2 = \frac{\theta}{\sqrt{\frac{L_1}{L_2}} + 1} \quad . \tag{2.26}$$

Then,

$$\theta_1 - \theta_2 = \theta \, \frac{\sqrt{\frac{L_1}{L_2}} - 1}{\sqrt{\frac{L_1}{L_2}} + 1} \quad . \tag{2.27}$$

The equation for the Hubble parameter in terms of the luminosities of the images, the redshifts of the source and the lens, the time delay, and the sum of the angular positions of the images can then be obtained by substituting equation (2.27) into (2.23) as

$$H = \frac{z_s\, z_l\, \theta^2}{\Delta t\, (z_s - z_l)} \frac{\sqrt{\frac{L_1}{L_2}} - 1}{\sqrt{\frac{L_1}{L_2}} + 1} \quad . \tag{2.28}$$

Present day lensing determinations of H_0 use the distances D_l, D_s and D_{ls} described in the introduction to this section instead of the luminosities that Refsdal used. Refsdal made the assumptions that the lens is spherically symmetric, and that the redshifts of the supernova and the lens are small. Most galaxies are not spherically symmetric and so information about the mass distribution of the lens needs to be included in the lens model. Modern lens models are far more complicated and are matched to observations.

The following is drawn from [33] and uses the FLRW metric (1.1). The dimensionless distance between the source and an observer at the lens is

$$D(z_l, z_s) \equiv (1 + z_s)\, H_0\, D_A(z_l, z_s) \quad , \tag{2.29}$$

where $D_A(z_l, z_s)$ is the angular diameter distance (1.78) of a source as observed at the lens. Using (1.104) to obtain $\sqrt{\Omega_{K,0}} = -\dfrac{K}{H_0^2}$ and the FLRW metric, equation (2.29) can be written

$$D(z_l, z_s) = \frac{1}{\sqrt{\Omega_{K0}}} \sinh\left(\sqrt{\Omega_{K0}} \int_{t_s(z_s)}^{t_l(z_l)} \frac{H_0}{a(t)}\, dt \right) \quad . \tag{2.30}$$

Denoting $D(z) \equiv D(0, z)$, $D_l \equiv D(z_l)$ and $D_s \equiv D(z_s)$, equation (2.30) is simplified to:

$$D_{ls} \equiv D(z_l, z_s) = D_s \sqrt{1 + \Omega_{K,0}\, D_l^2} - D_l \sqrt{1 + \Omega_{K,0}\, D_s^2} \quad . \tag{2.31}$$

In this way D_{ls} can be obtained from observations of D_l and D_s.

The time photons arrive at the observer depends on the path length and the gravitational potential $\psi(\theta)$ the light rays pass through, the latter of which is determined from a mass model of the system. In strong lensing, the light ray from a source splits into several bundles. The difference in the arrival times t_1 and t_2 of two light bundles at angular coordinates θ_1 and θ_2 on the sky is

$$\Delta t(\theta_1, \theta_2) = \frac{1}{H_0} \frac{D_l D_s}{D_{ls}}\, f(\theta_1, \theta_2) \quad , \tag{2.32}$$

where $f(\theta_1, \theta_2)$ depends on the structure of the lens. Given observations of Δt, D_l, D_s, $\Omega_{K,0}$ and a lens model, H_0 can be found using equation and (2.32) as

$$H_0 = \frac{D_l\, D_s}{D_{ls}} \frac{f(\theta_1, \theta_2)}{\Delta t} \quad . \tag{2.33}$$

The excess time delay of an image is given by [121] as

$$t(\theta, \beta) = \frac{D_{\Delta t}}{c} \left[\frac{(\theta - \beta)^2}{2} - \psi(\theta) \right] \quad , \tag{2.34}$$

where $D_{\Delta t}$ is the the time delay distance

$$D_{\Delta t} \equiv (1 + z_l) \frac{D_l \, D_s}{D_{ls}} \quad . \tag{2.35}$$

The time delay of the two images is the difference between their excess time delays [19]:

$$\Delta t = \frac{D_{\Delta t}}{c} \left(\phi(\theta_1, \beta) - \phi(\theta_2, \beta) \right) \quad , \tag{2.36}$$

where ϕ is the Fermat potential

$$\phi(\theta, \beta) = \left[\frac{(\theta - \beta)^2}{2} - \psi(\theta) \right] \quad . \tag{2.37}$$

When constraints on the lensing potential are provided, the time delay distance in equation (2.36) becomes [19]:

$$D_{\Delta t} = \frac{c \, \Delta t}{\Delta \phi} \quad . \tag{2.38}$$

H_0 is inversely proportional to $D_{\Delta t}$ as $D_{\Delta t} = \dfrac{cz}{H_0}$ [19], therefore H_0 can be determined through

$$H_0 = \frac{z \, \Delta \phi}{\Delta t} \quad . \tag{2.39}$$

Strong lensing time delays between multiple images of lensed quasars are used in determining the Hubble constant. To avoid bias on the part of experimenters, best practice is to construct a lens model for each system individually to enable blind analysis [139]. More recent results employ this. The results from each individual lens are combined to obtain stronger constraints. The more lenses used, the better the precision obtained. STRIDES (STRong-lensing Insights into Dark Energy Survey) analysed one single quadruply lensed quasar resulting in measurement of $H_0 = 74.2 \pm 3.0 \, \mathrm{km\,s^{-1}\,Mpc^{-1}}$ with 3.9% precision [129]. Using three lenses, SHARP (Strong-lensing High Angular Resolution Programme) obtained $H_0 = 76.8 \pm 2.6 \, \mathrm{km\,s^{-1}\,Mpc^{-1}}$ [28]. The HOLiCOW team were a major collaboration in finding H_0 using lensing: H0LiCOW stands for H_0 Lenses in COSMOGRAIL's Wellspring, with COSMOGRAIL standing for COsmologial MOnitoring of GRAvitational Lenses. H0LiCOW analysis is completely independent of the SNIa distance ladder and the CMB. H0LiCOW XII [121] is the blind analysis of one quadruply-imaged gravitationally lensed quasar, with a 6.6% precision result of $H_0 = 71.6^{+3.8}_{-4.9} \, \mathrm{km\,s^{-1}\,Mpc^{-1}}$. With four lenses, H0LiCOW IX [18] determined $H_0 = 72.5^{+2.1}_{-2.3} \, \mathrm{km\,s^{-1}\,Mpc^{-1}}$, a 3% precision determination.

H0LiCOW XIII [141] is a joint analysis of six gravitationally lensed quasars with measured time delays. All lenses except one are analyzed blindly. H_0 in each lens individually is measured to a precision of $4.3 - 9.1\%$. In the joint analysis, the Hubble constant found in flat ΛCDM is $H_0 = 73.3^{+1.7}_{-1.8} \, \mathrm{km\,s^{-1}\,Mpc^{-1}}$. This 2.4% precision value agrees with the SH0Es 2020 value, and is in 3.1σ tension with the *Planck* CMB value. In [90], all six lenses are reanalysed blindly, and the the precision improves to $\sim 2\%$ [19].

The TDCOSMO collaboration is formed by members of H0LiCOW, STRIDES, COSMOGRAIL and SHARP, and has reanalyzed their lens systems to obtain new values of H_0 with a focus on the inclusion of all uncertainties. The dominant source of residual uncertainty in lensing is the mass-sheet

transform (MST) – a discussion of the MST appears later. TDCOSMO deals with the effect of the MST differently than H0LiCOW. The time delays in the TDCOSMO IV [19] sample of seven lensed quasars (6 from H0LiCOW) gives $H_0 = 74.5^{+5.6}_{-6.1}\,\mathrm{km\,s^{-1}\,Mpc^{-1}}$. The inclusion of observations of kinematics from an independent set of 33 gravitational lenses in the Sloan Lens ACS sample (SLACS) to constrain the galaxy lens mass profiles substantially lowers the value to $H_0 = 67.4^{+4.1}_{-3.2}\,\mathrm{km\,s^{-1}\,Mpc^{-1}}$ [19]. This is performed under the assumption that the TDCOSMO and SLACS galaxies are originate in the same underlying parent population in terms of mass profiles and kinematic properties. H0LiCOW, TDCOSMO and TDCOSMO + SLACS agree statistically; and the TDCOSMO-only analysis is consistent with H0LiCOW/STRIDES/SHARP, the only difference being a significantly larger uncertainty, which is expected because of the reduced assumptions. The addition of SLACS to TDCOSMO reduces the uncertainty to 5% and reduces H_0 by ~ 6. The collaboration suggests that the reason for the lower value could be either that elliptical galaxies are more radially anisotropic than the prior used to model TDCOSMO galaxies, or that TDCOSMO and SLACS galaxies are different. The late universe TDCOSMO + SLACS H_0 value agrees with the early universe value; however, the uncertainties are so large that it cannot be said to resolve the Hubble tension.

The different H_0 values and the varying sizes of their uncertainties obtained using lensing data are depicted graphically in the top half of figure 2.6. It is clear that the large uncertainties mean it is difficult to compare lensing results with the high precision SH0Es and *Planck* values; and thus they do not contribute much to the Hubble tension debate beyond that the values tend to be large like the late universe SNIa distance ladder value.

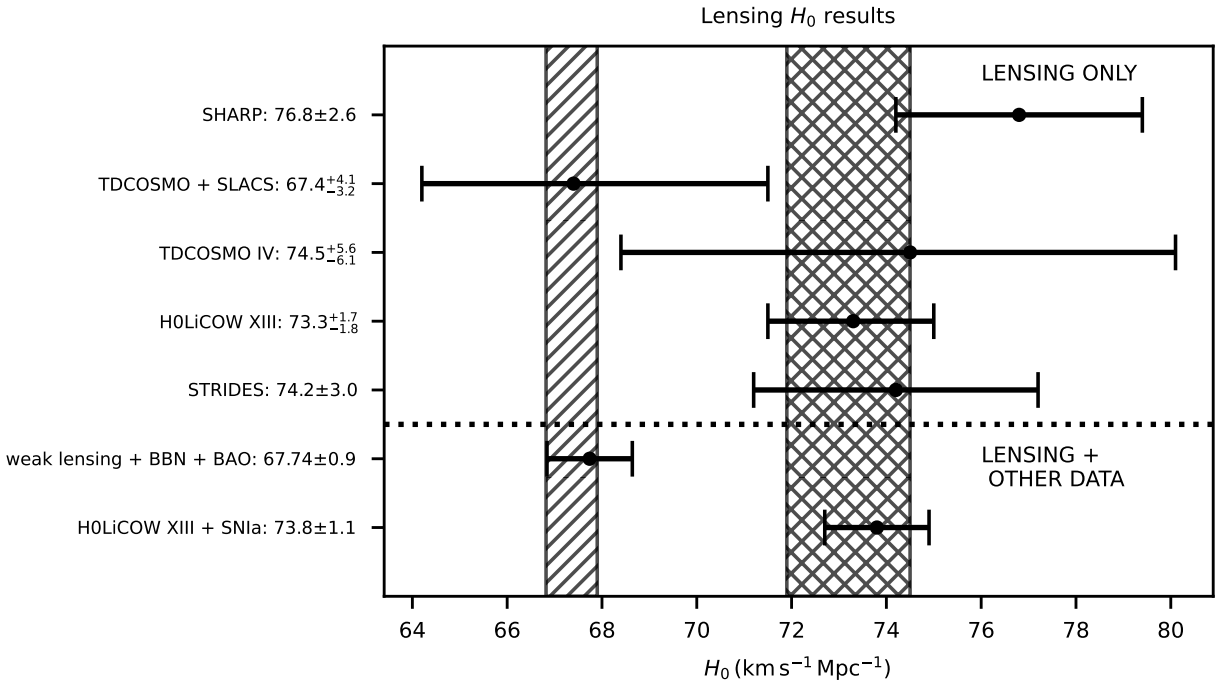

Figure 2.6: The values of H_0 found using lensing data, divided into those found using only lensing data and those determined with lensing data in combination with other data sets. The shaded region represents the *Planck* CMB value, while the cross-hatched region represents the SH0Es 2020 value.

The combination of constraints from lensing and other probes improves the precision and reduces the uncertainty of H_0 results, as can be seen in figure 2.6 which shows H_0 from lensing data only as well as H_0 from lensing data combined with data from other sources. When the H0LiCOW XIII analysis time delay distances are used to anchor the SH0Es SNIa distance ladder - something that can be performed because the two data sets are independent of each other - the result is $H_0 = 73.8 \pm 1.1$ km s^{-1} Mpc^{-1}, which is in 5.3σ tension with *Planck* [141] and has a smaller uncertainty than H0LiCOW lensing alone. As might be expected, the result from the addition of late universe (SNIa) data agrees with the SH0Es 2020 value; and the addition of early universe (BAO) data results in values in agreement with *Planck*. Using weak lensing and BBN to calibrate the sound horizon measured by BAO, [61] finds $H_0 = 67.74 \pm 0.9\,\mathrm{km\,s^{-1}\,Mpc^{-1}}$. Using an inverse distance ladder with lensing and SNIa distance measurements, [135] consistently find $H_0 = 73 - 74$ regardless of the cosmological model used.

A main source of uncertainty in time-delay cosmography is the mass-sheet transform (MST), a mathematical degeneracy that is the addition of a uniform mass sheet which adjusts the absolute time-delay while not changing the lensing observables [121], [19]. This results in the rescaling of the inferred H_0. The MST can be broken by stellar kinematics, which is the approach taken by TDCOSMO. It can also be broken by making assumptions about the mass-density profile of the lens. This is the strategy adopted by H0LiCOW and STRIDES, where the mass density profiles of the lenses are described by either stars, or a power-law with standard dark matter halos. All other mass along the line of sight between the observer and the source besides the mass of the lens explicitly included in the lens model also contribute to the gravitational potential ψ that light rays traverse. They cause additional focussing and defocussing of light rays, which affects the observed time delays. If the effects are small, they can be approximated using an external convergence term (the lensing convergence is defined by (2.22)) in the lens plane, κ_{ext}, defined by [141] with

$$D_{\Delta t} = \frac{D_{\Delta t}^{\mathrm{model}}}{1 - \kappa_{\mathrm{ext}}} \quad , \tag{2.40}$$

where $D_{\Delta t}$ is the true time delay distance (2.35) and $D_{\Delta t}^{\mathrm{model}}$ is the time delay distance inferred from the lens model and the measured time delays. If lenses are randomly distributed, the average of κ_{ext} over a large enough sample should be 0. However, lens galaxies tend to be located in overdense environments which means κ_{ext} will not average out, resulting in a bias on $D_{\Delta t}$ which needs to be corrected for. The external convergence term κ_{ext} cannot be constrained from a lens model and must be estimated using other methods. The effect of the MST can be alleviated by estimating the mass distribution along the line of sight and assuming the physical mass of the lens approaches 0 at a large radius. Furthermore, if the integrated contribution of the line of sight structures approximates a uniform mass-sheet, the bias on H_0 is corrected for by κ_{ext} [85]. But, a realistic line of sight consists of many galaxies at different redshifts, and κ_{ext} over estimates the bias. The authors of [85] recommend that multiple lens planes be included in lens modelling to account for this.

When Refsdal [113] first proposed the use of gravitational lenses to determine H_0 in 1964, it was with supernovae as the source. However, lensed supernovae with multiple resolved images are extremely rare - only three have been observed so far: SN Refsdal, LSN Ia iPTF16geu, and AT2016jka,

only one of which is confirmed to be Type Ia [73]. Therefore lensed quasars are used instead due to their abundance, as well as their brightness and variability which allow for observations at greater distances than supernovae would [141]. These greater distances mean that it can no longer be assumed that z is small, and the results depend on the choice of cosmological model. This allows models to be tested. Quasars or 'quasi-stellar objects' (QSO) are very active galactic centres which are bright enough to be observed at redshifts of up to to $z \sim 7$ [47]. Astronomers believe that quasars are created by the accretion of gas on to massive black holes, typically $10^9\, M_\odot$ [128]. Double or multiple images of distant quasars were the first astronomical gravitationally lensed phenomena observed (besides solar light bending) [50]: QSO 0957+561 (known as the Twin Quasar), at redshift $z = 1.41$, discovered in 1979, was the first observed gravitationally lensed object, and more than 10^4 quasars have been observed since [107]. The advantages of strongly lensed SNIa over quasars is discussed in [73]. Supernovae fade away over time, and thus allow for measurements of the stellar kinematics of the lens galaxy and the surface brightness distribution of the lens galaxy. These break model degeneracies such as the mass-sheet transformation. An upcoming survey, the Rubin Observatory Legacy Survey of Space and Time [1], expects to find $\sim 10^3$ lensed supernovae, of which 10-25 are expected to be Type Ia and yield accurate time delay measurements. In anticipation of this, [73] present a machine learning approach to measure time delays in strongly lensed SNIa. Other lensed sources that could in the future be used to measure H_0 are those that emit both gravitational waves and electromagnetic radiation [34], [69]. The rate of lensing of gravitational waves is expected to be slow, but [34] find that, in ΛCDM, even with only one single gravitational waves lensing event (combined with a *Planck* Ω_m prior), the uncertainty of the H_0 measurement will be comparable or better to current independent probes. A significant time delay could be expected from a supermassive binary black hole emitting electromagnetic radiation and gravitational waves with very small frequencies of $\sim 10^{-8}$ Hz, lensed by a galaxy of mass $M_{\rm lens} \sim 10^{11} M_\odot$ [34]. The probability to observe such an event is of order $10^{-3} - 10^{-4}$ [34], and could possibly be detected by future Japanese space-based interferometers DECIGO and B-DECIGO [69].

The aim of the lensing collaborations, as with all independent measurements, is to achieve a 1% or better precision determination of the Hubble constant for comparison with the SH0Es and *Planck* values. The precision of lensing is limited by sample size, but a future expected sample of forty lenses will deliver 1% precision [141], and no systematic errors have been discovered in the time delay cosmography method to prevent this [139]. A plan to improve the methodology to achieve the desired 1% precision is outlined in [19], in addition to the improvements already made with uncertainties as discussed above. When this precision is achieved, lensing H_0 values will contribute significantly to the Hubble tension conversation.

2.2.3 Gravitational Waves

In 1986 Schutz [126], [127] first described how H_0 could be determined from gravitational wave data and other data gathered from a gravitational wave source. In 2017, the GW170817 neutron star merger event was the first time a source was measured through both its gravitational waves (GW)

and electromagnetic (EM) radiation. With the GW data providing the luminosity distance to and the EM data the redshift of the source, the Hubble constant could be obtained. The result was $H_0 = 70.0^{+12.0}_{-8.0}\,\mathrm{km\,s^{-1}\,Mpc^{-1}}$ [2]. While the error bars are large, this independent measurement is in line with the *Planck* and SH0Es values.

The tensor field $h_{\mu\nu}$ describes gravitational waves and their dynamics in general relativity. The quadrupole formula, which consists only of spatial components because GW are orthogonal to their propagation direction and so the components of $h_{\mu\nu}$ with time indices do not radiate, is [67]

$$h_{jk} = \frac{2G}{c^4}\frac{1}{D_L}\frac{d^2 I_{jk}}{dt^2} \quad , \tag{2.41}$$

where G is the gravitational constant, D_L is the luminosity distance to the source given by equation (1.79), c is the speed of light, and I_{jk} is the mass quadrupole moment of the source given by

$$I_{jk} = \int_{\text{source}} \rho_m \left[r'_j r'_k - \frac{1}{3}(r')^2 \delta_{jk} \right] \quad . \tag{2.42}$$

The quadrupole moment (2.41) shows that the amplitude of the GW is inversely proportional to the luminosity distance to the source. If the variation of the quadrupole mass moment with time is known, a measurement of the GW amplitude results in a value for D_L, and therefore of H_0, without the use of a distance ladder. Schutz [126] showed that the measured data from gravitational waves emitted by neutron star binaries just before coalescence can be used to derive this. He considered a neutron star binary in a circular orbit. The frequency of the orbit f depends on the masses of the stars m_1 and m_2 and their separation. The gravitational waves emitted by the binary take energy from the orbit, which causes the stars to spiral towards each other and reduce their separation. As this occurs, they orbit each other more quickly: the orbital frequency increases on a timescale τ (illustrated in figure 2.7) and is given by

$$\tau = \frac{f}{\dot{f}} \quad , \tag{2.43}$$

where the rate of change is [67]

$$\dot{f} = \frac{96}{5}\left(\frac{G\mathcal{M}}{c^3}\right)^{5/3} f^{11/3} \tag{2.44}$$

(plus correction terms), with $\mathcal{M}$ the chirp mass:

$$\mathcal{M} = \frac{(m_1\, m_2)^{3/5}}{(m_1 + m_2)^{1/5}} \quad . \tag{2.45}$$

The increase in the orbital frequency increases the energy loss of the binary due to the GW, which further decreases the separation and so on. This is referred to as the binary 'chirping': the gravitational waves transition at a high rate, as can be seen in figure 2.7, from being emitted at low frequency to high frequency whilst increasing their amplitude. The rate of change of frequency relies on one parameter only, the chirp mass $\mathcal{M}$. Figure 2.7 shows that a binary with a smaller chirp mass has a larger initial time scale over which the orbital frequency increases as compared to one with a larger chirp mass. But, regardless of the chirp mass, the time scale decreases rapidly and the time it takes for the frequency with which the components orbit each other to increase becomes very small. The larger the chirp mass, the more rapidly the time scale decreases: the merger takes less time to occur for larger chirp masses.

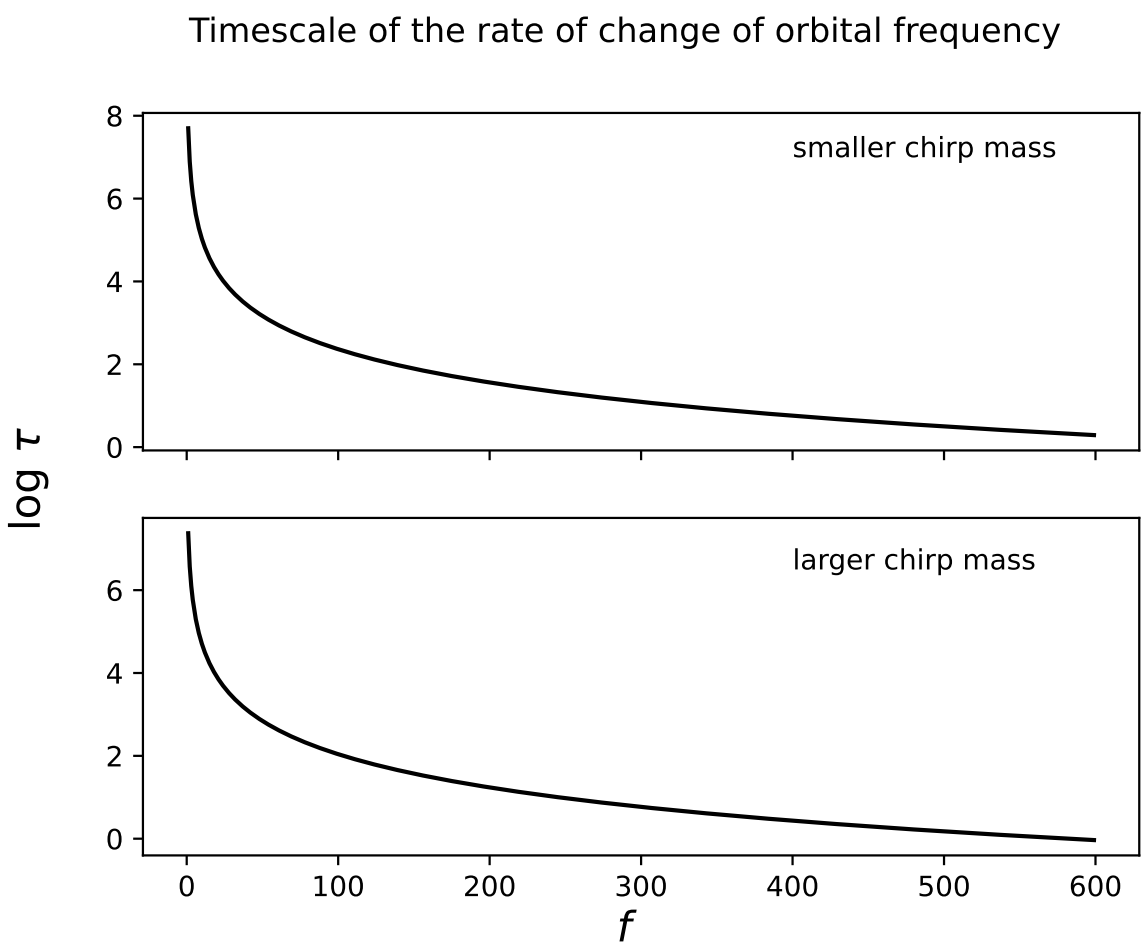

Figure 2.7: The timescale τ over which the frequency f of the orbit of a binary increases when gravitational waves are emitted. The upper plot has a chirp mass of $\mathcal{M} = 0.83\,M_\odot$ (individual masses $0.5\,M_\odot$, $2\,M_\odot$), while the lower plot has $\mathcal{M} = 1.3\,M_\odot$ (individual masses $1.4\,M_\odot$, $1.6\,M_\odot$).

The binary inclination ι is the angle between the line of sight to the source from the detector and the normal to the binary's orbital plane (conventionally, the x-z plane [67]). The binary is viewed head on if $\iota = 0°$ and edge-on if $\iota = 180°$. Gravitational waves have two polarizations given by the amplitudes h_+ and $h_\times$ which, for GW propagating along the z-axis, act along the x and y axes, and along axes rotated 45° from the x and y axes respectively. The equations for the amplitude are

$$h_+ = \frac{2c}{D_L}\left(\frac{G\,\mathcal{M}}{c^3}\right)^{5/3} f^{2/3}\,(1+\cos^2\iota)\,\cos 2\Phi(t) \quad \text{and} \tag{2.46}$$

$$h_\times = \frac{4c}{D_L}\left(\frac{G\,\mathcal{M}}{c^3}\right)^{5/3} f^{2/3}\,\cos\iota\,\sin 2\Phi(t) \quad , \tag{2.47}$$

where $\Phi(t)$ is the accumulated orbital phase which is obtained by integrating f over the total time the measurement occurred [67].

When gravitational waves are measured, the wave form is matched to a model template. In this way, the frequency f and its rate of change $\dot{f}$ are obtained and the chirp mass $\mathcal{M}$ is determined through equation (2.44). If more than one polarization of the GW is measured (i.e. from different detectors in different places), a ratio of their amplitudes (2.46) and (2.47) determines the inclination

angle ι. Then, substituting $\mathcal{M}$ and ι into (2.46) or (2.47), the luminosity distance to the source D_L can be obtained. In this way, GW act similarly to SNIa standard candles. GW detection is more like hearing than seeing and so GW are called 'standard sirens' [67]. Standard candles and standard sirens are both used to determine D_L with a constant known quantity, which is luminosity for standard candles and the chirp mass for standard sirens. The advantage of gravitational waves is that they are understood from first principles whereas Type Ia supernovae are not [67]. If the gravitational wave event has an electromagnetic counterpart that is observed, a measurement of its or its host galaxy's spectrum results in the redshift z of the event. The recession velocity of the galaxy is then used in Hubble's law (1.22) to obtain H_0.

In 2017, a gravitational wave signal from a neutron star binary merger was detected and named GW170817, and the results presented in [2]. The location of its source was derived using three GW detectors: LIGO Livingston, LIGO Hanford and Virgo. A few seconds after the signal was detected, a gamma ray burst was observed in a region consistent with the derived location of the GW source. The galaxy NGC 4993 was observed optically in a similar region and it is assumed that it is the host galaxy, and the location of the GW source on the sky is fixed to its location. The recession velocity v is estimated at the position of NGC 4993 and corrected for local peculiar velocities which come from the random relative motions of nearby galaxies; and H_0 is then obtained using Hubble's law (1.22) as $H_0 = 70.0^{+12.0}_{-8.0}\,\mathrm{km\,s^{-1}\,Mpc^{-1}}$. An improvement in radio signals [68] resulted in a final value of $H_0 = 68.9^{+4.7}_{-4.6}\,\mathrm{km\,s^{-1}\,Mpc^{-1}}$ from GW170817, consistent with both *Planck* and local values due to the large errors. Discussions on the reduction of systematics in GW standard siren measurements with regards to peculiar velocities appear in [64] and [94].

H_0 has also been measured from binary black hole mergers observed by LIGO and Virgo. The luminosity distance from binary black hole merger GW170814 and redshift information from the DES galaxy catalogue produced $H_0 = 75^{+40}_{-32}\,\mathrm{km\,s^{-1}\,Mpc^{-1}}$ [133]. H_0 has been estimated from binary black hole merger GW190521 with similarly large uncertainties in [58] and [93]. A combination of the three events GW170814, GW170817 and GW190814 resulted in $H_0 = 72.0^{+12.0}_{-8.2}\,\mathrm{km\,s^{-1}\,Mpc^{-1}}$ [100].

At present, the precision of the GW determination of H_0 means it can neither confirm not deny the existence of the Hubble tension. The expected increase in the event rate and combinations of sirens should improve the constraint on H_0 from GW events. It has been calculated that 20 - 30 observations of GW events will yield H_0 to 2% precision [29], which will make it comparable with SH0Es and *Planck* and able to contribute to the study of the Hubble tension. KAGRA and LIGO-India are planned detectors that will join Virgo and the current LIGO detectors. Future ground-based detectors the Cosmic Explorer and Einstein telescope will be able to measure practically all neutron star mergers in the universe. The planned space-borne LISA will also be able to detect more GW events.

Chapter 3

Solutions

The reduction in the uncertainties and increase in precision for both the CMB and local values of the Hubble constant H_0, as discussed in chapter 2, suggests that the tension between them is likely not due to errors in measurements but rather either an error in or an exclusion from our current cosmological model. The inference of H_0 from the CMB depends on the entire expansion history and so modifications to increase its value are to the cosmological model: an introduction of some kind of new physics to expand ΛCDM may relieve the tension. The early universe H_0 relies on angular scales, such as θ_* as shown in equation (2.7). The angular scale depends on equation (2.2), the ratio of the sound horizon r_s to the angular diameter distance $D_A(z_*)$, at z_* the redshift of recombination. For the angular scale to remain fixed while the H_0 value is increased, r_s and $D_A(z_*)$ must both decrease. For the early universe H_0 value to be reconciled with the late universe value, the CMB inferred sound horizon must be lowered by $\sim 7\%$ [139]. As introduced in Section 2.1, both the CMB and BAO values of H_0 rely on the value of the sound horizon r_s after decoupling. For the BAO H_0 value to agree with the low H_0 value inferred from the CMB, the BAO must constrain a large r_s value; however for it to agree with the SHOEs high H_0 value, it must constrain a low r_s value. This is called the 'sound horizon problem' [43]. For there to be agreement between these three data sets (BAO, CMB and SH0Es), the CMB, assuming a specific model, needs to produce a larger H_0 value and lower r_s value [43]. Any new physics or models proposing to do this must ensure that the structure of the CMB temperature and polarization spectrums, as well as the consistency between Big Bang Nucleosynthesis (BBN) and the observed abundance of light elements, are preserved. They must be at least as good as ΛCDM at describing other cosmological observations. Models containing new physics should only make changes prior to recombination because any changes to any other period will result in a worse fit to the CMB - that is, any change to the physical densities must be performed mostly through H_0 and the density parameters themselves [139]. Some proposed solutions to the Hubble tension could create new tensions between the CMB and BAO data [43], which must be guarded against. This chapter will provide an overview of the many schemes that have been proposed as solutions to the Hubble tension. It is not intended to be exhaustive. Comprehensive reviews of proposed solutions to the H_0 tension appear in [39], [81] (which provides guidance on model building), [43] and [125]. The focus in this chapter will be on late time solutions and why they do not seem viable, and on early dark energy.

The first question to be considered is: what qualifies a theory or model as a potential solution? What does it need to satisfy? It is necessary for solutions to reproduce standard cosmological results. For example, models whose early universe is different from ΛCDM must be in good agreement with the CMB. In [14], a list of seven assumptions has been compiled, of which it is proposed at least one needs to be broken for a model or theory to possibly alleviate the Hubble tension. These assumptions are listed below.

1. The laws of General Relativity and Einstein's Field Equations (EFE) in equation (1.80) are a good approximation of the physics of the universe on cosmological scales.

2. The universe is spatially isotropic and homogeneous at large scales. Then, the Friedmann–Lemaître–Robertson–Walker (FLRW) metric (1.1) applies.

3. The universe has no significant spatial curvature: that is, $K = 0$ and the FLRW metric (1.1) reduces to
$$ds^2 = -dt^2 + a(t)^2 \left[dx^2 + dy^2 + dz^2\right] \quad ; \tag{3.1}$$
and the Friedmann equation (1.2) reduces to
$$H(t) = \sqrt{\frac{8\,\pi\,G}{3}\,\rho(z)} \quad . \tag{3.2}$$

4. The relationship between the scale factor and redshift is:
$$a(t) = \frac{1}{1+z}\,. \tag{3.3}$$
This means that z can be used as a time variable. The angular diameter distance (1.78) can be re-written using (3.2) as
$$D_A = \int_0^{z_*} \frac{dz'}{H(z')} \tag{3.4}$$
$$D_A = \sqrt{\frac{3}{8\,\pi\,G}} \int_0^{z_*} \frac{dz'}{\sqrt{\rho(z')}}\,, \tag{3.5}$$
where z_* is the redshift of recombination.

5. The variation with redshift of a model specific density ρ_x is constrained by
$$\frac{\partial \rho_x}{\partial z} \geq 0 \quad \text{for} \quad z < z_* \quad \text{with} \tag{3.6}$$
$$\rho(z) = \rho_x(z) + \rho_m(z_*) \left(\frac{1+z}{1+z_*}\right)^3 \quad . \tag{3.7}$$
The total matter density $\rho(z)$ is the sum of model specific effects, given by ρ_x, and the dilution due to expansion of $\rho_m(z_*)$, the matter density at decoupling. The change in ρ_x after decoupling is shown in equation (3.6): after decoupling there is no net matter creation due to ρ_x and no decay from ρ_m contributing to ρ_x. Using the total matter density given in (3.7) in equation (3.5), and applying assumption 5 as given in (3.6), results in the following constraint:
$$D_A \leq \sqrt{\frac{3}{8\pi G}} \int_0^{z_*} \frac{dz'}{\sqrt{\rho_m(z_*)\left(\frac{1+z'}{1+z_*}\right)^3 + \rho_x(0)}} \quad . \tag{3.8}$$

The remaining two assumptions are observational not theoretical.

6. There are no significant unaccounted for systematic or model-induced errors in the *Planck* analysis of the CMB.

7. There are no significant unaccounted for systematic or model-induced errors in the distance measurements of late-time measurements, especially for measured redshifts and absolute luminosities.

From equation (3.2), $\rho(z = 0)$ and H_0 are directly related. Then, under the seven above assumptions, the following holds: for a given H_0 value, there is a maximal value of D_A in the analysis of the CMB under the assumption of ΛCDM. This means that any other model will have a lower D_A value. However, D_A is fixed by observations, so any model satisfying all seven assumptions would need a lower value of H_0 than the CMB value in order for equation (3.8) to hold. But late time observations measure an H_0 that is larger than the *Planck* value. Thus, for a model to obtain a larger value of H_0 from the CMB, it must break at least one of the seven assumptions.

These assumptions provide a framework in which a proposed model can immediately be dismissed as a possibility if it does not break any of the assumptions. A model that does break one of the assumptions can then be examined further. The assumptions also provide a starting point from which a new model that may resolve the tension can be developed. For example, as shown below, there do not appear to be any proposed theories which break assumption 4 and a potential solution could possibly start from there. Solutions can be categorised according to which assumptions they break.

The wide variety of independent late universe measurements that are in agreement makes it unlikely that assumption 7 is untrue, i.e. that there are significant systematics affecting late time distance measurements. However, effects that act in a similar way to systematics in the late universe could decrease the angular diameter distance and cause late measurements to overestimate the value of H_0. Once the overestimation is known and compensated for, a lower value of H_0 can be obtained. Examples of this include photon brightening [81], a local matter void [45] and screened fifth forces [38]. It is also unlikely that there are significant systematics affecting early observations such that breaking assumption 6 will resolve the Hubble tension. However, the effects of modifying the sound horizon could result in apparent systematics that may provide a solution. The lowered sound horizon decreases D_A, which then results in a larger early universe H_0 value. Examples of proposed solutions where the sound horizon is modified by changing the time of matter-radiation equality include neutrino mass mechanisms [51] and additional light particles [143]. The sound horizon can also be changed by dark energy models that change the evolution of the universe just after matter-radiation equality such as early dark energy [111], which is discussed further in section 3.2. Modifying the mechanism of recombination by producing a different temperature of recombination or a more stretched recombination would change the interpretation of the CMB resulting in a different D_A value. This mimics the effect of systematics, and would produce a larger early universe H_0 value [14].

Some proposed solutions modify the relationship between D_A and the elements of $H(z)$. Examples of these that change this relationship by breaking assumption 1 are alternative gravitational theories

that modify GR such as those that appear in [140], [78], [99], and [98], or those that go beyond GR, such as üΛCDM, based on über-gravity [80]. These types of models have also been used to explain different phases of the universe such as acceleration at late times. Other proposed solutions that deviate from perfect spatial flatness or isotropy such that evolution is affected break assumptions 2 and/or 3, for example an 'effective' curvature type contribution from matter dumping [65] and a solution that breaks isotropy that appears in [11]. Another category of proposed solutions is those that break post-recombination assumptions. A model which contains decaying dark matter does not obey (3.6) and breaks assumption 5. In these kinds of models, dark matter decays to some component that dilutes more slowly. This increases the early universe H_0. Part of dark matter decaying into dark radiation are included in the models proposed in [104], [32] and [62]. In [12], it is shown that cold dark matter that decays before recombination cannot resolve the tension, and so in [138] and [20] warm decaying dark matter is introduced, with constraints provided in [27]. Other kinds of exotic dark energy fall into this category, such as late dark energy [15] (this is disfavoured according to [96]), time varying dark energy (vacuum phase transitions) [40], dark energy with phantom crossing [44], as well as coupled or interacting dark energy in [60], [42], [101], [102] and [41]. Dark energy with an equation of state w (1.86) that is less than the vacuum energy could cause stronger acceleration and resolve the Hubble tension, however this solution is strongly disfavoured by intermediate redshift measurements [114]. Interacting dark matter and dark energy are models that have also been proposed in [137] and [144], as well as one where the transfer of energy between dark matter and dark energy changes sign [103]. Interacting dark matter has also been suggested in [70], with self-interacting neutrinos [24]. Other models could break assumption 4 such that the relationship between the scale factor and redshift (3.3) does not hold true. Smaller than expected values for $a(z_*)$ will result in larger z_* values and thus a larger integration range in equation (3.5). This produces a larger Hubble parameter without decreasing the fixed D_A value. The Hubble tension is reduced because a larger early universe H_0 value is obtained. There does not appear to be any current research on this approach [14], however it is difficult to imagine such a scenario where equation (3.3) is not obeyed.

Solutions to the Hubble tension can also be divided into 'early' and 'late' categories. Late time solutions make modifications to the expansion history after recombination to increase the value of the early universe H_0 without altering the sound horizon. These types of solutions, for example wCDM where the dark energy equation of state w is free to vary, could solve the tension between SH0Es and the CMB but they disagree with BAO data [43]. On the other hand, early solutions also raise the value of the early universe H_0 but do alter the sound horizon, decreasing it by increasing the expansion rate $H(z)$ prior to recombination. An increase in the energy density (such as through an early dark energy component) around recombination will increase the expansion rate, as will the introduction of extra radiation. These kinds of solutions can alleviate the tension to below 3σ [43], but cannot fully resolve it: models which only reduce the sound horizon can never fully resolve the tension because they do not agree with other data sets [75]. A model which increases H_0 by decreasing the matter density will be in tension with BAO data because the slopes of the $r_s - H_0$ degeneracy lines for BAO and CMB data are completely different: the CMB and SH0Es cannot be reconciled through a reduction in the sound horizon without disagreeing with BAO data [75]. If instead the matter density is increased to raise the value of H_0, the model will be in tension with weak lensing data [75]. Furthermore, the introduction

of new particles such as additional neutrinos would create new conflicts with the CMB [114]; and the addition of an extra new exotic energy or an increase in the density of a known energy would affect the gravitational potentials such that the CMB anisotropy spectra are modified. Thus, a viable model needs to do more than just modify the sound horizon. These examples again reiterate that proposed solutions to the Hubble tension need to agree with all current data sets in order to be successful.

One of the early solutions mentioned above is a category of models that introduce extra dark radiation around recombination. This is quantified by the number of relativistic degrees of freedom $N_{\rm eff}$, also known as the effective number of neutrinos. The radiation density is given by

$$\rho_r = \rho_\gamma \left[1 + \left(\frac{4}{11}\right)^{4/3} N_{\rm eff}\right] \quad , \tag{3.9}$$

where ρ_γ is the photon density. The ratio of the background temperature of neutrinos T_ν to that of photons T_γ is given, under the approximation of instantaneous photon decoupling [43], by

$$\frac{T_\nu}{T_\gamma} \equiv \left(\frac{4}{11}\right)^{4/3} \quad . \tag{3.10}$$

The standard model has three active massless neutrino families. Introducing additional relativistic degrees of freedom to this will produce more radiation. The effect of this will be to smear and shift the acoustic peaks in the damping tail of the CMB temperature power spectrum, as well as to delay matter-radiation equality [43]. There is a strong degeneracy between H_0 and $N_{\rm eff}$: additional radiation at recombination could result in a larger early H_0 value. A model with additional $N_{\rm eff}$ used to analyse *Planck* 2018 will produce an H_0 value that is in 3.6σ tension with the SH0Es 2020 result [43]. This is not much of an improvement on the current 4.2σ tension; and, as mentioned above, this type of solution will create new conflicts with the CMB. This category of models with additional dark energy at recombination include sterile neutrinos [59], self-interacting neutrinos and various kinds of decaying dark matter as mentioned above. If extra free streaming neutrinos are introduced in order to alleviate the Hubble tension, the fit to the high-ℓ CMB angular power spectrum is degraded. However, the fit can be improved if the neutrinos are instead self-interacting: not free streaming but instead behaving like tightly coupled radiation (see [24], [21], [22], [63] and [87]). The delayed onset of neutrino streaming until close to matter radiation epoch requires strong self-interacting neutrinos and produces $N_{\rm eff} = 4.02 \pm 0.29$ [83]. The introduction of self-interacting neutrinos and additional neutrino species could result in a larger CMB-inferred H_0 value and reduce the tension. Note, however, that the very strong coupling this requires is difficult to achieve while adhering to other constraints on neutrino physics [139].

There are other models that have been proposed to resolve the Hubble tension that introduce extra non-gravitational interactions between components of the universe besides self-interacting neutrinos. Some, such as interacting dark matter and models where dark matter and dark energy interact have already been referenced. The latter has also been studied as a way to solve the cosmological constant problem, the cosmic coincidence problem and to explain phantom dark energy [43]. The basic framework of interacting dark energy, as described in [43], is that the coupling of dark matter and dark

energy require the continuity equation (1.94) to be rewritten for dark matter (DM) and dark energy (DE) as

$$\rho'_{\rm DM} + 3\,\mathcal{H}\,\rho_{\rm DM} = a\,\mathcal{Q} \quad , \tag{3.11}$$

$$\rho'_{\rm DE} + 3\,\mathcal{H}\,(1+w_{\rm DE})\,\rho_{\rm DE} = -\,a\,\mathcal{Q} \quad , \tag{3.12}$$

where the prime denotes the derivative with respect to the conformal time η, $\mathcal{Q}$ is the interaction rate which characterizes the energy and/or momentum flow between dark energy and dark matter, and $\mathcal{H}$ is the conformal Hubble rate, given by

$$\mathcal{H} \equiv \frac{a'}{a} \quad . \tag{3.13}$$

In standard ΛCDM, dark matter does not collide with anything. Interacting dark matter is an extension of this, where dark matter interacts with other components of the universe.

An underdense local universe seems to have been ruled out as a solution to the Hubble tension [114]. The extreme underdensity required for a void like the one proposed in [142] is very unlikely to exist in the large scale structure (LSS) fluctuations of the ΛCDM universe [43]; and the SNIa luminosity distance-redshift relation (1.76) is in $4-5\sigma$ disagreement with the kind of void that could explain the tension [79]. Furthermore, there is a lack of evidence for the existence of such an underdensity, and the probability of such an occurrence exceeds 10σ [142]. A similar type of solution is the Swiss cheese model [53], [52], which is inhomogeneous on small scales but isotropic and homogeneous on large scales. It has been used to reconcile the value of $\Omega_{m,0}$ obtained by direct measurement with the inferred value from the *Planck* results in 2013, but did not do much to resolve the Hubble tension.

The 'Swiss cheese' models were proposed to address the 'Ricci-Weyl' problem. The problem is that observations of the CMB and supernovae have different sizes of light beams: ~ 5 arc min compared to $\sim 10^{-7}$ arc sec. These two observations probe the universe at very different scales, so inhomogeneity will affect them differently via gravitational lensing. The Riemann tensor $R_{\mu\nu\alpha\beta}$ can be decomposed into the Ricci $R_{\mu\nu}$ and Weyl $C_{\mu\nu\alpha\beta}$ components. The evolution of the separation vector k^μ is governed by the geodesic deviation equation:

$$u^\alpha\,u^\beta\,\nabla_\alpha\,\nabla_\beta = R^\mu_{\nu\alpha\beta}\,u^\nu\,u^\alpha\,k^\beta \quad . \tag{3.14}$$

The Sachs equation is obtained by projecting the geodesic deviation equation (3.14) on to the Sachs basis $(s^\mu_A)_{A\in 1,2}$ and is:

$$\frac{d^2 k_A}{dv^2} = \mathcal{R}_{AB}\,k^B \quad , \tag{3.15}$$

where

$$\mathcal{R}_{AB} = R_{\mu\nu\alpha\beta}\,k^\nu\,k^\alpha\,s^\mu_A\,s^\beta_B \tag{3.16}$$

is the optical tidal matrix and can be decomposed into the Ricci and Weyl terms which are given by

$$\mathcal{R}_{\mathcal{AB}} = \begin{pmatrix} \Phi_{00} & 0 \\ 0 & \Phi_{00} \end{pmatrix} + \begin{pmatrix} -\mathrm{Re}\ \Psi_0 & \mathrm{Im}\ \Psi_0 \\ \mathrm{Im}\ \Psi_0 & \mathrm{Re}\ \Psi_0 \end{pmatrix} \quad . \tag{3.17}$$

The first term of (3.17) is the Ricci term and the second term is the Weyl term, with

$$\Phi_{00} \equiv -\frac{1}{2}R_{\mu\nu}\,k^\mu\,k^\nu \text{and} \tag{3.18}$$

$$\Psi_0 \equiv -\frac{1}{2}C_{\mu\nu\alpha\beta}\,\sigma^\mu\,k^\nu\,k^\alpha\,\sigma^\beta \quad \text{with} \quad \sigma^\mu \equiv s^\mu_1 - i s^\mu_2 \quad . \tag{3.19}$$

The Riemann curvature experienced by a light beam is dominated by the Weyl term in a universe with discrete matter distribution, and by the Ricci term in a universe smoothed on large scales. The Ricci term focusses light beams, and acts on large beams such as CMB observations; whereas the Weyl term shears and rotates light beams, acting on narrow beams such as supernova observations. Light beams behaving differently based on whether they experience Ricci- or Weyl-dominated lensing is called the Ricci-Weyl problem. Swiss cheese models proposed to address the problem consist of a universe which is homogeneous on large scales but very inhomogeneous on small scales. In [52] and [53], the Swiss cheese universe is made of the FLRW universe with multiple holes or spherical voids. The geometry inside the holes is governed by the Kottler metric, which is an exact solution of the Einstein Field Equations (1.80) and is an extension of the Schwarzschild metric with $\Lambda \neq 0$:

$$ds^2 = -A(r)\,dt^2 + A^{-1}(r)\,dr^2 + r^2\,d\Omega^2 \tag{3.20}$$

with

$$A(r) \equiv 1 - \frac{r_S}{r} - \frac{\Lambda r^2}{3} \quad , \tag{3.21}$$

where r_S is the Schwarzschild radius. Inside the holes are clumps of matter which model systems such as clusters of galaxies. The introduction of holes with a Kottler geometry have a negligible effect on redshift but a significant effect on the luminosity distance $D_L(z)$: reduced Ricci focussing increases $D_L(z)$. This could result in a smaller direct measurement of H_0, reducing the Hubble tension. Compared to a homogeneous universe, sources are demagnified: the effect increases with redshift, and the more lumpy the universe, the greater the effect. In the Swiss cheese models discussed here, light propagates only through underdense regions. This is different from Swiss cheese models where the holes exist in a Lemaître-Tolman-Bondi universe, where light propagates through both and underdense regions, and is demagnified only if light passes through underdense regions. Ultimately, the Swiss cheese models do not seem to resolve the Hubble tension.

The effectiveness of various solutions at resolving the Hubble tension can now be considered, guided by analysis in [43]. Models that are based on introductions of new kinds of dark energy, such as dynamical or interacting dark energy, appear to be better at resolving the tension than those based on early dark energy or neutrino-dark matter interactions when considering only their agreement with the *Planck* data set. However, this classification ignores the physics behind the model, any tension with other observations such as BAO and the effect of correlations between data sets. Models that appear successful at resolving the Hubble tension often disagree with other data sets such as BAO and the Pantheon supernova catalogue: and often the tension is alleviated because of a larger error bar and not necessarily by actually changing the H_0 value. Considering both *Planck* and external data, [43] find that no one solution appears superior to any others at resolving the tension. In comparison, solutions that introduce additional components in order to increase the expansion rate $H(z)$ in the decade prior to recombination, including early dark energy and extra relativistic species, are found by [81] to be most likely. Again, however, these solutions do not actually increase the early H_0 value: the tension is reduced because of the increase in uncertainty in the values.

This chapter continues with a discussion of the problems facing late time solutions following analysis in [49] in section 3.1, and then a comprehensive study of Early Dark Energy in section 3.2.

3.1 Late universe solutions

Late universe solutions are those that change the physics in the post-recombination universe, resulting in a lower H_0 value measured at late times. However, these solutions often overlook the fact that the distance ladder does not directly measure H_0: instead, it measures luminosity. The changes made by models attempting this approach by rapidly increasing $H(z)$ close to $z = 0$ do not seem to take this into account, as discussed in [36] and [49], which results in a suggestion of a resolution to the Hubble tension when there is none. Luminosity depends on the the integrated expansion history, not just on H_0. Simply increasing $H(z)$ as $z \to 0$ will not result in a redshift-distance relation that is compatible with the one that is inferred from the distance ladder [36].

The 'SNIa luminosity problem' is a particular interpretation of the Hubble tension [36]. It suggests that the luminosity inferred from the distance ladder is too dim. A brighter luminosity from SNIa that are further away would result in a lower late universe H_0 value. A possible cause of this is that in the underlying geometric distance measurements underpinning the distance ladder there are significant errors [48], [49].

Figure 3.1 shows the Hubble parameter at low redshift, giving the best fit of ΛCDM from *Planck* data in one curve, and the Hubble rate produced with parameters that are chosen to give the SH0Es 2019 H_0 value whilst maintaining the fit to BAO constraints at $z > 0.3$ in the other curve. The latter curve could be interpreted as a variation in the equation of state of dark energy requiring $w < -1$ at low z, or as a result of the transference between dark matter and dark energy. These have been proposed as solutions to the Hubble tension and change the late time dynamics to obtain a lower H_0 value like in the lower curve. Analysis performed using the inverse distance ladder (see chapter 1) in [49] indicates that changes like these to physics in the late universe cannot resolve the Hubble tension. Proposed solutions that do so are not viable because the distance ladder does not measure H_0 directly: it directly measures luminosities, or equivalently magnitudes, as discussed in section 2.2.1. A SH0Es H_0 prior is imposed in these models whether or not they are consistent with the magnitude-redshift relation of SNIa, which they need to be. The SH0Es distance ladder in fact measures M_B, the absolute peak magnitude of SNIa. M_B is converted to an H_0 value via the magnitude-redshift relation: magnitude and luminosity distance are related through equation (2.15). If changes to late time physics are explored and the results compared with SH0Es results, [49] recommend that M_B should be used as a parameter instead of H_0 (see also [25]); and that when SH0Es data is combined with other data, a SH0Es prior should be imposed on M_B not H_0. A late time solution that results in M_B agreeing with SH0Es measurements may resolve the tension. If a SHOEs H_0 prior is imposed on a data set that excludes the Pantheon supernovae sample, evidence for a phantom-like dark energy could be inferred. However, the Pantheon sample is an essential element in the SH0Es distance ladder, and such dark energy is strongly disfavoured by the Pantheon magnitude-redshift relation [49]. Furthermore, post-recombination solutions could introduce new CMB anisotropies at late times which may confuse the inference of cosmological parameters from the CMB [81].

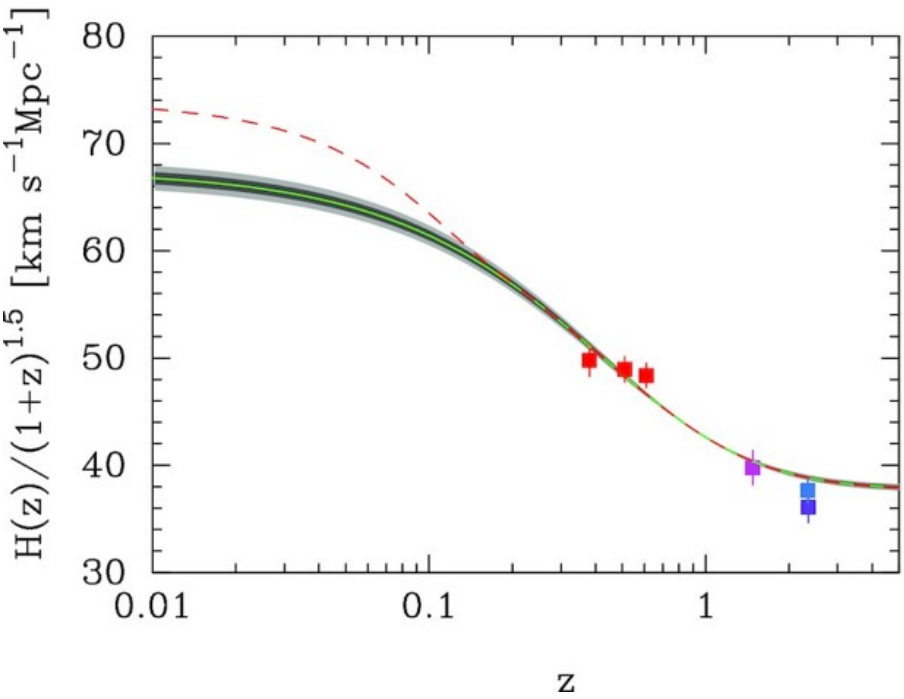

Figure 3.1: The Hubble rate at low redshift. The points are BAO constraints, and the solid line gives the best fit of ΛCDM from *Planck* data, while the dashed curve is produced with parameters chosen to match the SH0Es 2019 H_0 value whilst fitting to the BAO constraints at $z > 0.3$. From [49].

Theoretical explanations for the tension that focus on new physics in the decade of expansion preceding recombination instead seem more plausible, and one example of this is early dark energy, which is discussed in the next section.

3.2 Early Dark Energy

The introduction of new physics into the early universe seems more likely to be successful at resolving the Hubble tension than into the late universe. An example of this is to introduce a new source of energy density that increases the Hubble parameter $H(z)$ just prior to recombination. As can be seen in equation (2.3), a smaller sound horizon will result in an increased early universe H_0 value. Early dark energy (EDE) is a popular new source of energy density. The aim of EDE is to obtain an H_0 value which is larger than the one inferred when fitting ΛCDM to the CMB, while maintaining the overall fit to the CMB. EDE is constructed such that the energy density of the EDE component is only relevant between matter radiation equality and recombination.

As introduced in chapter 2, the angular scale θ_* is an observable, and so the ratio between the sound horizon r_s and the angular distance D_A, as given in equation (2.2), must remain constant when new physics is introduced. For the value of H_0 to be increased by the $\approx 10\%$ required to eliminate the tension [66], and for θ_* to be kept fixed, there needs to be a corresponding $\approx 10\%$ decrease in r_s. This requires a change in the expansion history prior to recombination. For this to occur, while also preserving the rest of CMB physics, an extra contribution to the total energy density is required for

a brief period just prior to recombination which would be $\approx 10\%$ of the total [66]. The new energy density would need to rapidly decay after the required decrease in r_s is obtained. This new energy is referred to as early dark energy. It behaves like dark energy at early times, and rapidly decays and becomes subdominant after a critical redshift z_c. EDE changes both the shape and amplitude of the Hubble parameter [81].

The new source of energy density introduced by EDE models are ultralight scalar fields ϕ. They are much lighter than ultra-light axions and fuzzy dark matter [66]. Various different models of EDE have been proposed. These include unstable dark energy [10]; New Early Dark Energy [97]; acoustic dark energy [86]; EDE from massive neutrinos [122]; and monomial potentials [9] - the latter was found in [131] to be unfavourable compared to other models. A model presented in [111] has a scalar field that rolls slowly down its potential which is linear at early times and approaches 0 at late times. A similar model is explored in [66]: ϕ is displaced from its minimum at early times, and once $H(z)$ drops below the mass of the field, ϕ rolls downs its potential and starts to oscillate around the minimum. If the potential around the minimum is steeper than a quadratic, the EDE field is dominant in the early universe only. The oscillating EDE scalar field with potential $V(\phi) \propto \phi^{2n}$ that appears in [111] (and is also discussed in [110] and [131]) has been chosen as an illustrative model and will be expanded on further in this section. This model finds a higher value for the CMB-inferred H_0 that alleviates the Hubble tension whilst preserving the fit to relevant observations. The authors of [111] estimate that for the 2018 SH0Es value, the tension with *Planck* can be reduced from 3.6σ to less than 1.6σ by the introduction of EDE. The specific details of the model do not affect how well the tension is resolved - as long as at $z \simeq 5000$, approximately 7% of the total energy density comes from EDE, and that afterwards the EDE decays like radiation or faster. However, $n = 3$ is favoured because the tension is then further reduced to 1.2σ.

Oscillating scalar fields are presented in [136]. A scalar field ϕ with a potential $V(\phi)$ has a Lagrangian

$$\mathcal{L} = -\frac{1}{2}\,\partial_\mu\phi\,\partial^\mu\phi - V(\phi) \quad . \tag{3.22}$$

The stress-energy tensor of the scalar field is

$$T^{\mu\nu} = \partial^\mu\phi\,\partial^\nu\phi + \mathcal{L}g^{\mu\nu} \quad . \tag{3.23}$$

The equations of motion for the scalar field are obtained by varying its action or from the conservation of the stress-energy tensor. In a homogeneous and isotropic FLRW cosmology the scalar field is necessarily homogeneous and its equation of motion is the Klein-Gordon equation

$$\ddot{\phi} + 3H\,\dot{\phi} + \frac{dV}{d\phi} = 0 \quad , \tag{3.24}$$

where the dot denotes the derivative with respect to proper time t. Equation (3.24) can be re-written as follows:

$$\frac{d}{dt}\left(\frac{1}{2}\,\dot{\phi}^2 + V\right) = -3H\,\dot{\phi}^2 \quad . \tag{3.25}$$

The energy density ρ_ϕ and pressure p_ϕ of the scalar field are given by

$$\rho_\phi = \frac{1}{2}\,\dot{\phi}^2 + V(\phi) \quad \text{and} \tag{3.26}$$

$$p_\phi = \frac{1}{2}\,\dot{\phi}^2 - V(\phi) \quad . \tag{3.27}$$

Then, from equation (3.25),

$$\frac{d\rho_\phi}{dt} = -3H\,(\rho_\phi + p_\phi) \quad . \tag{3.28}$$

Furthermore,

$$\frac{d}{dt}\left(\rho_\phi\, a^3\right) = \left(\frac{d\rho_\phi}{dt}\right) a^3 + \rho_\phi\,\frac{da^3}{dt} \tag{3.29}$$

$$= -3H\,(\rho_\phi + p_\phi)\, a^3 + 3\rho_\phi\, a^2\,\dot{a} \tag{3.30}$$

$$= -3H\,(\rho_\phi + p_\phi)\, a^3 + 3\rho_\phi\, a^3\, H \tag{3.31}$$

$$= -3H\, p_\phi\, a^3 \quad , \tag{3.32}$$

and

$$-\,p_\phi\,\frac{da^3}{dt} = -3p_\phi\, a^2\,\dot{a} = -3H\,\rho_\phi\, a^3 \quad . \tag{3.33}$$

Therefore

$$\frac{d}{dt}\left(\rho_\phi\, a^3\right) = -p_\phi\,\frac{d}{dt}\left(a^3\right) \quad . \tag{3.34}$$

Equations (3.25), (3.28) and (3.34) show that the energy density ρ_ϕ of the scalar field decays because of the redshifting away of the kinetic part $\frac{1}{2}\,\dot{\phi}^2$.

The scalar field ϕ oscillates about the minimum of $V(\phi)$. Assume the frequency of the oscillations ω is always much larger than the Hubble rate, such that

$$\omega \simeq \frac{\dot{\phi}}{\phi} \gg H \quad . \tag{3.35}$$

As the scalar field oscillates, the energy density varies slowly with time, decreasing on a time scale characterized by H^{-1}. However, $(\rho_\phi + p_\phi) = \dot{\phi}^2$ varies rapidly on a time scale characterized by $\omega^{-1} \ll H^{-1}$. Introducing w_n, the average of $(\rho_\phi + p_\phi)$ over an oscillation, and w_{np}, which represents the periodic part of $\dot{\phi}^2$, as

$$\dot{\phi}^2 = \rho_\phi + p_\phi = (w_n + w_{np})\,\rho_\phi \quad , \tag{3.36}$$

equation (3.28) can be rewritten and integrated as follows:

$$\frac{d\rho_\phi}{dt} = -3H\,(w_n + w_{np})\,\rho_\phi \tag{3.37}$$

$$\int_{t_0}^{t} \frac{d\rho_\phi}{\rho_\phi} = -3\int_{t_0}^{t} \frac{\dot{a}}{a}\, w_n\, dt - 3\int_{t_0}^{t} H\, w_{np}\, dt \tag{3.38}$$

$$\ln\left(\frac{\rho_\phi}{\rho_{\phi,0}}\right) = -3\int_{t_0}^{t} w_n\,\frac{da}{a} - 3\int_{t_0}^{t} H\, w_{np}\, dt \quad , \tag{3.39}$$

where $\rho_\phi(t_0) = \rho_{\phi,0}$. The periodic nature of w_{np} means that its integral over time is:

$$\int_0^t w_{np}\, dt \lesssim O\left(\omega^{-1}\right) \quad . \tag{3.40}$$

The final term of (3.39) can be integrated by parts, and, using (3.40), the leading term will be of the order $\frac{H}{\omega}$. By assumption (3.35) $\omega \gg H$, so this term is much less than 1 and can be neglected with respect to the first term on the right hand side of (3.39). If w_n is constant, than integrating (3.39) results in:

$$\rho_\phi = \rho_{\phi,0} \left(\frac{a}{a_0}\right)^{-3w_n} \quad , \tag{3.41}$$

where $a(t_0) = a_0$. If the oscillating scalar field energy density ρ_ϕ dominates the total energy density including ρ_Λ, then, in the limit where curvature can be ignored, the Friedmann equation (1.92) can be written

$$\left(\frac{\dot{a}}{a}\right)^2 = 8\pi G\, \rho_{\phi,0} \left(\frac{a}{a_0}\right)^{-3w_n} \quad . \tag{3.42}$$

Solving this for $a(t)$ results in

$$\frac{a^{3w_n/2}}{3w_n/2} = \frac{\sqrt{8\pi G}\, \rho_{\phi,0}}{a_0^{3w_n/2}}\, t \quad . \tag{3.43}$$

This indicates that

$$a(t) \propto t^{2/3w_n} \quad . \tag{3.44}$$

On time scales much smaller than H^{-1}, the scalar field energy density ρ_ϕ is constant - that is, conserved. $\phi_{\max}$ is the amplitude of the oscillations, occurring at $\dot{\phi} = 0$. Then, from (3.26)

$$\rho_\phi = V(\phi_{\max}) \equiv V_{\max} \quad . \tag{3.45}$$

Using (3.36) and (3.26), and recalling that the contribution from w_{np} can be ignored, w_n can be written as

$$w_n = 2\left(1 - \frac{V}{V_{\max}}\right) \quad . \tag{3.46}$$

Averaging $\frac{\dot{\phi}^2}{\rho_\phi}$ over one cycle, w_n is then given by

$$w_n = 2\, \frac{\int_0^{\phi_{\max}} (1 - V/V_{\max})^{1/2}}{\int_0^{\phi_{\max}} (1 - V/V_{\max})^{-1/2}} \quad . \tag{3.47}$$

For a potential with the form

$$V(\phi) \propto \phi^n \quad , \tag{3.48}$$

equation (3.47) can be integrated to obtain

$$w_n = \frac{2n}{n+2} \quad . \tag{3.49}$$

The oscillating scalar field presented in [111], [110] and [131] has a potential

$$V(\phi) = m^2 f^2 \left(1 - \cos\left[\frac{\phi}{f}\right]\right)^n \quad , \tag{3.50}$$

where f is the ultra light axion-like decay constant. The field is flat and acts like a cosmological constant at early times, but when $H(z)$ drops below a certain value at some critical redshift $z_c \gtrsim 3000$, the field begins to oscillate and behave like a fluid. The Friedmann equation (1.92) can be rewritten, in the limit where curvature can be ignored, as

$$H^2 = \frac{8\pi G}{3} \left(\rho_m + \rho_r + \rho_\Lambda + \rho_\phi\right) \tag{3.51}$$

$$H(z) = H_0\, E(z) = H_0 \sqrt{\Omega_m (1+z)^3 + \Omega_r (1+z)^4 + \Omega_\Lambda + \Omega_\phi} \quad , \tag{3.52}$$

where, as in chapter 1, ρ_m, ρ_r and ρ_Λ are the energy densities of matter, radiation and the cosmological constant respectively; and the dimensionless density parameter (1.101) and dimensionless expansion rate $E(z)$ (1.108) are used. Redefining the variables to be dimensionless as in [110] with

$$\Theta = \frac{\phi}{f} \quad , \quad \alpha \equiv \frac{f}{M_{Pl}} \quad , \quad x = H_0\, t \quad \text{and} \quad \mu \equiv \frac{m}{H_0} \quad , \tag{3.53}$$

where $M_{Pl} \equiv (8\pi G)^{1/2}$ is the reduced Planck mass, the scalar field's potential (3.50), equation of motion (3.24) and energy density (3.26) can then be written:

$$V(\Theta) = \mu^2\, \alpha^2\, (1 - \cos\Theta)^n \tag{3.54}$$

$$\Theta'' = -3\, E\, \Theta' - \frac{1}{\alpha^2}\, \frac{dV}{d\Theta} \tag{3.55}$$

$$\Omega_\phi(a) = \frac{1}{3}\left(\frac{1}{2}\, \alpha^2\, \Theta'^2 + V(\Theta)\right) \quad , \tag{3.56}$$

where the prime denotes the derivative with respect to x. The potential of the scalar field during the oscillating phase in the terms of the dimensionless variables (3.53) has the form

$$V(\Theta) \simeq \frac{1}{2^n}\, \mu^2\, \alpha^2\, \Theta^{2n} \quad . \tag{3.57}$$

For $n = 1$, the oscillations are simple harmonic oscillations and their frequency is independent of their amplitude; whereas for $n > 1$, the oscillations are anharmonic with a frequency dependent on their amplitude. Setting $w_{np} = 1$, the energy density (3.41) can be written

$$\rho_\phi = \rho_{\phi,0}\, \left(\frac{a}{a_0}\right)^{-3(1+w_n)} \quad . \tag{3.58}$$

This indicates that the energy density of the scalar field decays as $a^{-3(1+w_n)}$. Solving (3.47) with the potential (3.57), w_n is

$$w_n = \frac{n-1}{n+1} \quad . \tag{3.59}$$

The EDE energy density (3.56), in an effective-fluid approximation [111] (i.e. approximating EDE as an anisotropic fluid which behaves like an ordinary liquid such as water, but whose properties are different in different directions), is given by [110] as

$$\Omega_\phi(a) = \frac{2\,\Omega_\phi(a_c)}{\left(\frac{a}{a_c}\right)^{3(w_n+1)} + 1} \quad . \tag{3.60}$$

The EDE model is parameterized by $f_{\rm EDE}$, the EDE field's maximal fractional contribution to the energy density of the universe, which is defined by [111] as

$$f_{\rm EDE} \equiv \frac{\Omega_\phi(a_c)}{\Omega_{\rm total}} \quad . \tag{3.61}$$

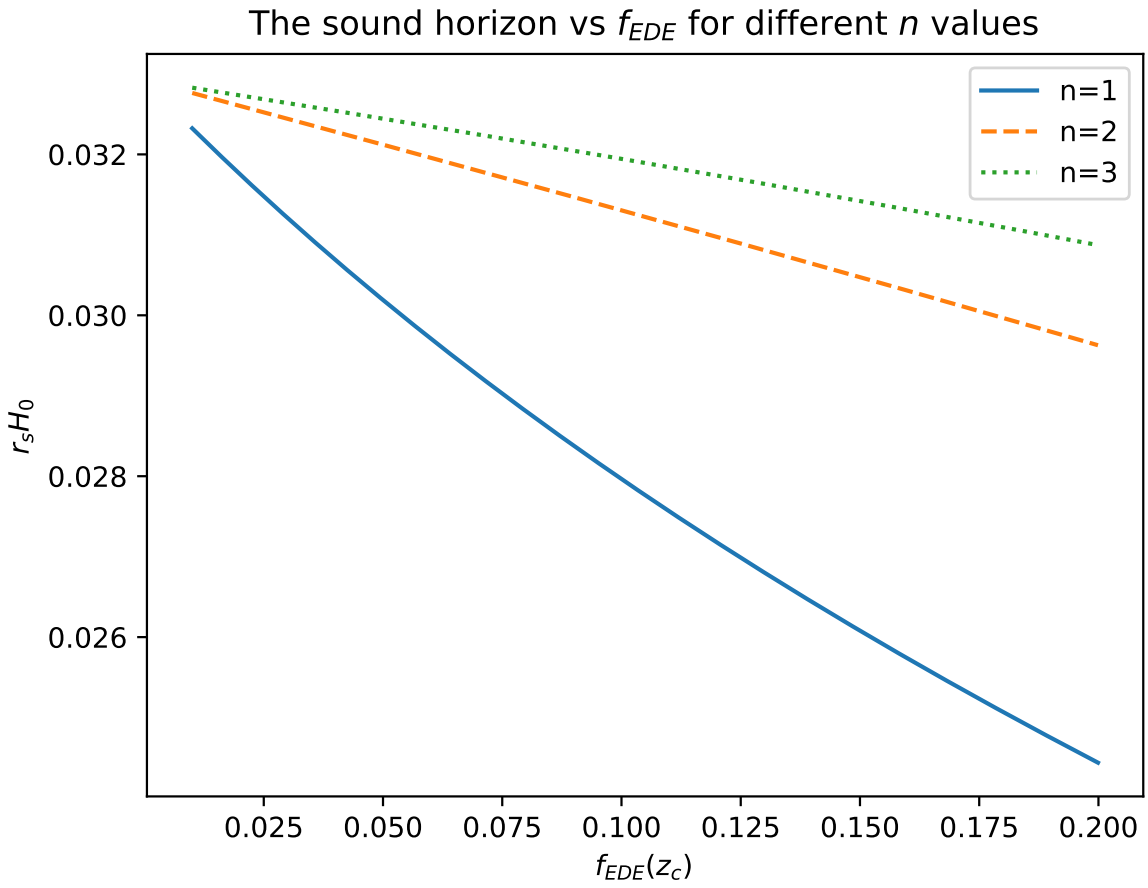

Figure 3.2: The sound horizon, normalised as $r_s\, H_0$, for an oscillating EDE model for different values of $f_{\rm EDE}(z_c)$ at critical redshift $z_c = 10^4$. Models with $n = 1$ are plotted with a solid line, $n = 2$ with a dashed line, and $n = 3$ with a dotted line.

In figure 3.2, the sound horizon r_s is plotted for different $f_{\rm EDE}(z_c)$ values at critical redshift $z_c = 10^4$. The greater the value of $f_{\rm EDE}(z_c)$, that is, the greater the contribution of early dark energy to the total energy density, the lower the value of r_s. The claim that EDE reduces the sound horizon is proved. It is somewhat surprising that the $n = 1$ model appears to have the most effect on the sound horizon.

The EDE energy density has an equation of state $w_\phi = \dfrac{p_\phi}{\rho_\phi}$:

$$w_\phi(a) = \frac{1 + w_n}{1 + \left(\frac{a_c}{a}\right)^{3(1+w_n)}} - 1 \quad . \tag{3.62}$$

The behaviour of the equation of state parameter of the EDE energy density (3.62) is

$$w_\phi \longrightarrow \begin{cases} -1 & a \to 0 \\ w_n & a \gg a_c \end{cases} \quad . \tag{3.63}$$

This indicates that the energy density in the EDE scenario is constant at early times (i.e. when $a \to 0$), but decays like $a^{-3(1+w_n)}$ once the field is dynamical (i.e. when $a \gg a_c$). Posterior distribution shows

that the EDE field must become dynamical around matter-radiation equality [111]. For $n = 1$, the energy density decays like matter (a^{-3}). For $n = 2$, the energy density decays like radiation (a^{-4}), and faster than radiation for $n = 3$ and beyond. This is apparent in figure 3.3, where (3.60) is plotted for three different values of $f_{\rm EDE}(z_c)$ (with critical redshift $z_c = 10^4$) and then for the three different n models ($n = 1$, $n = 2$ and $n = 3$). The shape of the energy density is, as expected, the same for each $f_{\rm EDE}(z_c)$ value: EDE is constant until it reaches z_c, when it decays to 0, and the $n = 2$ and $n = 3$ models decay faster than the $n = 1$ model. Also as expected, the larger the $f_{\rm EDE}(z_c)$ value, the larger the EDE energy density before the critical redshift. Similarly, the Hubble rate (3.52) for different n EDE models with various $f_{\rm EDE}(z_c)$ values (with critical redshift $z_c = 10^4$) is plotted in figure 3.4. Again, as expected, the shape of the Hubble rate is the same for all the $f_{\rm EDE}(z_c)$ values: constant until z_c and then decaying as the EDE is diluted; and the rate is larger for larger $f_{\rm EDE}(z_c)$ values. The values of the parameters used in producing these plots (and figure 3.2) appear in table A.1 in appendix A.

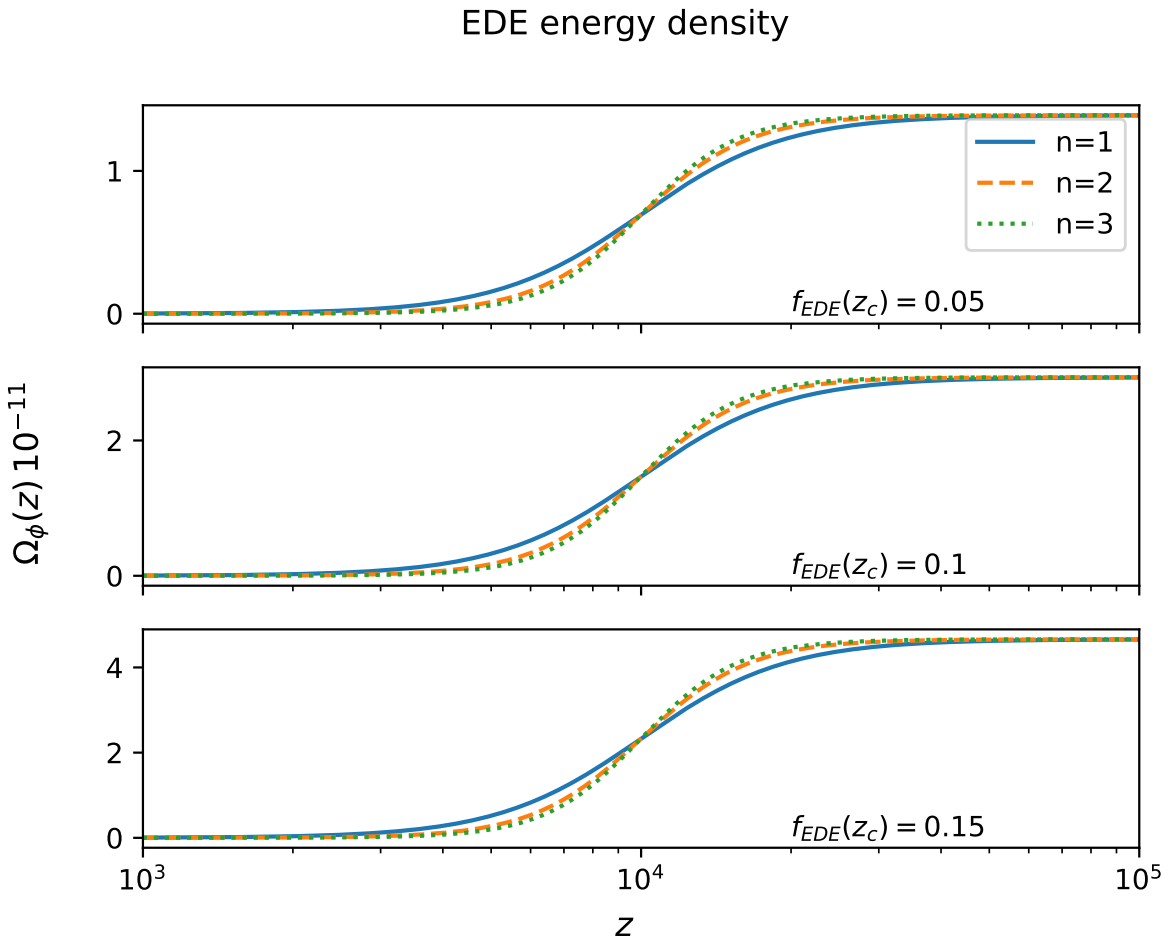

Figure 3.3: The energy density of early dark energy $\Omega_\phi(z)$ for different n and $f_{\rm EDE}(z_c)$ values, for critical redshift $z_c = 10^4$. A model with $f_{\rm EDE}(z_c) = 0.05$ is plotted in the top graph, $f_{\rm EDE}(z_c) = 0.1$ in the middle graph, and $f_{\rm EDE}(z_c) = 0.15$ in the bottom graph. Models with $n = 1$ are plotted with a solid line, $n = 2$ with a dashed line, and $n = 3$ with a dotted line. The plot starts at $z = 10^3$ because it converges after that.

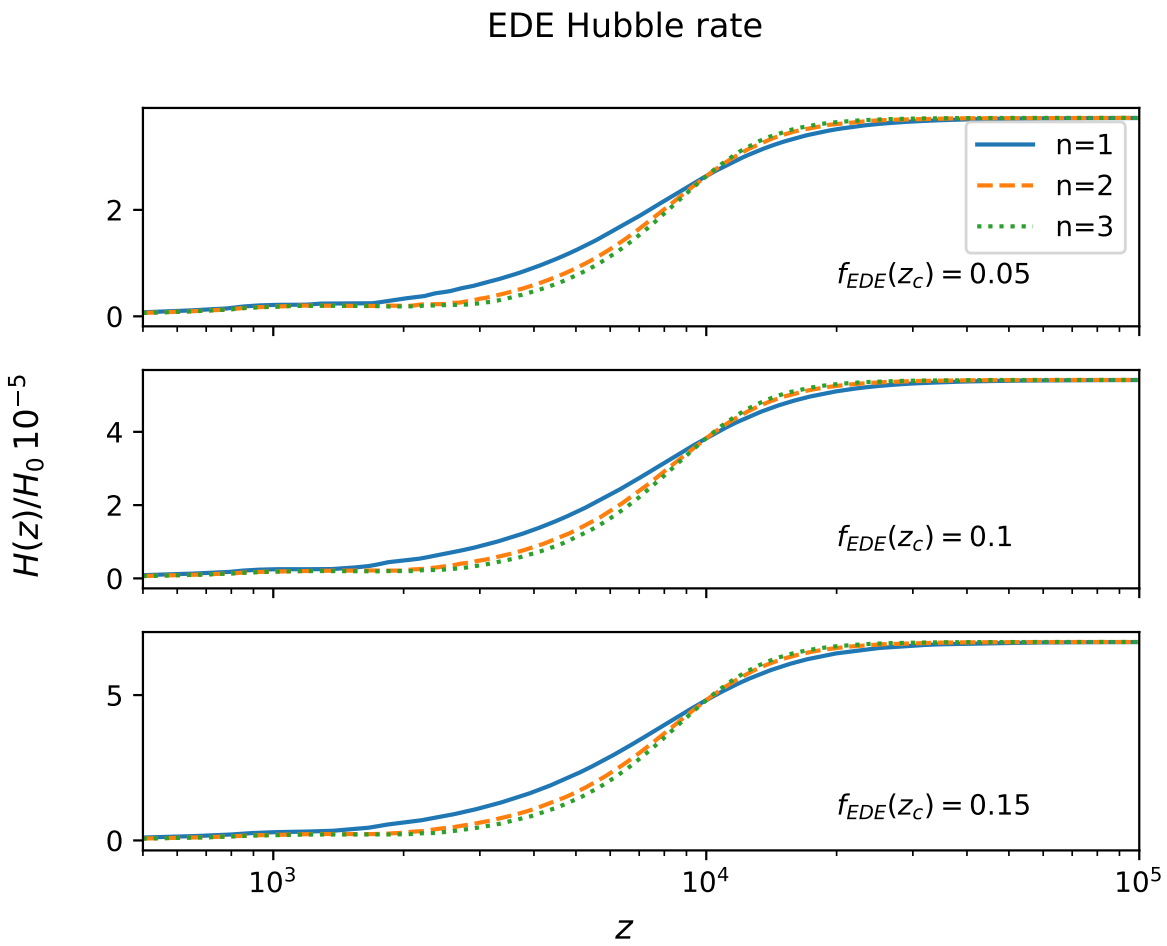

Figure 3.4: The Hubble rate $H(z)$ for a model of early dark energy, normalised as $H(z)/H_0$, with different n and $f_{\rm EDE}(z_c)$ values, for critical redshift $z_c = 10^4$. A model with $f_{\rm EDE}(z_c) = 0.05$ is plotted in the top graph, $f_{\rm EDE}(z_c) = 0.1$ in the middle graph, and $f_{\rm EDE}(z_c) = 0.15$ in the bottom graph. Models with $n = 1$ are plotted with a solid line, $n = 2$ with a dashed line, and $n = 3$ with a dotted line. The plot starts at $z = 10^3$ because it converges after that.

The $n = 2$ EDE cosmology behaves like additional radiation density, that is, increasing the effective number of neutrinos $N_{\rm eff}$. In this case the tension is increased [111]. This suggests that the EDE solution (for other n values) resolves the Hubble tension better than solutions which increase $N_{\rm eff}$, such as those that appear in [43] and [114]. However, in [110], $n = 2$ is found to be the most favourable model.

A reduction in the Hubble tension using an EDE model is also found by analysis performed in [131], [30], and [31], the latter two finding that EDE reduces the tension without degrading the fit to large scale structure (LSS) data. However, the authors of [66] and [74] suggest that current large scale structure (LSS) data exclude EDE as a potential solution to the Hubble tension: claiming that the ΛCDM parameter shifts required for the theory to preserve the fit to the CMB, quantified with

$$S_8 \equiv \sigma_8 \left(\frac{\Omega_m}{0.3}\right)^{1/2} \quad , \tag{3.64}$$

are not compatible with LSS data, and that EDE models which use a distance ladder H_0 prior and

fit well to the CMB have a worse fit to LSS data. This is repudiated in [132] and [95]. There already exists a mild tension between the CMB and LSS inferences of the amplitude of perturbations σ_8 (see chapter 4): the required increase in the σ_8 value in EDE models further exacerbates this tension. During the pre-recombination period, EDE is dominant and so contributes non-negligibly to the total energy density. Dark energy in the early universe suppresses the clustering of dark matter and baryon-photon fluid on small scales, and slightly suppresses growth perturbations. In order to preserve the fit to the CMB, σ_8 in EDE models must be increased to make up for the loss of growth perturbations. For an EDE with an oscillating scalar field, [66] found, for $n = 3$, $S_8 = 0.842 \pm 0.019$. This is in 2.1σ tension with the Dark Energy Survey Year 1 (DES-Y1) data [3]. Any model that tries to reduce the sound horizon by increasing $H(z)$ with a new dark energy-like element will encounter the same problem as EDE: in order to realise a good fit to both the CMB and SH0Es, the ΛCDM parameters will need to be shifted in such a way that is not compatible with LSS data [66]. A further problem with EDE is that it requires a lot of fine tuning.

data used	result
CMB data	no evidence for EDE $f_{\text{EDE}} < 0.087$
primary CMB + CMB lensing; BAO; Pantheon SN; SH0Es 2019; BOSS	$\approx 3\sigma$ evidence for EDE 1.9σ Hubble tension
above + LSS data (DES-Y1)	$< 2\sigma$ evidence for EDE
above + HSC and KiDS priors (cosmic shear measurements)	$f_{\text{EDE}} < 0.103$ 2.3σ Hubble tension
above *without* SH0ES 2019 H_0 prior	$f_{\text{EDE}} < 0.53$ increase Hubble tension

Table 3.1: Evidence for early dark energy in various data sets, with the SH0Es 2019 H_0 value as prior, as well as the Hubble tension between the *Planck* 2018 and SH0Es 2019 values with an EDE model. KiDS is the Kilo-Degree Survey and HSC refers to the Hyper Suprime-Cam survey. Results from analysis in [66].

The evidence for EDE in different data sets and combinations of data sets, quantified by f_{EDE} defined in equation (3.61), is analysed in [66]. Their results are summarised in table 3.1. An $n = 3$ oscillating EDE model was fitted to various data sets with the SH0Es 2019 H_0 value as a prior. No evidence for EDE was found in primary CMB alone. The Hubble tension is reduced to 1.9σ when the EDE model is fitted to the second data set (comprising the CMB, BAO, BOSS and supernovae observations), although this is partly due to the large error bars. The evidence for EDE in this data set is 2.7σ. However, the addition of LSS data substantially weakens the evidence for EDE and the Hubble tension is less reduced. This is shown in the third and fourth row of table 3.1. The exclusion of the SH0Es 2019 H_0 prior from the data set results in no evidence for EDE. An increased early universe H_0 value with a good fit to the CMB requires an increased f_{EDE} and the shift up of other

parameters. However, the CMB and LSS data do not favour a large $f_{\rm EDE}$ and the parameter shifts conflict with LSS data constraints. A larger neutrino mass would allow larger $f_{\rm EDE}$ values [66], but it is still to be established if this will be consistent with observations.

In summary, a particular EDE model with $V(\phi) \propto \phi^{2n}$ could reduce the Hubble tension rather drastically, through an increase in the early universe H_0 value by a reduction in the sound horizon at recombination. This is done via via an injection of dark energy just prior to recombination, which is constant until a critical redshift when it decays like radiation or faster. However, the increase in the values of ΛCDM parameters that is required to accommodate this is not compatible with various large scale structure data. This indicates that current observations do not allow for EDE, or at least this specific EDE model.

If EDE does turn out to be a feasible solution to the Hubble tension, then what could cause it? Parametric resonance driven by an anharmonic oscillating field could cause the rapid, scale-dependent growth of the EDE field perturbations [131], as could the dynamics of an interacting dilaton and axion [10]. A rolling axion coupled to a non-Abelian gauge group is a further suggestion in [16]. The physics of matter-radiation equality and EDE are seemingly unrelated, and fine-tuning is required for them to occur at the same time. The non-trivial coupling of neutrinos to the EDE scalar is proposed in [122] and [26] as an explanation for the near simultaneous occurance of EDE and matter-radiation equality. It is suggested in [111] that the oscillating EDE field could naturally occur in the 'string-axiverse' scenario, noting that the $n = 1$ EDE cosmology is the standard axion potential. The existence of EDE would have some further implications for our understanding of the universe. The EDE model, the current accelerated expansion and early universe inflation all taken together could suggest that the universe experiences episodic periods of accelerated expansion [111]. The presence of EDE might imply the existence of isocurvature perturbations in the CMB according to [131].

Chapter 4

Conclusion

Cosmology describes the nature of the universe. In chapter 1, the homogeneous and isotropic Friedmann-Lemaître-Robertson-Walker (FLRW) universe is established. The Hubble rate $H(z)$ (defined in equation (1.21)) is introduced, as well as distance measurements. The dynamics of the FLRW universe is discussed. The ΛCDM model, an FLRW universe with $\Lambda \neq 0$, some cold dark matter and no curvature, is the generally accepted model to describe the universe. The test of a model is how well it reproduces observations. ΛCDM is the accepted model because it accounts for most current observations. However, there is not an agreement on the Hubble rate today, H_0. The value of H_0 inferred by assuming ΛCDM in the *Planck* observations of the CMB is $H_0 = 67.36 \pm 0.54\,\mathrm{km\,s^{-1}\,Mpc^{-1}}$, which is in 4.2σ tension with the most recent value measured by SH0Es using direct observations of the SNIa distance ladder, which is $H_0 = 73.2 \pm 1.3\,\mathrm{km\,s^{-1}\,Mpc^{-1}}$. The ΛCDM model does not appear to reproduce observations of H_0 in the late universe. The tension between the early and late universe H_0 values persists even when different data sets and methods are used: this is shown in figure 2.1 where the values obtained using late universe data favour larger H_0 values than those inferred using early universe data. Note, however, that many of these values do not have the $\sim 1\%$ precision required for comparison with the SH0Es and *Planck* values.

How H_0 is inferred from the CMB, as well as from BAO data, is discussed in section 2.1. Elaboration on the distance measurements introduced in chapter 1 appears in section 2.2 to enable a discussion of how H_0 is obtained from late universe measurements: the SNIa distance ladder in 2.2.1, lensing in 2.2.2 and gravitational waves in 2.2.3. The Type Ia supernovae distance ladder, and its use in determining H_0, is explained in section 2.2.1 with figure 2.4. An introduction to lensing, and how it is used to obtain distance measurements is given in section 2.2.2. The H_0 determinations from different lensing data sets, as well as from lensing data sets combined with other data sets, appears in figure 2.6, with a comparison to the *Planck* and SH0Es values. It shows that the uncertainties associated with this measurement are large, and the precision is not quite good enough to allow definitive comparisons with *Planck* and SH0Es. However, lensing does seem to favour larger H_0 values. In section 2.2.3, gravitational waves and their use in determining H_0 are discussed. There are many systematics related to the detection of gravitational waves, and as such the associated H_0 measurement has large

error bars. As more detections are made, the precision should improve in order for the gravitational wave H_0 determination to be comparable to *Planck* and SH0Es. A discussion of how the remainder of the values appearing in figure 2.1 are obtained appears in the introductory pages of chapter 2. Determinations of H_0 that are wholly independent of both the CMB and the SNIa distance ladder are needed to confirm that there is indeed a tension between the early and late universe that is manifested through the Hubble tension. As already stated, the measurements need to have a comparable precision of $\sim 1\%$ in order to do so. Few do, especially in the late universe. In chapter 2, the plans to improve the precision of and reduce the inaccuracies in various measurements are outlined. The SH0Es team has managed to improve the precision of their result to almost 1%, and work is being performed to achieve 1% precision.

If one accepts that there is a tension between the early and late universe (and the growing discrepancy despite improvement in precision are compelling evidence that it does exist), an enormous number of possible new physics and models have been proposed to resolve it. Some of these are discussed in chapter 3, which begins with a discussion of what a possible solution needs to achieve in order to be considered viable. At the most basic level, it must not result in a worse fit to observations than ΛCDM. It is worth noting that many purportedly successful solutions do not in fact change the value of the early or late H_0 determinations, but instead increase the error bars so that the results are in statistical agreement but no resolution has in fact been obtained. Selected proposed solutions to the Hubble tension are loosely categorised in chapter 3, however it is not intended to be an exhaustive list. Solutions that change post-recombination physics are discussed in section 3.1. These solutions are not viable because they do not take into account the fact that the SNIa distance ladder does not measure H_0 directly, and so impose a SH0Es H_0 prior without ensuring that the model is consistent with the magnitude-redshift relation of SNIa. In section 3.2, models that introduce a form of early dark energy (EDE) are explored, with specific attention given to those whose EDE scalar field ϕ have a potential $V(\phi) \propto \phi^{2n}$. Just before recombination, these models inject additional dark energy which is constant until a critical redshift and then decays like radiation or faster. This lowers the sound horizon at recombination and results in a larger early universe H_0 value which reduces the Hubble tension. However, current observations do not appear to allow for EDE because the required ΛCDM parameter shifts to accommodate it are not compatible with various large scale structure (LSS) data: see table 3.1 for evidence (or rather the lack thereof) for EDE in various data sets.

In conclusion, there is strong evidence - namely, the improvement in precision resulting in a larger discrepancy between *Planck* and SH0Es and various corroborating independent measurements (albeit with large uncertainties, but these are projected to improve) - that there is a significant tension between the early universe and late universe determinations of H_0, the present day rate of expansion, that indicates a need to modify or expand ΛCDM. A vast array of solutions have been proposed to resolve the tension, however none seem able to do so yet.

The tension between the *Planck* and SH0Es values of H_0 is not the only indication that there is a conflict between the early and late universes that might necessitate a modification or expansion of ΛCDM. There are several other tensions between parameters inferred from the CMB while assuming

ΛCDM and those obtained from high redshift LSS observations.

As briefly mentioned in section 3.2, there is a tension between the inferences of σ_8, the amplitude of density fluctuations, made by the CMB and by LSS observations. The values of σ_8, or equivalently S_8 which is given by equation (3.64), obtained by the CMB are slightly greater than those found by LSS observations. The ΛCDM analysis of the CMB observations made by *Planck* [8] infers $S_8 = 0.830 \pm 0.013$; whereas a combination of three independent LSS measurements together give $S_8 = 0.770^{+0.018}_{-0.016}$ [66]. The early and late universe values are in 2.7σ tension with each other. Other LSS measurements, such as galaxy cluster number counts, also tend to favour lower σ_8 values [17]. Furthermore, there is a tension between the values of σ_8 and $\Omega_{m,0}$ that are predicted from the CMB and those determined from galaxy clusters. The value of $\sigma_8 \sqrt{\frac{\Omega_{m,0}}{0.3}}$ inferred from the CMB by *Planck* in 2015 is 0.851 ± 0.013 [6] is in 2.5σ tension with the value from clusters of 0.745 ± 0.039 [23]. The σ_8 tension varies depending on the data set used and assumptions made, but remains below 3σ. This tension is not as large as the Hubble tension but is still significant. Analysis in [17] shows there is a strong positive correlation between H_0 and σ_8 which is prevalent across data sets, regardless of the cosmological model used. This correlation indicates that if H_0 increases, then σ_8 also increases. But low redshift data, as shown in chapter 2 and figure 2.1, prefers larger H_0 values whereas galaxy clusters prefer low σ_8 values. This appears to indicate that these two tensions cannot be resolved together.

Another anomaly arises with A_{lens}, a nuisance parameter used to match CMB anisotropies and CMB lensing data. A value of 1 is expected from ΛCDM but *Planck* 2015 gives a value of 1.22 ± 0.1 [6]. Additionally, when A_{lens} is inferred from the smoothing of high and angular temperature power spectrum peaks, the value is in $\gtrsim 2\sigma$ tension with the value inferred from CMB lensing data [139]. If this tension is confirmed, it could be evidence that our knowledge of the relationship between CMB anisotropies and structure growth is somehow lacking [139] and could point towards a need for new physics. Another tension is one between the BAO (at $z < 1$) inferred cosmological parameters and those of Lyman-α forest BAO data at higher redshifts [139].

The statistical errors in both early and late universe measurements have, as discussed, decreased. The increase in the Hubble tension at the same time indicates that this tension is not as a result of a statistical fluke or unaccounted for systematics but as a sign of the need for new physics. The various other tensions between high redshift CMB data and low redshift direct measurements given above seem to further support some further error or omission in ΛCDM. A proposed solution to the Hubble tension would be more credible if it also resolved these tensions - at the very least it should not make them significantly worse. Future surveys and observations, the improved precision in measurement and analysis, and the blind reanalysis of existing data taking into account previously unaccounted for systematic errors will either further confirm the existence of the Hubble tension, or show that it is in fact a coincidence or the result of an error.

Appendix A

The parameter values used in creating figures 3.2, 3.3, and 3.4 appear in table A.1.

parameter		value
curvature	K	0
matter density (present day)	$\Omega_{m,0}$	0.32
dark energy density	Ω_Λ	0.68
radiation density (present day)	$\Omega_{r,0}$	10^{-4}
baryon density (present day)	$\Omega_{b,0}$	0.05

Table A.1: The values of the parameters used

Bibliography

[1] Rubin Observatory. `https://www.lsst.org/`.

[2] B. P. Abbott et al. A gravitational-wave standard siren measurement of the Hubble constant. *Nature*, 551(7678):85–88, 2017. **arxiv:1710.05835**.

[3] T. M. C. Abbott et al. Dark Energy Survey Year 1 Results: A Precise H_0 Measurement from DES Y1, BAO, and D/H Data. *MNRAS*, 480:3879, 2018. **arxiv:1711.00403**.

[4] G. E. Addison, D. J. Watts, C. L. Bennett, M. Halpern, G. Hinshaw, and J. L. Weiland. Elucidating ΛCDM: Impact of Baryon Acoustic Oscillation Measurements on the Hubble Constant Discrepancy. *Astrophys. J.*, 853(2):119, 2018. **arxiv:1707.06547**.

[5] P. A. R. Ade et al. Planck 2013 results. XVI. Cosmological parameters. *Astron. Astrophys.*, 571:A16, 2014. **arxiv:1303.5076**.

[6] P. A. R. Ade et al. Planck 2015 results. XXIV. Cosmology from Sunyaev-Zeldovich cluster counts. *Astron. Astrophys.*, 594:A24, 2016. **arxiv:1502.01597**.

[7] N. Aghanim et al. Planck 2018 results. V. CMB power spectra and likelihoods. *Astron. Astrophys.*, 641:A5, 2020. **arxiv:1907.12875**.

[8] N. Aghanim et al. Planck 2018 results. VI. Cosmological parameters. *Astron. Astrophys.*, 641:A6, 2020. **arxiv:1807.06209**.

[9] Prateek Agrawal, Francis-Yan Cyr-Racine, David Pinner, and Lisa Randall. Rock 'n' Roll Solutions to the Hubble Tension. *arXiv e-prints*, 2019. **arxiv:1904.01016**.

[10] Stephon Alexander and Evan McDonough. Axion-Dilaton Destabilization and the Hubble Tension. *Phys. Lett. B*, 797:134830, 2019. **arxiv:1904.08912**.

[11] Hassan Amirhashchi and Anil Kumar Yadav. Interacting Dark Sectors in Anisotropic Universe: Observational Constraints and H_0 Tension. *arXiv e-prints*, 2020. **arxiv:2001.03775**.

[12] Luis A. Anchordoqui. Decaying dark matter, the H_0 tension, and the lithium problem. *Phys. Rev. D*, 103(3):035025, 2021. **arxiv:2010.09715**.

[13] Daniel Baumann. Cosmology lectures. University of Cambridge, 2012.

[14] Wim Beenakker and David Venhoek. A structured analysis of Hubble tension. *arXiv e-prints*, 2021. **arxiv:2101.01372**.

[15] Giampaolo Benevento, Wayne Hu, and Marco Raveri. Can Late Dark Energy Transitions Raise the Hubble constant? *Phys. Rev. D*, 101(10):103517, 2020. **arxiv:2002.11707**.

[16] Kim V. Berghaus and Tanvi Karwal. Thermal Friction as a Solution to the Hubble Tension. *Phys. Rev. D*, 101(8):083537, 2020. **arxiv:1911.06281**.

[17] Archita Bhattacharyya, Ujjaini Alam, Kanhaiya Lal Pandey, Subinoy Das, and Supratik Pal. Are H_0 and σ_8 tensions generic to present cosmological data? *Astrophys. J.*, 876(2):143, 2019. **arxiv:1805.04716**.

[18] S. Birrer et al. H0LiCOW - IX. Cosmographic analysis of the doubly imaged quasar SDSS 1206+4332 and a new measurement of the Hubble constant. *MNRAS*, 484:4726, 2019. **arxiv:1809.01274**.

[19] S. Birrer et al. TDCOSMO - IV. Hierarchical time-delay cosmography – joint inference of the Hubble constant and galaxy density profiles. *Astron. Astrophys.*, 643:A165, 2020. **arxiv:2007.02941**.

[20] Nikita Blinov, Celeste Keith, and Dan Hooper. Warm Decaying Dark Matter and the Hubble Tension. *JCAP*, 06:005, 2020. **arxiv:2004.06114**.

[21] Nikita Blinov, Kevin James Kelly, Gordan Z Krnjaic, and Samuel D McDermott. Constraining the Self-Interacting Neutrino Interpretation of the Hubble Tension. *Phys. Rev. Lett.*, 123(19):191102, 2019. **arxiv:1905.02727**.

[22] Nikita Blinov and Gustavo Marques-Tavares. Interacting radiation after Planck and its implications for the Hubble Tension. *JCAP*, 09:029, 2020. **arxiv:2003.08387**.

[23] Hans Böhringer, Gayoung Chon, and Chris A. Collins. The extended ROSAT-ESO Flux Limited X-ray Galaxy Cluster Survey (REFLEX II) IV. X-ray Luminosity Function and First Constraints on Cosmological Parameters. *Astron. Astrophys.*, 570:A31, 2014. **arxiv:1403.2927**.

[24] Thejs Brinckmann, Jae Hyeok Chang, and Marilena LoVerde. Self-interacting neutrinos, the Hubble parameter tension, and the cosmic microwave background. *Phys. Rev. D*, 104(6):063523, 2021. **arxiv:2012.11830**.

[25] David Camarena and Valerio Marra. On the use of the local prior on the absolute magnitude of Type Ia supernovae in cosmological inference. *Mon. Not. Roy. Astron. Soc.*, 504:5164–5171, 2021. **arxiv:2101.08641**.

[26] Mariana Carrillo González, Qiuyue Liang, Jeremy Sakstein, and Mark Trodden. Neutrino-Assisted Early Dark Energy: Theory and Cosmology. *JCAP*, 04:063, 2021. **arxiv:2011.09895**.

[27] A. Chen et al. Constraints on dark matter to dark radiation conversion in the late universe with DES-Y1 and external data. *Phys. Rev. D*, 103(12):123528, 2021. **arxiv:2011.04606**.

[28] Geoff C. F. Chen et al. A SHARP view of H0LiCOW: H_0 from three time-delay gravitational lens systems with adaptive optics imaging. *Mon. Not. Roy. Astron. Soc.*, 490(2):1743–1773, 2019. **arxiv:1907.02533**.

[29] Hsin-Yu Chen, Maya Fishbach, and Daniel E. Holz. A two per cent Hubble constant measurement from standard sirens within five years. *Nature*, 562(7728):545–547, 2018. **arxiv:1712.06531**.

[30] Anton Chudaykin, Dmitry Gorbunov, and Nikita Nedelko. Combined analysis of Planck and SPTPol data favors the early dark energy models. *JCAP*, 08:013, 2020. **arxiv:2004.13046**.

[31] Anton Chudaykin, Dmitry Gorbunov, and Nikita Nedelko. Exploring an early dark energy solution to the hubble tension with Planck and SPTPol data. *Phys. Rev. D*, 103:043529, 2021. **arxiv:2011.04682**.

[32] Steven J. Clark, Kyriakos Vattis, and Savvas M. Koushiappas. Cosmological constraints on late-Universe decaying dark matter as a solution to the H_0 tension. *Phys. Rev. D*, 103(4):043014, 2021. **arxiv:2006.03678**.

[33] Thomas Collett, Francesco Montanari, and Syksy Rasanen. Model-Independent Determination of H_0 and Ω_{K0} from Strong Lensing and Type Ia Supernovae. *Phys. Rev. Lett.*, 123(23):231101, 2019. **arxiv:1905.09781**.

[34] Paolo Cremonese and Vincenzo Salzano. High accuracy on H_0 constraints from gravitational wave lensing events. *Phys. Dark Univ.*, 28:100517, 2020. **arxiv:1911.11786**.

[35] Andrei Cuceu, James Farr, Pablo Lemos, and Andreu Font-Ribera. Baryon Acoustic Oscillations and the Hubble Constant: Past, Present and Future. *JCAP*, 10:044, 2019. **arxiv:1906.11628**.

[36] Francis-Yan Cyr-Racine. Cosmic Expansion: A mini review of the Hubble-Lemaitre tension. In *55th Rencontres de Moriond on Electroweak Interactions and Unified Theories*, 2021. **arxiv:2105.09409**.

[37] T. de Jaeger, B. E. Stahl, W. Zheng, A. V. Filippenko, A. G. Riess, and L. Galbany. A measurement of the Hubble constant from Type II supernovae. *Mon. Not. Roy. Astron. Soc.*, 496(3):3402–3411, 2020. **arxiv:2006.03412**.

[38] Harry Desmond, Bhuvnesh Jain, and Jeremy Sakstein. Local resolution of the Hubble tension: The impact of screened fifth forces on the cosmic distance ladder. *Phys. Rev. D*, 100(4):043537, 2019. [Erratum: Phys.Rev.D 101, 069904 (2020), Erratum: Phys.Rev.D 101, 129901 (2020)]. **arxiv:1907.03778**.

[39] Eleonora Di Valentino et al. Cosmology Intertwined II: The Hubble Constant Tension. *Astropart. Phys.*, 131:102605, 2021. **arxiv:2008.11284**.

[40] Eleonora Di Valentino, Eric V. Linder, and Alessandro Melchiorri. Vacuum phase transition solves the H_0 tension. *Phys. Rev.*, D97(4):043528, 2018. **arxiv:1710.02153**.

[41] Eleonora Di Valentino, Alessandro Melchiorri, and Olga Mena. Can interacting dark energy solve the H_0 tension? *Phys. Rev. D*, 96(4):043503, 2017. **arxiv:1704.08342**.

[42] Eleonora Di Valentino, Alessandro Melchiorri, Olga Mena, and Sunny Vagnozzi. Interacting dark energy in the early 2020s: A promising solution to the H_0 and cosmic shear tensions. *Phys. Dark Univ.*, 30:100666, 2020. **arxiv:1908.04281**.

[43] Eleonora Di Valentino, Olga Mena, Supriya Pan, Luca Visinelli, Weiqiang Yang, Alessandro Melchiorri, David F. Mota, Adam G. Riess, and Joseph Silk. In the realm of the Hubble tension—a review of solutions. *Class. Quant. Grav.*, 38(15):153001, 2021. **arxiv:2103.01183**.

[44] Eleonora Di Valentino, Ankan Mukherjee, and Anjan A. Sen. Dark Energy with Phantom Crossing and the H_0 Tension. *Entropy*, 23(4):404, 2021. **arxiv:2005.12587**.

[45] Qianhang Ding, Tomohiro Nakama, and Yi Wang. A gigaparsec-scale local void and the Hubble tension. *Sci. China Phys. Mech. Astron.*, 63(9):290403, 2020. **arxiv:1912.12600**.

[46] A. Domínguez, R. Wojtak, J. Finke, M. Ajello, K. Helgason, F. Prada, A. Desai, V. Paliya, L. Marcotulli, and D. H. Hartmann. A new measurement of the Hubble constant and matter content of the Universe using extragalactic background light γ-ray attenuation. *The Astrophysical Journal*, 885(2):137, 2019. **arxiv:1903.12097**.

[47] Ruth Durrer. *The Cosmic Microwave Background*. Cambirdge University Press, 2008.

[48] G. Efstathiou. A Lockdown Perspective on the Hubble Tension (with comments from the SH0ES team). *arXiv e-prints*, 2020. **arxiv:2007.10716**.

[49] George Efstathiou. To H0 or not to H0? *Mon. Not. Roy. Astron. Soc.*, 505(3):3866–3872, 2021. **arxiv:2103.08723**.

[50] George F. R. Ellis, Roy Maartens, and Malcolm A. H. MacCallum. *Relativistic Cosmology*. Cambridge University Press, 2012.

[51] Miguel Escudero and Samuel J. Witte. A CMB Search for the Neutrino Mass Mechanism and its Relation to the H_0 Tension. *Eur. Phys. J. C*, 80(4):294, 2020. **arxiv:1909.04044**.

[52] Pierre Fleury, Hélène Dupuy, and Jean-Philippe Uzan. Can all cosmological observations be accurately interpreted with a unique geometry? *Phys. Rev. Lett.*, 111:091302, 2013. **arxiv:1304.7791**.

[53] Pierre Fleury, Hélène Dupuy, and Jean-Philippe Uzan. Interpretation of the Hubble diagram in a nonhomogeneous universe. *Phys. Rev.*, D87(12):123526, 2013. **arxiv:1302.5308**.

[54] Wendy L. Freedman, Barry F. Madore, Brad K. Gibson, Laura Ferrarese, Daniel D. Kelson, Shoko Sakai, Jeremy R. Mould, Jr. Robert C. Kennicutt, Holland C. Ford, John A. Graham, John P. Huchra, Shaun M. G. Hughes, Garth D. Illingworth, Lucas M. Macri, and Peter B. Stetson. Final Results from the Hubble Space Telescope Key Project to Measure the Hubble Constant. *The Astrophysical Journal*, 553(1):47–72, 2001. **doi:10.1086/320638**.

[55] Wendy L. Freedman, Barry F. Madore, Dylan Hatt, Taylor J. Hoyt, In Sung Jang, Rachael L. Beaton, Christopher R. Burns, Myung Gyoon Lee, Andrew J. Monson, Jillian R. Neeley, M. M.

Phillips, Jeffrey A. Rich, and Mark Seibert. The Carnegie-Chicago Hubble Program. VIII. An Independent Determination of the Hubble Constant Based on the Tip of the Red Giant Branch. *The Astrophysical Journal*, 882(1):34, 2019. **arxiv:1907.05922**.

[56] Wendy L. Freedman, Barry F. Madore, Victoria Scowcroft, Chris Burns, Andy Monson, S. Eric Persson, Mark Seibert, and Jane Rigby. Carnegie Hubble Program: A Mid-Infrared Calibration of the Hubble Constant. *The Astrophysical Journal*, 758(1):24, 2012. **arxiv:1208.3281**.

[57] E. E. E. Gall, R. Kotak, B. Leibundgut, S. Taubenberger, W. Hillebrandt, and M. Kromer. Applying the expanding photosphere and standardized candle methods to Type II-Plateau supernovae at cosmologically significant redshifts: the distance to SN 2013eq. *Astron. Astrophys.*, 592:A129, 2016. **arxiv:1603.04730**.

[58] V. Gayathri, J. Healy, J. Lange, B. O'Brien, M. Szczepanczyk, I. Bartos, M. Campanelli, S. Klimenko, C. O. Lousto, and R. O'Shaughnessy. Measuring the Hubble Constant with GW190521 as an Eccentric black hole Merger and Its Potential Electromagnetic Counterpart. *The Astrophysical Journal*, 908(2):L34, feb 2021. **doi:10.3847/2041-8213/abe388**.

[59] Graciela B. Gelmini, Alexander Kusenko, and Volodymyr Takhistov. Possible Hints of Sterile Neutrinos in Recent Measurements of the Hubble Parameter. *JCAP*, 06:002, 2021. **arxiv:1906.10136**.

[60] Adrià Gómez-Valent, Valeria Pettorino, and Luca Amendola. Update on coupled dark energy and the H_0 tension. *Phys. Rev. D*, 101(12):123513, 2020. **arxiv:2004.00610**.

[61] Alex Hall. Cosmology from weak lensing alone and implications for the Hubble tension. *Mon. Not. Roy. Astron. Soc.*, 505(4):4935–4955, 2021. **arxiv:2104.12880**.

[62] Balakrishna S. Haridasu and Matteo Viel. Late-time decaying dark matter: constraints and implications for the H_0-tension. *Mon. Not. Roy. Astron. Soc.*, 497(2):1757–1764, 2020. **arxiv:2004.07709**.

[63] Hong-Jian He, Yin-Zhe Ma, and Jiaming Zheng. Resolving Hubble Tension by Self-Interacting Neutrinos with Dirac Seesaw. *JCAP*, 11:003, 2020. **arxiv:2003.12057**.

[64] Jian-hua He. Accurate method to determine the systematics due to the peculiar velocities of galaxies in measuring the Hubble constant from gravitational-wave standard sirens. *Phys. Rev. D*, 100(2):023527, 2019. **arxiv:1903.11254**.

[65] Asta Heinesen and Thomas Buchert. Solving the curvature and Hubble parameter inconsistencies through structure formation-induced curvature. *Class. Quant. Grav.*, 37(16):164001, 2020. [Erratum: Class.Quant.Grav. 37, 229601 (2020)]. **arxiv:2002.10831**.

[66] J. Colin Hill, Evan McDonough, Michael W. Toomey, and Stephon Alexander. Early dark energy does not restore cosmological concordance. *Phys. Rev. D*, 102(4):043507, 2020. **arxiv:2003.07355**.

[67] Daniel Holz, Scott Hughes, and Bernard Schutz. Measuring cosmic distances with standard sirens. *Physics Today*, 71:34–40, 2018. **doi:10.1063/PT.3.4090**.

[68] Kenta Hotokezaka, Ehud Nakar, Ore Gottlieb, Samaya Nissanke, Kento Masuda, Gregg Hallinan, Kunal P. Mooley, and Adam. T. Deller. A Hubble constant measurement from superluminal motion of the jet in GW170817. *Nature Astron.*, 3(10):940–944, 2019. **arxiv:1806.10596**.

[69] Shaoqi Hou, Xi-Long Fan, and Zong-Hong Zhu. Constraining cosmological parameters from strong lensing with DECIGO and B-DECIGO sources. *Mon. Not. Roy. Astron. Soc.*, 507:761, 2021. **arxiv:2106.01765**.

[70] Andrzej Hryczuk and Krzysztof Jodłowski. Self-interacting dark matter from late decays and the H_0 tension. *Phys. Rev. D*, 102(4):043024, 2020. **arxiv:2006.16139**.

[71] Caroline Huang, Adam Riess, Wenlong Yuan, Lucas Macri, Nadia Zakamska, Stefano Casertano, Patricia Whitelock, Samantha Hoffmann, Alexei Filippenko, and Daniel Scolnic. Hubble Space Telescope Observations of Mira Variables in the SN Ia Host NGC 1559: An Alternative Candle to Measure the Hubble Constant. *The Astrophysical Journal*, 889:5, 2020. **arxiv:1908.10883**.

[72] Edwin Hubble. A relation between distance and radial velocity among extra-galactic nebulae. *Proceedings of the National Academy of Sciences*, 15(3):168–173, 1929.

[73] S. Huber, S. H. Suyu, D. Ghoshdastidar, S. Taubenberger, V. Bonvin, J. H. H. Chan, M. Kromer, U. M. Noebauer, S. A. Sim, and L. Leal-Taixé. HOLISMOKES - VII. Time-delay measurement of strongly lensed SNe Ia using machine learning. *arXiv e-prints*, 2021. **arxiv:2108.02789**.

[74] Mikhail M. Ivanov, Evan McDonough, J. Colin Hill, Marko Simonović, Michael W. Toomey, Stephon Alexander, and Matias Zaldarriaga. Constraining Early Dark Energy with Large-Scale Structure. *Phys. Rev. D*, 102(10):103502, 2020. **arxiv:2006.11235**.

[75] Karsten Jedamzik, Levon Pogosian, and Gong-Bo Zhao. Why reducing the cosmic sound horizon alone can not fully resolve the Hubble tension. *Commun. in Phys.*, 4:123, 2021. **arxiv:2010.04158**.

[76] Raul Jimenez, Andrea Cimatti, Licia Verde, Michele Moresco, and Benjamin Wandelt. The local and distant Universe: stellar ages and H_0. *JCAP*, 1903(03):043, 2019. **arxiv:1902.07081**.

[77] D. O. Jones et al. Should Type Ia Supernova Distances be Corrected for their Local Environments? *Astrophys. J.*, 867(2):108, 2018. **arxiv:1805.05911**.

[78] Lavrentios Kazantzidis and Leandros Perivolaropoulos. σ_8 Tension. Is Gravity Getting Weaker at Low z? Observational Evidence and Theoretical Implications. In *Modified Gravity and Cosmology: An Update by the CANTATA Network*, pages 507–537. Springer International Publishing, 2021.

[79] W. D'Arcy Kenworthy, Dan Scolnic, and Adam Riess. The Local Perspective on the Hubble Tension: Local Structure Does Not Impact Measurement of the Hubble Constant. *Astrophys. J.*, 875(2):145, 2019. **arxiv:1901.08681**.

[80] Nima Khosravi, Shant Baghram, Niayesh Afshordi, and Natacha Altamirano. H_0 tension as a hint for a transition in gravitational theory. *Phys. Rev.*, D99(10):103526, 2019. **arxiv:1710.09366**.

[81] Lloyd Knox and Marius Millea. Hubble constant hunter's guide. *Phys. Rev. D*, 101(4):043533, 2020. **arxiv:1908.03663**.

[82] Arpine Kozmanyan, Hervé Bourdin, Pasquale Mazzotta, Elena Rasia, and Mauro Sereno. Deriving the Hubble constant using Planck and XMM-Newton observations of galaxy clusters. *Astron. Astrophys.*, 621:A34, 2019. **arxiv:1809.09560**.

[83] Christina D. Kreisch, Francis-Yan Cyr-Racine, and Olivier Doré. Neutrino puzzle: Anomalies, interactions, and cosmological tensions. *Phys. Rev. D*, 101(12):123505, 2020. **arxiv:1902.00534**.

[84] G. Lemaître. Un Univers homogène de masse constante et de rayon croissant rendant compte de la vitesse radiale des nébuleuses extra-galactiques. *Annales de la Société Scientifique de Bruxelles*, 47:49–59, 1927.

[85] Nan Li, Christoph Becker, and Simon Dye. The impact of line-of-sight structures on measuring H0 with strong lensing time delays. *Mon. Not. Roy. Astron. Soc.*, 504(2):2224–2234, 2021. **arxiv:2006.08540**.

[86] Meng-Xiang Lin, Giampaolo Benevento, Wayne Hu, and Marco Raveri. Acoustic Dark Energy: Potential Conversion of the Hubble Tension. *Phys. Rev. D*, 100(6):063542, 2019. **arxiv:1905.12618**.

[87] Kun-Feng Lyu, Emmanuel Stamou, and Lian-Tao Wang. Self-interacting neutrinos: Solution to Hubble tension versus experimental constraints. *Phys. Rev. D*, 103(1):015004, 2021. **arxiv:2004.10868**.

[88] E. Macaulay et al. First Cosmological Results using Type Ia Supernovae from the Dark Energy Survey: Measurement of the Hubble Constant. *Mon. Not. Roy. Astron. Soc.*, 486(2):2184–2196, 2019. **arxiv:1811.02376**.

[89] Barry F. Madore and Wendy L. Freedman. The Cepheid Distance Scale. *Publications of the Astronomical Society of the Pacific*, 103:933, 1991. **doi:10.1086/132911**.

[90] M. Millon et al. TDCOSMO. I. An exploration of systematic uncertainties in the inference of H_0 from time-delay cosmography. *Astron. Astrophys.*, 639:A101, 2020. **arxiv:1912.08027**.

[91] Edvard Mortsell, Ariel Goobar, Joel Johansson, and Suhail Dhawan. The Hubble Tension Bites the Dust: Sensitivity of the Hubble Constant Determination to Cepheid Color Calibration. *arXiv e-prints*, 2021. **arxiv:2105.11461**.

[92] Edvard Mortsell, Ariel Goobar, Joel Johansson, and Suhail Dhawan. The Hubble Tension Revisited: Additional Local Distance Ladder Uncertainties. *arXiv e-prints*, 2021. **arxiv:2106.09400**.

[93] Suvodip Mukherjee, Archisman Ghosh, Matthew J. Graham, Christos Karathanasis, Mansi M. Kasliwal, Ignacio Magaña Hernandez, Samaya M. Nissanke, Alessandra Silvestri, and Benjamin D. Wandelt. First measurement of the Hubble parameter from bright binary black hole GW190521. *arXiv e-prints*, 2020. **arxiv:2009.14199**.

[94] Suvodip Mukherjee, Guilhem Lavaux, François R. Bouchet, Jens Jasche, Benjamin D. Wandelt, Samaya M. Nissanke, Florent Leclercq, and Kenta Hotokezaka. Velocity correction for Hubble constant measurements from standard sirens. *Astron. Astrophys.*, 646:A65, 2021. **arxiv:1909.08627**.

[95] Riccardo Murgia, Guillermo F. Abellán, and Vivian Poulin. Early dark energy resolution to the Hubble tension in light of weak lensing surveys and lensing anomalies. *Phys. Rev. D*, 103(6):063502, 2021. **arxiv:2009.10733**.

[96] Edvard Mörtsell and Suhail Dhawan. Does the Hubble constant tension call for new physics? *JCAP*, 1809(09):025, 2018. **arxiv:1801.07260**.

[97] Florian Niedermann and Martin S. Sloth. New Early Dark Energy is compatible with current LSS data. *Phys. Rev. D*, 103(10):103537, 2021. **arxiv:2009.00006**.

[98] Nils A. Nilsson. Preferred-frame effects, the H_0 tension, and probes of Hořava–Lifshitz gravity. *Eur. Phys. J. Plus*, 135(4):361, 2020. **arxiv:1910.14414**.

[99] Rafael C. Nunes. Structure formation in $f(T)$ gravity and a solution for H_0 tension. *JCAP*, 05:052, 2018. **arxiv:1802.02281**.

[100] A. Palmese et al. A statistical standard siren measurement of the Hubble constant from the LIGO/Virgo gravitational wave compact object merger GW190814 and Dark Energy Survey galaxies. *Astrophys. J. Lett.*, 900(2):L33, 2020. **arxiv:2006.14961**.

[101] Supriya Pan, Weiqiang Yang, Eleonora Di Valentino, Emmanuel N. Saridakis, and Subenoy Chakraborty. Interacting scenarios with dynamical dark energy: Observational constraints and alleviation of the H_0 tension. *Phys. Rev. D*, 100(10):103520, 2019. **arxiv:1907.07540**.

[102] Supriya Pan, Weiqiang Yang, and Andronikos Paliathanasis. Non-linear interacting cosmological models after Planck 2018 legacy release and the H_0 tension. *Mon. Not. Roy. Astron. Soc.*, 493(3):3114–3131, 2020. **arxiv:2002.03408**.

[103] Supriya Pan, Weiqiang Yang, Chiranjeeb Singha, and Emmanuel N. Saridakis. Observational constraints on sign-changeable interaction models and alleviation of the H_0 tension. *Phys. Rev. D*, 100(8):083539, 2019. **arxiv:1903.10969**.

[104] Kanhaiya L. Pandey, Tanvi Karwal, and Subinoy Das. Alleviating the H_0 and σ_8 anomalies with a decaying dark matter model. *JCAP*, 07:026, 2020. **arxiv:1902.10636**.

[105] Shivam Pandey, Marco Raveri, and Bhuvnesh Jain. Model independent comparison of supernova and strong lensing cosmography: Implications for the Hubble constant tension. *Phys. Rev. D*, 102(2):023505, 2020. **arxiv:1912.04325**.

[106] D.W. Pesce et al. The Megamaser Cosmology Project. XIII. Combined Hubble constant constraints. *Astrophys. J.*, 891(1):L1, 2020. **arxiv:2001.09213**.

[107] Patrick Peter and Jean-Philippe Uzan. *Primordial Cosmology*. Oxford University Press, 2009.

[108] Oliver H. E. Philcox, Mikhail M. Ivanov, Marko Simonović, and Matias Zaldarriaga. Combining Full-Shape and BAO Analyses of Galaxy Power Spectra: A 1.6% CMB-independent constraint on H_0. *JCAP*, 05:032, 2020. **arxiv:2002.04035**.

[109] Oliver F. Piattella. *Lecture Notes in Cosmology*. UNITEXT for Physics. Springer, Cham, 2018. **arxiv:1803.00070**.

[110] Vivian Poulin, Tristan L. Smith, Daniel Grin, Tanvi Karwal, and Marc Kamionkowski. Cosmological implications of ultralight axionlike fields. *Phys. Rev. D*, 98(8):083525, 2018. **arxiv:1806.10608**.

[111] Vivian Poulin, Tristan L. Smith, Tanvi Karwal, and Marc Kamionkowski. Early Dark Energy Can Resolve The Hubble Tension. *Phys. Rev. Lett.*, 122(22):221301, 2019. **arxiv:1811.04083**.

[112] Mohamed Rameez and Subir Sarkar. Is there really a Hubble tension? *Class. Quant. Grav.*, 38(15):154005, 2021. **arxiv:1911.06456**.

[113] S. Refsdal. On the possibility of determining Hubble's parameter and the masses of galaxies from the gravitational lens effect. *Monthly Notices of the RAS*, 128:307, 1964.

[114] Adam G. Riess. The Expansion of the Universe is Faster than Expected. *Nature Rev. Phys.*, 2(1):10–12, 2019. **arxiv:2001.03624**.

[115] Adam G. Riess, Stefano Casertano, Wenlong Yuan, J. Bradley Bowers, Lucas Macri, Joel C. Zinn, and Dan Scolnic. Cosmic Distances Calibrated to 1% Precision with Gaia EDR3 Parallaxes and Hubble Space Telescope Photometry of 75 Milky Way Cepheids Confirm Tension with ΛCDM. *Astrophys. J. Lett.*, 908(1):L6, 2021. **arxiv:2012.08534**.

[116] Adam G. Riess, Stefano Casertano, Wenlong Yuan, Lucas M. Macri, and Dan Scolnic. Large Magellanic Cloud Cepheid Standards Provide a 1% Foundation for the Determination of the Hubble Constant and Stronger Evidence for Physics beyond ΛCDM. *Astrophys. J.*, 876(1):85, 2019. **arxiv:1903.07603**.

[117] Adam G. Riess et al. A 2.4% Determination of the Local Value of the Hubble Constant. *Astrophys. J.*, 826(1):56, 2016. **arxiv:1604.01424**.

[118] Adam G. Riess et al. New Parallaxes of Galactic Cepheids from Spatially Scanning the Hubble Space Telescope: Implications for the Hubble Constant. *Astrophys. J.*, 855(2):136, 2018. **arxiv:1801.01120**.

[119] Adam G. Riess, Lucas Macri, Stefano Casertano, Hubert Lampeitl, Henry C. Ferguson, Alexei V. Filippenko, Saurabh W. Jha, Weidong Li, and Ryan Chornock. A 3% solution: Determination of the hubble constant with the hubble space telescope and wide field camera 3. *The Astrophysical Journal*, 730(2):119, 2011. **arxiv:1103.29766**.

[120] M. Rigault et al. Strong Dependence of Type Ia Supernova Standardization on the Local Specific Star Formation Rate. *Astron. Astrophys.*, 644:A176, 2020. **arxiv:1806.03849**.

[121] Cristian E. Rusu et al. H0LiCOW XII. Lens mass model of WFI2033 − 4723 and blind measurement of its time-delay distance and H0. *Mon. Not. Roy. Astron. Soc.*, 498(1):1440–1468, 2020. **arxiv:1905.09338**.

[122] Jeremy Sakstein and Mark Trodden. Early dark energy from massive neutrinos – a natural resolution of the Hubble tension. *Phys. Rev. Lett.*, 124:161301, 2020. **arxiv:1911.11760**.

[123] Allan Sandage. Current Problems in the Extragalactic Distance Scale. *Astrophysical Journal*, 127:513, 1958.

[124] James Schombert, Stacy McGaugh, and Federico Lelli. Using the Baryonic Tully–Fisher Relation to Measure H_0. *Astron. J.*, 160(2):71, 2020. **arxiv:2006.08615**.

[125] Nils Schöneberg, Guillermo Franco Abellán, Andrea Pérez Sánchez, Samuel J. Witte, Vivian Poulin, and Julien Lesgourgues. The H_0 Olympics: A fair ranking of proposed models. *arXiv e-prints*, 2021. **arxiv:2107.10291**.

[126] Bernard F. Schutz. Determining the Hubble Constant from Gravitational Wave Observations. *Nature*, 323:310–311, 1986.

[127] Bernard F. Schutz. Hubble's constant from gravitational wave observations. In *Gravitational collapse and relativity: proceedings of Yamada Conference XIV, Kyoto International Conference Hall, Japan, 7-11 April 1986*, pages 350–368, 1986.

[128] Bernard F. Schutz. *A First Course in General Relativity*. Cambridge University Press, 2nd edition, 2009.

[129] A. J. Shajib et al. STRIDES: a 3.9 per cent measurement of the Hubble constant from the strong lens system DES J0408−5354. *Mon. Not. Roy. Astron. Soc.*, 494(4):6072–6102, 2020. **arxiv:1910.06306**.

[130] V. M. Slipher. Nebulae. *Proceedings of the American Philosophical Society*, 56:403–409, 1917.

[131] Tristan L. Smith, Vivian Poulin, and Mustafa A. Amin. Oscillating scalar fields and the Hubble tension: a resolution with novel signatures. *Phys. Rev. D*, 101(6):063523, 2020. **arxiv:1908.06995**.

[132] Tristan L. Smith, Vivian Poulin, José Luis Bernal, Kimberly K. Boddy, Marc Kamionkowski, and Riccardo Murgia. Early dark energy is not excluded by current large-scale structure data. *Phys. Rev. D*, 103(12):123542, 2021. **arxiv:2009.10740**.

[133] M. Soares-Santos et al. First Measurement of the Hubble Constant from a Dark Standard Siren using the Dark Energy Survey Galaxies and the LIGO/Virgo Binary–Black-hole Merger GW170814. *Astrophys. J.*, 876(1):L7, 2019. **arxiv:1901.01540**.

[134] D. N. Spergel, L. Verde, H. V. Peiris, E. Komatsu, M. R. Nolta, C. L. Bennett, M. Halpern, G. Hinshaw, N. Jarosik, A. Kogut, M. Limon, S. S. Meyer, L. Page, G. S. Tucker, J. L. Weiland, E. Wollack, and E. L. Wright. First-Year Wilkinson Microwave Anisotropy Probe (WMAP) Observations: Determination of Cosmological Parameters. *The Astrophysical Journal Supplement Series*, 148(1):175–194, 2003. **doi:10.1086/377226**.

[135] S. Taubenberger, S. H. Suyu, E. Komatsu, I. Jee, S. Birrer, V. Bonvin, F. Courbin, C. E. Rusu, A. J. Shajib, and K. C. Wong. The Hubble Constant determined through an inverse distance ladder including quasar time delays and Type Ia supernovae. *Astron. Astrophys.*, 628:L7, 2019. **arxiv:1905.12496**.

[136] Michael S. Turner. Coherent scalar-field oscillations in an expanding universe. *Phys. Rev. D*, 28:1243–1247, 1983. **doi:10.1103/PhysRevD.28.1243**.

[137] Carsten Van De Bruck and Jurgen Mifsud. Searching for dark matter - dark energy interactions: going beyond the conformal case. *Phys. Rev. D*, 97(2):023506, 2018. **arxiv:1709.04882**.

[138] Kyriakos Vattis, Savvas M. Koushiappas, and Abraham Loeb. Dark matter decaying in the late Universe can relieve the H0 tension. *Phys. Rev.*, D99(12):121302, 2019. **arxiv:1903.06220**.

[139] L. Verde, T. Treu, and A. G. Riess. Tensions between the Early and the Late Universe. *Nat Astron*, 3(10):891–895, 2019. **arxiv:1907.10625**.

[140] Deng Wang and Xin-He Meng. Finslerian Universe May Reconcile Tensions between High and Low Redshift Probes. *arXiv e-prints*, 2017. **arxiv:1709.04141**.

[141] Kenneth C. Wong et al. H0LiCOW – XIII. A 2.4 per cent measurement of H0 from lensed quasars: 5.3σ tension between early- and late-Universe probes. *Mon. Not. Roy. Astron. Soc.*, 498(1):1420–1439, 2020. **arxiv:1907.04869**.

[142] Hao-Yi Wu and Dragan Huterer. Sample variance in the local measurements of the Hubble constant. *Mon. Not. Roy. Astron. Soc.*, 471(4):4946–4955, 2017. **arxiv:1706.09723**.

[143] Mark Wyman, Douglas H. Rudd, R.Ali Vanderveld, and Wayne Hu. Neutrinos Help Reconcile Planck Measurements with the Local Universe. *Phys. Rev. Lett.*, 112(5):051302, 2014. **arxiv:1307.7715**.

[144] Weiqiang Yang, Eleonora Di Valentino, Olga Mena, and Supriya Pan. Dynamical Dark sectors and Neutrino masses and abundances. *Phys. Rev. D*, 102(2):023535, 2020. **arxiv:2003.12552**.

[145] Wenlong Yuan, Adam G. Riess, Lucas M. Macri, Stefano Casertano, and Dan Scolnic. Consistent Calibration of the Tip of the Red Giant Branch in the Large Magellanic Cloud on the Hubble Space Telescope Photometric System and a Re-determination of the Hubble Constant. *Astrophys. J.*, 886:61, 2019. **arxiv:1908.00993**.